UNIVERSITY OF HAWAIʻI AT MĀNOA

Flexible Graphene Transistor Architecture for Optical Sensor Technology

A DISSERTATION TO THE GRADUATE DIVISION OF THE UNIVERSITY OF HAWAI'I IN PARTIAL FULLFILLMENT OF THE REQUIREMENTS FOR THE DEGREE OF

DOCTOR OF PHILOSOPHY

IN

ELECTRICAL ENGINEERING

May 2017

By

Richard Christopher Ordonez

Dissertation Committee

David Garmire (chair)

Olga Boric-Lubecke

Victor Lubecke

Narayana Prasad Santhanam

Anupam Misra (University Representative)

ABSTRACT OF THE DISSERTATION

A Flexible Graphene Transistor Architecture for Optical Sensor Technology

By

Richard Christopher Ordonez

Doctor of Philosophy in Electrical Engineering

University of Hawai′i at Mānoa, 2016

Research conducted under the Supervision of Dr. David Garmire

The unique electrical and optoelectronic properties of graphene allow tunable conductivity and broadband electromagnetic absorption that spans the ultraviolet and infrared regimes. However, in the current state-of-art graphene sensor architectures, junction resistance and doping concentration are predominant factors that affect signal strength and sensitivity. Unfortunately, graphene produces high contact resistances with standard electrode materials (~few kilo-ohms), therefore, signal is weak and large carrier concentrations are required to probe sensitivity. Moreover, the atomic thickness of graphene enables the potential for flexible electronics, but there has not been a successful graphene sensor architecture that demonstrates stable operation on flexible substrates and with minimal fabrication cost.

In this study, the author explores a novel 3-terminal transistor architecture that integrates two-dimensional graphene, liquid metal, and electrolytic gate dielectrics (*LM-GFETs: Liquid Metal and Graphene Field-Effect Transistors*). The goal is to deliver a sensitive, flexible, and lightweight transistor architecture that will improve sensor technology and maneuverability. The reported high

thermal conductivity of graphene provides potential for room-temperature thermal management without the need of thermal-electric and gas cooling systems that are standard in sensor platforms. Liquid metals provide a unique opportunity for conformal electrodes that maximize surface area contact, therefore, enable flexibility, lower contact resistance, and reduce damage to the graphene materials involved. Lastly, electrolytic gate dielectrics provide conformability and high capacitances needed for high on/off rations and electrostatic gating.

Results demonstrated that with minimal fabrication steps the proposed flexible graphene transistor architecture demonstrated ambipolar current-voltage transfer characteristics that are comparable to the current state-of-the-art. An additional investigation demonstrated PN junction operation and the successful integration of the proposed architecture into an optoelectronic application with the use of semiconductor quantum dots in contact with the graphene material that acted as optical absorbers to increase detector gain. Applications that can benefit from such technology advancement include Nano-satellites (Nanosat), Underwater autonomous vehicles (UAV), and airborne platforms in which flexibility and sensitivity are critical parameters that must be optimized to increase mission duration and range.

Dedicated to

my loving wife Sola Ordonez

and family

VITA

Education

2010 – Present	PhD. Candidate, Electrical Engineering University of Hawai'i at Manoa, Honolulu, HI, USA
2004 – 2010	Bachelors of Science, Electrical Engineering University of Hawaii at Manoa, Honolulu, HI, USA

Honors, Awards

University of Hawaii Office of Graduate Education Dean's Achievement Award (Spring 2017)

Excellence in Technology Transfer Far West Federal Laboratory Consortium Award (Fall 2016)

Naval Innovative Science and Engineering (NISE) Award to provide advanced research capabilities to the Navy (Fall 2015 - Present)

Department of Navy (DON) Pathways Internship Program (Fall 2014 – Present)

Distinguished Member, National Academy of Inventors Award, University of Hawaii Chapter (Fall 2015)

Advanced Research for College Students (ARCS) Foundation, Brettzlaff Scholar Award (April 2014)

Pacific Asian Center for Entreprnuership (PACE) Breakthrough Innovation Challenge 1st Place Winner (Fall 2012)

IEEE Micromouse Regional Competition 5th Place Winner (Spring 2009)

NASA Hawaii Space Research Grant (Spring 2006)

Research Experience

Graphene Microfluidics Laboratory, Space and Naval Warfare Systems Center Pacific (SSC PAC), Summer 2014 – Present.

Ultra-Low Power Integrated Circuit Design Group, Space and Naval Warfare Systems Center Pacific (SSC PAC), Summer 2014 – Fall 2014.

College of Tropical Agriculture and Human Resources (CTAHR), University of Hawaii at Manoa, Fall 2014.

Center for Adaptive Optics, University of Southern California, Santa Cruz, Summer 2012

Institute for Astronomy, Curvature Adaptive Optics Group, University of Hawaii at Manoa.
Fall 2010 – 2012.

Institute for Astronomy, University of Hawaii at Hilo UH-88 inch Telescope Group, Summer 2009.

Journal Publications

R.C. Ordonez, C. Hayashi, C.M. Torres, J. Melcher, N. Kamin, G. Severa, D. Garmire. "Rapid Fabrication of Graphene Field-Effect Transistors with Liquid-Metal Interconnects and Electrolytic Gate Dielectrics Made of Honey," Submitted to Nature: Scientific Reports (2017), Under Review.

R.C. Ordonez, C. Hayashi, C.M. Torres, N. Hafner, J. R. Adleman, N. Acosta, J. Melcher, N. Kamin, D. Garmire. "Conformal liquid metal electrodes for flexible graphene device interconnects." *IEEE Transactions on Electron Devices*, 63.10 (2016): 4018-4023.

R.C. Ordonez, C. Hayashi, N. Kamin, M.C. de Andrade, D.Garmire, "Radio Frequency Detection with On-chip Graphene." *Naval Engineers Journal,* 126.4 (2014): 155-158.

Conference Publications

R.C. Gough, **R.C. Ordonez**, M.R. Moorefield, K.J. Cho, W.A. Shiroma, A.T. Ohta, "Reconfigurable liquid-metal antenna with integrated surface-tension actuation." presented at *IEEE-NEMS 2016*, Sendai, Japan, 17 Apr. 2016. Conference Proceedings.

R.C. Ordonez, C. Hayashi, C.M. Torres, N. Hafner, J. R. Adleman, N. Acosta, J. Melcher, N. Kamin, D. Garmire. "Flexible graphene liquid metal devices." *Department for Defense Nanotechnology for Defense Conference*, City of Industry, CA, 16 Nov. 2015. Poster Publication.

R.C. Ordonez, N. Acosta, J. Melcher, N. Kamin, D. Garmire.. "Investigation of Liquid Metal Ohmic Contacts for Graphene Photonic Devices." *ASME 2015 International Technical Conference and Exhibition on Packaging and Integration of Electronic and Photonic Microsystems collocated with the ASME 2015 13th International Conference on Nanochannels, Microchannels, and Minichannels*. American Society of Mechanical Engineers, 2015. Conference Proceedings.

R. C. Ordonez, K. Norman, K Uchida, D. Jenkins, D. Garmire , "Investigation of Graphene-Based Coatings for Electroflotation Devices," *Asia Pacific Resilience Innovation Summit & Expo*., Honolulu, HI, 15 Sep. 2014. Poster Publication.

R.C.Ordonez, C. Hayashi, N. Kamin, M.C. de Andrade, D.Garmire, "Charge Amplification of a Graphene integrated-CMOS (GIC) RF Detector," presented at *TechConnect World 2014-Nanotech.*,Washington D.C., USA, 14 Jun. 2014 2. Conference Proceedings.

R. Ordonez, J. Hirano, C. Hayashi, T. Robertson, D. Garmire, "Reflectivity Modulation with Pentahedral Grids for Low-cost Thermal Management of Buildings," presented *at Energy Forum for Advanced Building Skins*., Bressanone, Italy, 5 Nov. 2013. Conference Proceedings.

ACKNOWLEDGEMENTS

I have been very fortunate to work with my friends and colleagues at the University of Hawai′i at Mānoa, Department of Electrical Engineering. I would first like to express my sincere gratitude to Dr. David Garmire, for his continual guidance and support throughout my academic journey. He is an inspirational figure and his continuous mentorship has led to my many successes in both academia and industry. His variety of research efforts has enabled me to become a more well-rounded. I deeply appreciate my PhD dissertation committee Dr. Olga Boric-Lubecke, Dr. Victor Lubecke, and Dr. Narayana Prasad Santhanam from the UHM Department of Electrical Engineering. In addition, Dr. Anupam Misra from the Hawai′i Institute for Geophysics and Planetology for use of his department Raman Spectroscopy System. Their insightful, critical comments, and use of their laboratory equipment has greatly improved my work. Furthermore, their professional and academic advice have allowed me to overcome many challenges. I would also like to thank the graduate and undergraduate students who have assisted in my dissertation work. Especially, Jordan Melcher, Noah Acosta, Matthew Cieslak, and Kevin Kam. Their friendship, discussions, and long research hours have made my academic experience enjoyable.

Lastly, I am very grateful to the Space and Naval Warfare Systems Center Pacific mentors and collaborators. Especially, Cody Hayashi, Nackieb Kamin, Neal Miyake, and Alan Umeda. Their persistent interest in my dissertation work has provided me with the necessary motivation and resources via the prestigious Department of Navy (DON) Pathways Internship Award that enabled me to pursue this work. Their patience, mentorship, and support will never be matched by any other organization. I will always cherish the experience.

TABLE OF CONTENTS

1. Introduction

Graphene is best defined as a monolayer of carbon atoms arranged in a honeycomb crystal lattice that exhibits extraordinarily unique optical, electronic, and mechanical properties [1]. With the first isolation of graphene in 2004 by two Nobel laureates, Andre Giem and Kostantin Novolselov with the exploitation of a *"scotch tape method"*, a surge of studies led by the global scientific community has aimed to incorporate graphene into electronic and mechanical devices. The goal has been to overcome the saturation of Moore's law with fast, lightweight, and flexible graphene devices that benefit from the high charge carrier mobility ($u = 5000\ cm^2/V \cdot s$), high thermal conductivity, atomic thickness, and broadband optical absorption of graphene that spans the ultraviolet and infrared wavelengths [1, 2, 3, 4].

Unfortunately, the adoption of graphene into modern electronics has had little success due to the challenges associated with large-scale fabrication and yield of graphene materials. With these issues, the IC industry has avoided mass production of graphene integrated electronics until graphene synthesis techniques are optimized and cost, dominated currently by limited and complex chemical vapor deposition techniques, is reduced to compete with that of the silicon semiconductor industry. For the time being, commercialization strategies for startups address graphene raw material production (graphene films, graphene oxide (GO) flakes, and graphene nanoplatelets (GNPs)) aimed at small laboratories and academia with little to no growth beyond small research ventures [5]. Therefore, progress for graphene integrated electronics have remained at the basic research level and cannot escape the infamous "Valley of Death". The return on investment of these small efforts have been single to few device demonstrations and publications that barely make a dent on the large-scale potential for graphene technologies. In addition, resistance of current incumbent technologies such as indium tin oxide (ITO) in the flexible display and

transparent electrode industry has placed entry barriers for graphene despite the known advantage graphene will bring to such an industry [5]. To envision large scale production of graphene such as in a graphene field-effect transistors (GFET) and optical detectors at a commercial level, innovative fabrication techniques must be explored to reduce cost, exploit the unique capabilities of graphene, and tap into emerging industries that compete with that of incumbent technologies.

1.1. Dissertation Objectives

The aim of this dissertation is to demonstrate a unique and innovative combination of graphene and liquid materials as alternatives to standard electrode and doping materials that will overcome flexibility, weight, and size limitations of existing graphene field-effect transistors (GFETs) and optical detectors. The proposed work investigates the electronic properties of graphene in the presence of liquid-metals and electrolytic gate dielectrics that are combined as conformal materials for a three-terminal field-effect transistor architecture. Embodiments of the said architecture will demonstrate optical sensor technology using semiconductor quantum dots and PN junctions for nanophotonic applications.

The author encourages the reader to adopt the said methods into their own research in hopes that new innovative embodiments of the said methods will advance electronic devices. The high thermal conductivity of graphene provides potential for room-temperature thermal management that may enable broadband electromagnetic detection without the need of thermoelectric and gas cooling systems that are standard in optical platforms. Moreover, liquid-metals provide a unique opportunity for conformal electrodes that maximize surface area contact, therefore, enable flexibility, lower contact resistance, and reduce damage to a graphene materials involved. Applications that can benefit from such technology advancement include Nano-satellites (Nanosat), underwater autonomous vehicles (UAV), and airborne platforms in which weight, size,

and power consumption are critical parameters that must be optimized to increase mission duration and range.

1.2. Dissertation Structure

The structure of this Dissertation is broken up into 6 chapters. The author describes the aim of this work in Chapter 1. In Chapter 2, the author reviews graphene fundamentals, synthesis, and characterization techniques. In Chapter 3, the author provides an overview of liquid-metal fundamentals followed by a demonstration of the conformal properties of liquid-metal electrodes in a simple two-terminal device embodiment via incremental bend experiments and bend cycle experiments. In Chapter 4, the author provides the technical execution of this dissertation. Discussed are results of conformal liquid-metal electrodes and electrolytic gate dielectrics used in a unique graphene transistor architecture that can be adopted by industry rather quickly. Device characteristics are measured with standard semiconductor processes to validate the architecture with the current state-of-the-art and a study is devoted to the equations needed to extract graphene transfer characteristics from measured data. In Chapter 5, the author discusses several graphene phototransistor architectures by exploitation of the optical properties of graphene to fabricate graphene photonic elements that integrate semiconductor quantum dots and PN junctions to boost detector gain. Finally, in Chapter 6, a summary of the research contributions is given for this dissertation.

REFERENCES

[1] A. K. Geim and N. S. Konstantin, "The rise of graphene," *Nature materials*, vol. 6, no. 3, pp. 183-191, 2007.

[2] R. R. Schaller, "Moore's Law: past, present and future," *IEEE Spectrum*, pp. 52-59, 6 4 1997.

[3] S. Ghosh and et al., "Extremely high thermal conductivity of graphene: Prospects for thermal management applications in nanoelectronic circuits," *Applied Physics Letters*, vol. 92, no. 15, p. 151911, 2008.

[4] K. F. Mak and et al., "Measurement of the optical conductivity of graphene," *Physical Review Letters*, vol. 101, no. 19, p. 196405, 2008.

[5] A. Zurutuza and et al., "Challenges and oppurtuinities in graphene commercialization," *Nature nanotechnology*, vol. 9, no. 10, pp. 730-734, 2014.

2. Background

Carbon popularity originates from its willingness to support a wide variety chemical bonds, some of which are vastly important to sustain of life. Carbon is known as the most versatile of elements due the number of different allotropes it can form. Graphene is only a single allotrope of carbon, meaning additional chemical structures exist for carbon with the same physical state but offer competing electrical and mechanical properties. Among the other allotropes of carbon are metastable diamond (carbon tetrahedral lattices), graphite (stacked hexagonal lattices), fullerenes (Buckminsterfullerene), and carbon nanotubes (tube-like rolled carbon sheets).

Early research in carbon electronics focused mainly on electronic devices made with carbon nanotubes with the sole-purpose of electrical and optical phenomena at the nanometer scale. In 2008, a study published in *Nature Nanotechnology* linked carbon nanotubes to look and behave like asbestos fibers. Laboratory experiments with mice exhibited cancer-like characteristics that included inflammation and the formation of lesions called granulomas [1]. The cumulative knowledge of such studies led researchers to diagnose carbon nanotubes as highly dangerous and can destroy the human immune system if exposure exceeded that of 30 to 40+ years [1,2].

The isolation of graphene came with little hesitation as graphene was assumed to be no more dangerous than a standard #2 pencil. Furthermore, graphene exhibited uniquely desirable electrical and mechanical properties that were of benefit to the scientific community and outperformed that of carbon nanotubes. To understand the origin and importance of these properties, we must first focus our attention to the chemical nature of carbon.

2.1. Chemical Structure

Carbon is currently the sixth most abundant element in the universe and ironically has atomic number of six. The electron configuration of the lowest energy state of carbon is 1s2 2s2 2p2 and follows that of the pauli exclusion principle that states no two fermions with the same electronic spin can occupy the same quantum state simultaneously. However, carbon is a little tricky in that the 2s and 2p quantum states share similar energies. Therefore, the four outer electrons of carbon can experience the chemical phenomena known as hybridization.

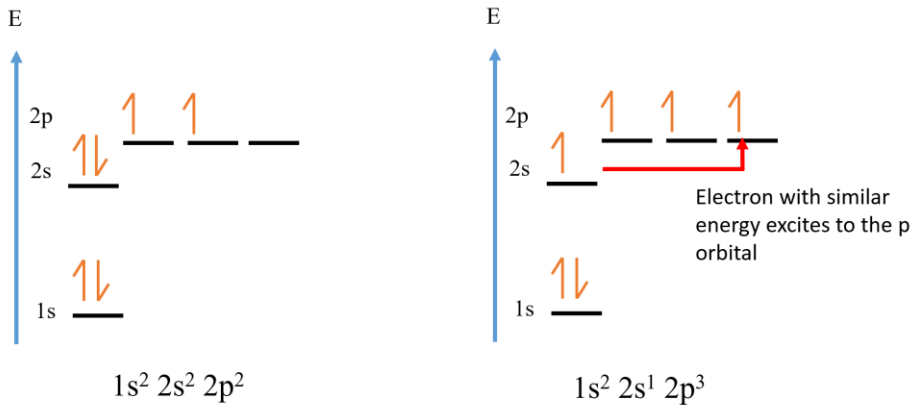

Fig. 2.1. Electron Configuration for carbon before (left) and after (right) hybridization.An electron from the 2s quantum state excites to the 2p quantum state.

Hybridization is defined as the mixing of quantum states (atomic orbitals) into new hybrid quantum states with different energies and shapes, Fig. 2.1. For example, the individual carbon atoms of graphene undergo sp2 hybridization, meaning an electron from a radially symmetric s-orbital mixes with 2 available p-orbitals. The result is a 3 sp2 hybridized orbitals with a single unchanged 2p orbital. In space, the planar atomic orbitals align with 120° separation forming a molecular geometry of a trigonal planar geometry with a single electron occupying each orbital ready for covalent bonding.

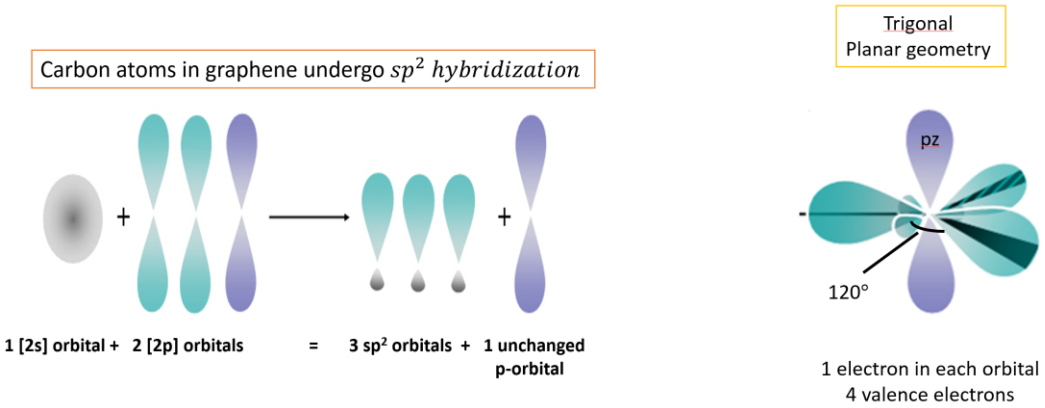

Fig. 2.2. Mixing of graphene orbitals

When a carbon atom comes into proximity with an additional carbon atom, a C-C (carbon-carbon) bond is formed that influences the physical properties of graphene. Fig. 2.3 illustrates the formation of covalent bonds both in the XY plane and Z plane. In the XY plane of reference, a strong σ-bond is formed and corresponds to the mechanical strength of graphene and demonstrates the carbon atoms align to form a planar hexagonal lattice structure. The mechanical properties of graphene will be discussed in a later section. In the Z plane of reference, a π-bond is made and becomes responsible for the desirable electronic properties of graphene. The explanation of the electronic properties of graphene is described in the following sections.

2.2. Electronic Band Structure

As stated in the previous section, the molecular geometry of the carbon atoms in graphene become trigonal planar. Each sp2 hybridized carbon atom will form strong covalent bonds with its nearest neighbor. The result is the famous honeycomb lattice structure.

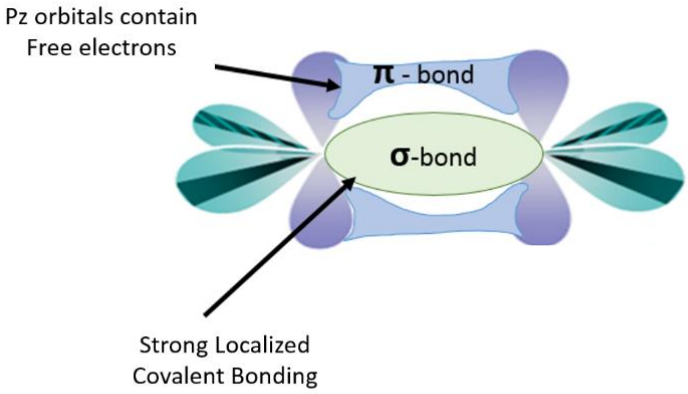

Fig. 2.3. Illustration of C-C bond of graphene. Inset: graphene hexagonal array. Note the σ-bond in the XY plane of reference form a trigonal planar geometry with neighboring carbon atoms and form the mechanical strength of graphene. The π-bonds are responsible for the electronic properties of graphene.

The electronic band structure of graphene can be derived by the segmentation of the honeycomb lattice structure into adjacent sub lattices of two atoms per unit cell. The application of a tight-binding approach within each unit cell along with the realization that the free electron of each carbon atom can hop between π orbitals of the nearest-neighbor (t = 2.7 eV) and the next-nearest neighbor (t' = 0.2t) with different energy derives the complex Hamiltonian for electrons in graphene and as described in [1]. The resultant energy dispersion relationship derived from the Hamiltonian in [1] is shown in Fig. 2.4.

Referring to the energy band dispersion of Fig. 2.4, the conduction band (top) and valence bands (bottom) meet at the six corners (dirac points) of the brillouin zone. If the energy dispersion is expanded close to these dirac points (K, K') and electron hopping is ignored between the next-nearest neighbor carbon atom (t' = 0), the band energy can be approximated as:

$$E^{\pm}(k) = \hbar v_F \boldsymbol{k}$$

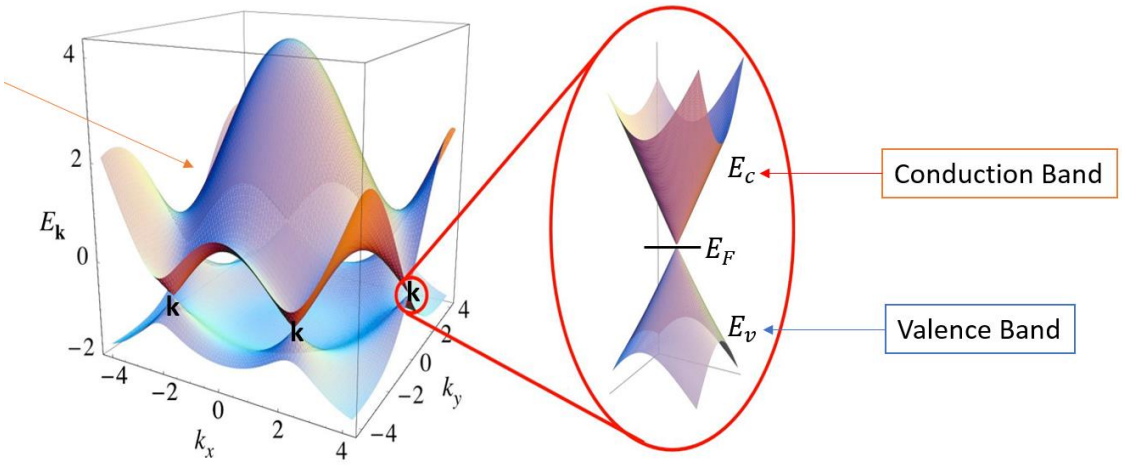

Fig. 2.4. Energy dispersion relation of monolayer graphene. Note the valence band and conduction band meet a (K , K') points within the Brillouin zone [1] and the orbitals form a conical shape.

where ħ is the reduced plancks constant, v_F is the fermi velocity ($\sim 10^6 \frac{m}{s}$ or $\frac{c}{300}$), and wave vector $\boldsymbol{k} = (k_x, k_y)$ which is measured from the dirac points where there is zero density of states with no band gap. Graphene is than best described as a semi-metal or zero band gap semiconductor. A unique feature of the electronic band structure of graphene is its linear dispersion relationship $E = \hbar v_F k$ that is vastly unlike that of conventional semiconductors energy dispersion relationship $E = \frac{\hbar^2 k^2}{2m^*}$ which is parabolic. This is mostly due in part to the quasi particles in graphene sustaining a zero-effective mass in the vicinity of its dirac points. Graphene is an exception in that its charge carriers mimic relativistic particles and are easier to describe with the dirac equation rather than the Schrodinger equation [2]. It is important to note that in unbiased graphene, the fermi velocity reduces to the dirac points of the brillouin zone. Hence, the valence band is completely occupied by electrons and the conduction band is completely empty above the dirac point. In the next section, we discuss the importance of altering the fermi energy.

2.3. Electrical Properties

As mentioned in the previous section the fermi level for unbiased graphene is situated at the six dirac points which are located at every corner of the hexagonal structure. Near the dirac points, the density of states becomes zero, therefore, the electrical conductivity of graphene fermions remains low and is on the order of the conductance quantum $\sigma = e^2/h$, where e is the elemental charge and h is planks constant [2].

However, the energy dispersion, $E^{\pm}(k) = \hbar v_F \boldsymbol{k}$, of graphene is unique in that graphene particles behave like massless dirac fermions. A consequence of this massless dirac-like behavior is the cyclotron mass depends on the electronic density as its square root [1]. In this condition, the fermi energy can be approximated as:

$$E_F = \hbar v_F \sqrt{\pi n}$$

where the electronic density n is related to the fermi momentum k_F, is ${k_F}^2/\pi = n$. An application of this idea is implemented in a graphene field-effect transistor (GFET). Variable field-effects in a GFET device are achieved by a variable DC gate-bias across the gate electrode and bulk substrate. The density of carriers in the graphene channel n can be estimated from the surface charge density induced by the applied DC gate-bias V_{gs} in that:

$$n = \frac{\varepsilon_0 \varepsilon_r V_{gs}}{te}$$

Therefore, the fermi energy of the graphene material under an applied gate-bias becomes:

$$E_F = \hbar v_F \sqrt{\pi \frac{\varepsilon_0 \varepsilon_r V_{gs}}{te}}$$

Under this condition, the fermi energy can be shifted to any desirable level and can be used to vary carrier density in that the graphene channel will conduct n-type (electron) carriers or p-type (hole) carriers. This effect determines the ambipolar characteristics of graphene and allows one to design

a device that has both n-type and p-type characteristics. An illustration of the ambipolar resistivity characteristics is shown in Fig. 2.5(c). It is important to note as the gate-voltage exceeds (V_{gs} = 0), the resitivity changes drastically for small values of V_{gs}.

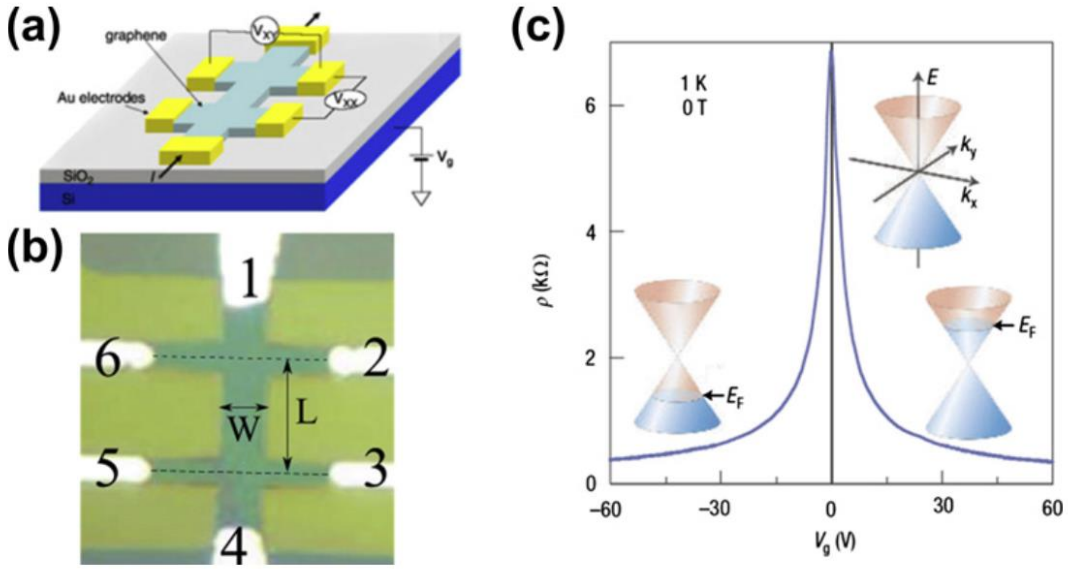

Fig. 2.5. Ambipolar electric field-effect in monolayer graphene. (a) and (b) schematic and image of typical three-terminal device (hall bar configuration) used to modulate graphene channel resistivity [3]. (c) Alteration of graphene channel resistivity by an applied gate voltage [2]. Note changes in the position of the fermi energy EF with respect to a change in voltage determine carrier density and carrier type.

Modulation of the carrier density away from the dirac points allowed carrier motilities to be measured in excess of 100,000 $cm^2V^{-1}s^{-1}$ and utilization of the hall bar configuration in Fig. 5 has led researchers to exhibit hall mobilities near 200,000 $cm^2V^{-1}s^{-1}$with carrier concentration as low as $5\times10^9cm^{-2}$ [4, 5].

Graphene exhibits a very large thermal conductivity $\sim3080-5150\ W/m\cdot k$ [6]. An important implication of high thermal conductivity is that graphene can be used in application where thermal management is critical. Graphene can naturally be made into heat sinks and can be applied into

infrared detectors as response time is directly related to the amount of time it takes to remove heat from a photoconductive surface.

2.4. Mechanical Properties

Graphene was awarded the title as the strongest material with respect to its atomic thickness. A fracture test demonstrated the mechanical strength of graphene with the use of an atomic force microscope probe [3]. In that test, pressure was carefully provided by an atomic force microscope probe tip on the graphene surface and strain measurements were taken before the material buckled under stress. The result was an elastic stiffness of 340 N/m (newton per meter) for a monolayer graphene material, therefore, made graphene the strongest material ever measured using this method and was determined to be stronger than steel.

2.5. Optical Properties

Graphene is virtually transparent and is not easily detectable with the naked eye. Therefore, graphene quality is typically characterized with sophisticated optical characterization techniques such as Raman Spectroscopy and Optical Characterization Methods (Section 2.6). Despite its opacity, graphene has an optical absorption of about 2.3% and was experimentally deemed constant over the ultraviolet to infrared spectrum [7].

In current optical sensors, high quantum efficiency is achieved by managing bandgap energies of semiconductor alloys. Fabrication of these alloys can become costly and demand rigorous processing. The spectral response is than limited to a few investigations as spectral absorption is dependent on the bandgap energy. Such materials also have low thermal conductivity;

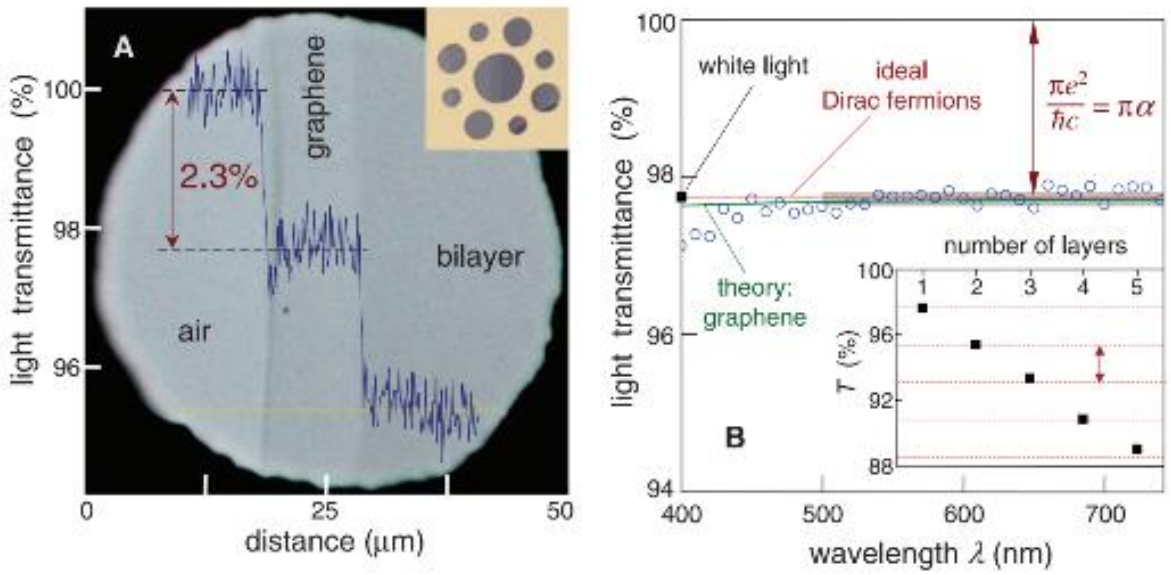

Fig. 2.6. (left) 50-micron aperture covered with graphene and bilayer graphene. (right) transmission spectrum of graphene that span ultraviolet and near-infrared spectrum. Fine structure constant of absorption ($\pi\alpha = 2.3\%$) [7].

therefore, require researchers to maintain complex cooling systems to increase SNR. To achieve broadband operation, additional sensors are required and modified with filters or gratings. As a payload, these modifications may increase complexity, weight, and overhead.

As discussed in Section 2.3, The linear dispersion of graphene allows the fermi energy in graphene to be shifted by hundreds of millivolts through electrostatic gating. Electrostatic doping leads to a screening of interband transitions with an energy less than twice the fermi energy due to Pauli blocking, Fig 2.7. The optical response of graphene becomes controllable with the electric field-effect and can be implemented with a graphene field-effect transistor architecture. Such a benefit can be applied to an optical sensor technology in the form of a wide-band tunable spectral response that can be achieved at the transistor level. In addition, the high carrier mobility and low thermal conductivity of graphene can increase response time

and reduce the need for complex cooling systems that are required by broadband imagers such as hyperspectral imagers.

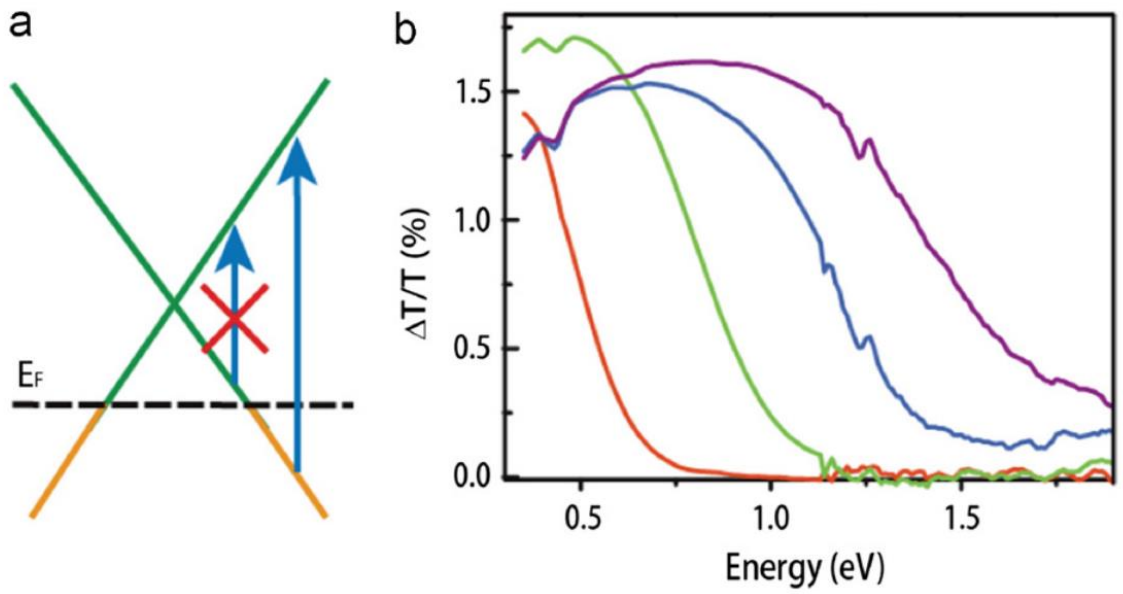

Fig. 2.7. Gate-tunable interband transitions in graphene: (a) Optical absorption governed by interband transitions. Optical transitions at photon energies $> 2E_F$ are allowed, energies $< 2E_F$ are blocked, (b) the gate-induced change of transmission in hole-doped graphene as a function of gate voltage (from left to right): 0.75, 1.75, 2.75 and 3.5 V [8].

2.6. Graphene Characterization via Optical Characterization techniques

2.6.1. Raman Spectroscopy

Due to the atomic thickness of graphene, it is rather difficult to measure the quality of a graphene with traditional methods and without damage. However, in graphene the Stokes phonon energy shift caused by laser excitation is resonant. Therefore, implementation of Raman Spectroscopy is allowed and enables researchers to characterize the number of graphene layers optically and non-destructively.

Raman Spectroscopy is defined as an optical characterization technique in which the inelastic scattering of monochromatic light interacts with a sample [9] and provides a unique spectral profile

of the scattering events within the sample. A Raman spectroscopy measurement typically consists of illuminating a sample with either UV, visible, or infrared light followed by a measurement of the re-emited light with a spectrometer. The relationship with respect to the laser source is called a Raman shift Δw and is given by the following:

$$\Delta w(cm^{-1}) = \left(\frac{1}{\lambda_0(nm)} - \frac{1}{\lambda_1(nm)}\right) \times \frac{(10^7)}{(cm)}$$

where λ_0 is the frequency of the laser source and $\lambda_1$is the frequency of the re-emitted light. Most of the light re-emitted is of the same frequency as the laser source and is called Raleigh Scattering and is typically removed via an optical notch filter before entering the spectrometer. However, some of the re-emitted light is shifted from the laser source and is due to the inelastic scattering. There are two types of Raman scattering effects known as Stokes and Anti-Stokes scattering. In Stokes scattering, the energy of the light re-emitted is at a lower energy then the laser source. However, in Anti-stokes scattering the energy of the light re-emitted is of a higher energy. The corresponding Raman shifts provide valuable information on the vibrational and rotational modes of the sample under test. Information can be extracted from the Raman data such as quality, number of layer, mechanical strength, and electrical properties of the sample.

Utilization of Raman spectroscopy can be exploited to measure the electrical and mechanical properties of graphene. For simplicity, this discussion will only focus on the determination of the number of layers of graphene. The most prominent Raman features of graphene are the G-peak, D-peak, and 2D-peak. A careful analysis of the amplitude of each of the Raman peaks can aid in the determination of the number of graphene layers. The G-Peak occurs at a Raman shift value of $\sim 1580\ cm^{-1}$and corresponds to bond stretching of all pairs of sp^2 atoms in both rings and chains [9]. The G-peak can also be described as the first-order Raman scattering process linked to a doubly degenerate in-plane phonon modes (TO transverse optical and LO longitudinal optical).

The 2D peak which is typically the largest peak in the Raman profile of graphene occurs at $\sim 2700\ cm^{-1}$ and is a second-order double resonant process between the dirac points of graphene. The D-peak is special in that it can occur at both the $\sim 1350\ cm^{-1}$ and $\sim 2450\ cm^{-1}$ respectively, and corresponds to breathing modes of sp^2 atoms in rings, also known as overtones. The D-peak is typically a forbidden phonon mode, however, in the presence of defect scattering the symmetry is broken and the transition is allowed.

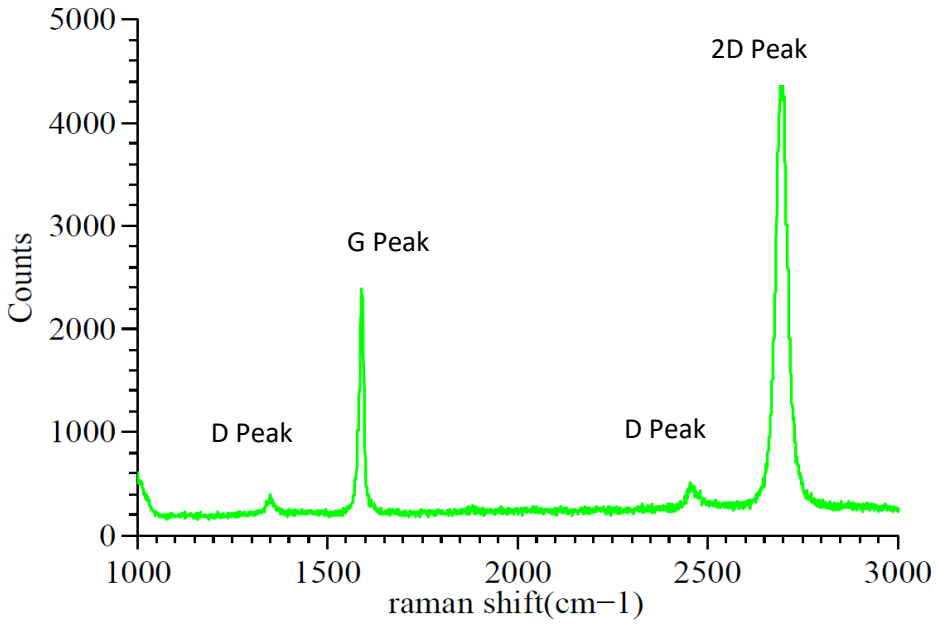

Fig. 2.8. Raman Spectroscopy profile of graphene monolayer on support catalyst using a 514 nm Renishaw Confocal Micro-Raman Spectroscopy System

Fig. 2.8 illustrates a typical Raman profile for a graphene monolayer with locations of the 2D, G, and D-peaks. Analysis of the ratio of I_{2D}/I_G determines the number of graphene layers. A ratio of $I_{2D}/I_G > 2$ corresponds to monolayer graphene. Additionally, the presence of a D-peak corresponds to graphene defects, however, the graphene is still considered useful if the D-peak is much smaller.

2.6.2. Optical Contrast Method

Due to a scalable optical absorption of graphene of 2.3 % per graphene layer, the number of graphene layers can easily be computed with the linear relationship of graphene layer count and image contrast, also known as the *optical contrast method*:

$$C = 0.0778x + 0.005$$

where C is image contrast and x is the graphene layer count [10]. The optical contrast method was implemented with the following methods:

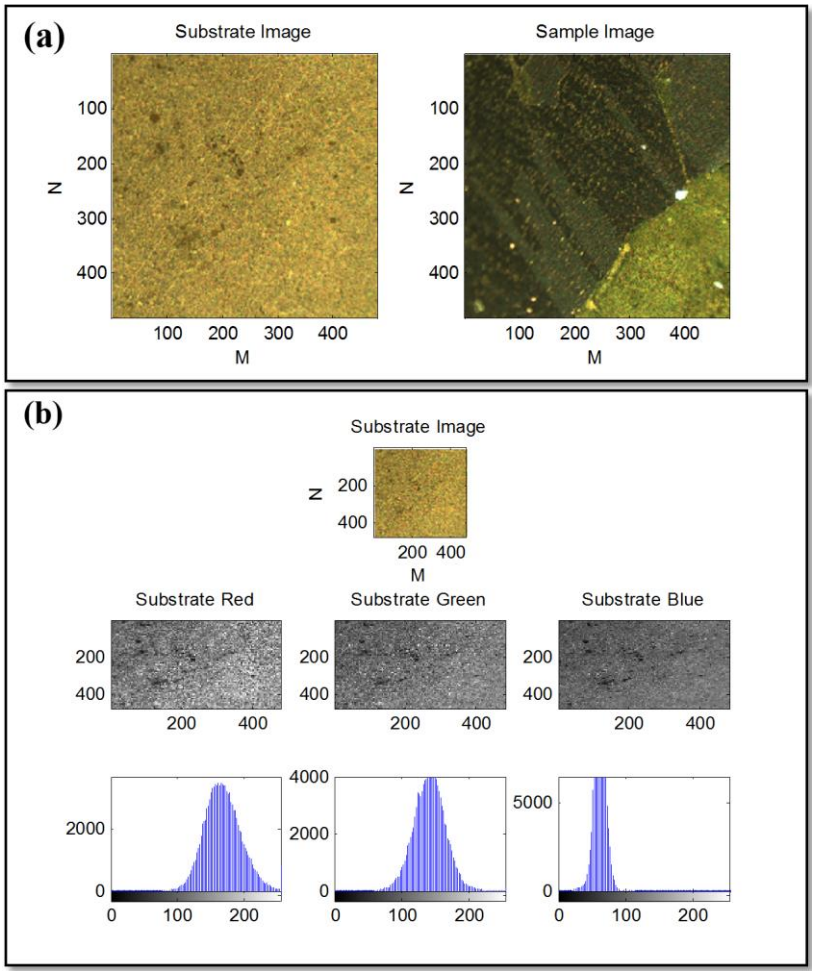

Fig. 2.9. (a) Images of bare copper substrate and (b) boundary of graphene sysnthesized on copper cubstrate via chemical vapor deposition.

a) Individual images of bare copper substrates are taken and compared to graphene synthesized on the copper substrates via chemical vapor deposition (CVD graphene) Fig 2.9(a).

b) The images are separated into corresponding red, green, and blue (RGB) images with the use of MATLAB image processing techniques and the color with best image contrast determined with histograms is further analyzed.

c) A block mesh was then used to divide the image into subsections.

d) In each subsection, the average pixel intensity is computed and used to solve for graphene layer count:

$$C = \frac{G_{sub} - G_{sam}}{G_{sub}}$$

where *C* is the image contrast and G_{sub} is the pixel intensity for the bare substrate and G_{sam} is the pixel intensity for the CVD graphene.

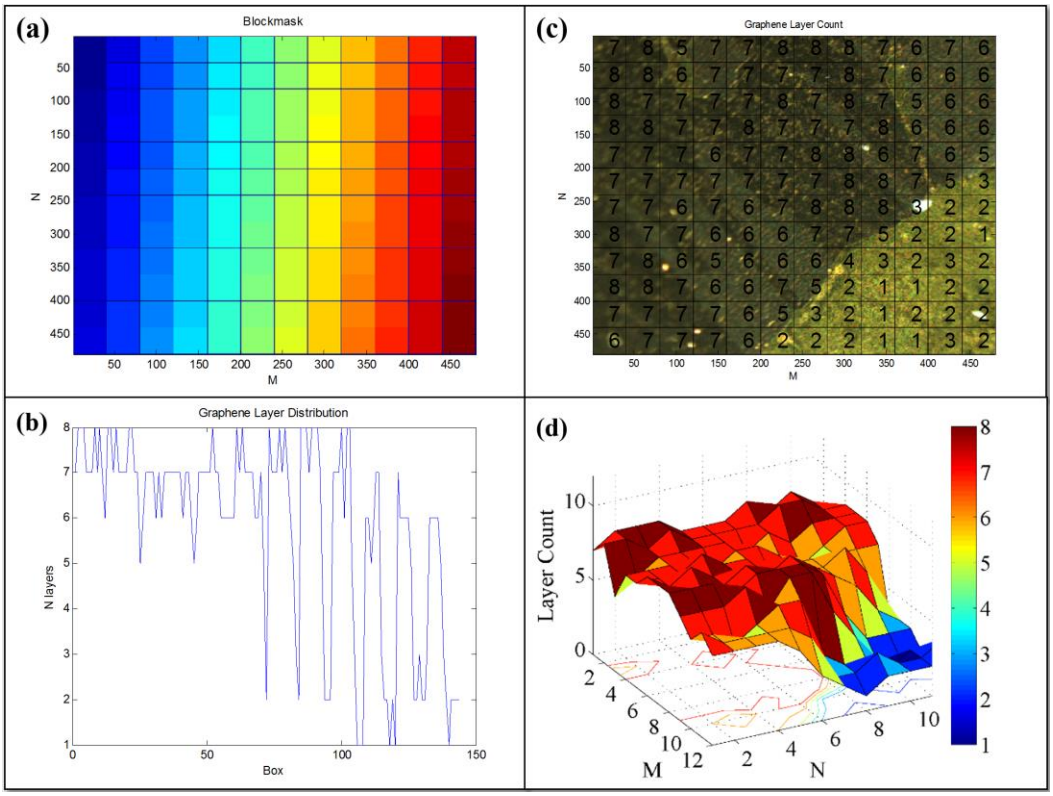

Fig. 2.10. (a) Block mesh used for optical contrast method. (b) Graphene layer count in each block area and (c) graphene layer count overlaid on image of CVD graphene. (D) Surface plot of graphene layer count for CVD graphene boundary. The boundary of the monolayer and multi-layer graphene is determined by the colormap.

REFERENCES

[1] C. Neto and et al. , "The electronic properties of graphene," *Review of modern physics,* vol. 81, no. 1, p. 109, 2009.

[2] A. K. Geim and K. Novoselov, "The rise of graphene," *Nature Nanomaterials,* vol. 6, no. 3, pp. 183-191, 2007.

[3] Z. Jiang and et al., "Quantum Hall effect in graphene," *Solid State Communications,* vol. 143, pp. 14-19, 2007.

[4] C. Dean and et al., "Boron nitride substrates for high quality graphene electronics," *Nature nanotechnology,* vol. 5, no. 10, pp. 722-726, 2010.

[5] K. I. Bolotin and et al., "Ultrahigh electron mobility in suspended graphene," *Solid State Communications,* vol. 146, no. 9, pp. 351-355, 2008.

[6] S. Ghosh and et al., "Extremely high thermal conductivity of graphene: Prospects for thermal management applications in nanoelectronic circuits," *Applied Physics Letters,* vol. 92, no. 15, p. 151911, 2008.

[7] R. Nair, "Fine structure constant defines visual transparency of graphene," *Science,* vol. 320, no. 5881, p. 1308, 2008.

[8] K. F. Mak and et al., "Optical Spectroscopy of graphene: From far infrared to ultraviolet," *Solid State Communications,* vol. 152, pp. 1341-1349, 2012.

[9] J. H. Warner and et al., Graphene: Fundamentals and emergent applications, Newnes, 2012.

[10] Y. Y. Wang, "Thickness identification of two-dimensional materials by optical imaging," *Nanotechnology,* vol. 23, no. 49, p. 495713, 2012.

3. Conformal Liquid Metal Electrodes for Flexible Graphene Devices

As industry miniaturizes flexible circuits into smaller dimensions, thermal management difficulties are exacerbated and additional stress is placed on device interconnects when flexed [1]. There is an immediate need to fabricate more robust device interconnects that can withstand a variety of shapes and contours under flexure. The discovery of graphene leads to endless implementations of atomically thin [2], conductive, transparent, and flexible devices. As carbon materials become more available due to reduction in graphene synthesis cost, the high thermal conductivity and atomic thickness of two-dimensional graphene enables unique opportunities for a variety of applications where size, shape, and conformability to unconventional contours are critical.

Recent attempts to utilize graphene in flexible electronics have led to advances in capacitive multi-touch sensors [3], graphene-based light-emitting devices [4], and nonvolatile memory [5]. The robust high performance of these devices is rarely achieved due to problems associated to interfacial delamination and cracking of traditional device electrodes that are mainly comprised of gold, silver, and their composites [6]. A plausible solution to construct graphene flexible devices is to fabricate source and drain electrodes with titanium and gold that utilize physical vapor deposition (PVD) processes such as plasma-enhanced thermal evaporation and or metal sputtering [7]. However, PVD processes are expensive, tedious, and rely on lithographic techniques that have consistently proven to alter the electronic properties of graphene. For example, the photoresist and deposition gases used in PVD processes lead to unwanted chemical doping and contamination that reduce device yield and alter performance [8]. The result of such processes is irreversible mechanical and electrical degradation of graphene, such as wrinkling, cracking, delamination.

3.1. Liquid Metal Fundamentals

Conductive fluids have been used to make connections in microelectromechanical systems and microfluidics for various applications that include physical and biomedical sensors. In one study, a microfluidic normal force sensor for tactile feedback demonstrated repeatable measurements of static uniaxial loads [9]. In another study, mercury was utilized to fabricate tunable organic transistors that use microfluidic source and drain electrodes that are noninvasive and suitable for fragile organic semiconductors [10]. Unfortunately, the occupational and safety hazards of liquid mercury such as the toxicity and high vapor pressure have slowed large-scale device integration. The *National Council for Occupational Safety and Health* states exposures to large concentrations of mercury vapor lead to severe respiratory damage, headaches, short-term memory loss, weakness, loss of appetite, psychiatric effects, and kidney damage [11].

The discovery of Galinstan, a eutectic gallium alloy comes with much interest, as claims of its non-toxicity and similar liquid properties to mercury make Galinstan highly desirable for a variety of applications where mercury is at a loss. Galinstan is known as a commercially available and easily obtained non-toxic eutectic alloy of 68.5% gallium, 21.5% indium, and 10% tin [12]. Most importantly, Galinstan exhibits a high electrical conductivity ($3.83\ x\ 10^6\ S/m$) [13] (siemens per meter), a desirable thermal conductivity of ($16.5\ W\ m^{-1}K^{-1}$) (watts per meter kelvin)], and can exist in a liquid state across a broad temperature range ($-19℃\ to\ 1300℃$) [13]. A summary of Galinstan properties is illustrated in Table 3.1.

Property	Galinstan	Mercury
Color	Silver	Silver
Melting point	-19℃	-356.62℃
Boiling Point	>1300℃	-38.83℃
Density	6440 $\frac{kg}{m^3}$	13533.6 $\frac{kg}{m^3}$
Solubility	Insoluble	Insoluble
Viscosity	$2.4 \times 10^{-3} Pa\ s$ at 20℃	$1.56 \times 10^{-3} Pa\ s$ at 25℃
Thermal Conductivity	16.5 $W\ m^{-1}K^{-1}$	8.541 $W\ m^{-1}K^{-1}$
Electrical Conductivity	$3.83 \times 10^6\ \frac{S}{m}$	$1.04 \times 10^6\ \frac{S}{m}$

Table 3.1: Summary of electrical properties of Galinstan in comparison to Mercury

It is important to note that Galinstan exhibits a low vapor pressure (<10^{-8} Torr at 500℃) with respect to high vapor pressure of mercury (10^{-3} Torr at 75℃) [14]. A low vapor pressure is desirable in electronic design because particles cannot escape from the substance readily, therefore, the stability of the substance can be predicted in situ. In addition, a substance that exhibits low vapor pressure is non-volatile, therefore, reduces occupational and safety hazards when handling the substance in standard laboratory environments.

3.1.1. Liquid-metal Resistivity

To measure resistivity is to understand how a material handles current. In device fabrication, resistivity is a desirable parameter to characterize before the design process occurs as resistivity determines the ability of a material to pass electrical current. The origin of resistivity is a result of

electron scattering, meaning energy is lost to electron collisions rather than linear movement through the medium. A material with high resistivity typically has low conductivity as energy is lost to heat. For example, as a device material in photodetectors, a highly resistive material results in unexpected thermal excitations that result in unpredictable signal operation. The generated heat can be transferred to surrounding electrical components and may potentially be registered as a detected signal. This can be contributed as dark current in a two-dimensional camera image.

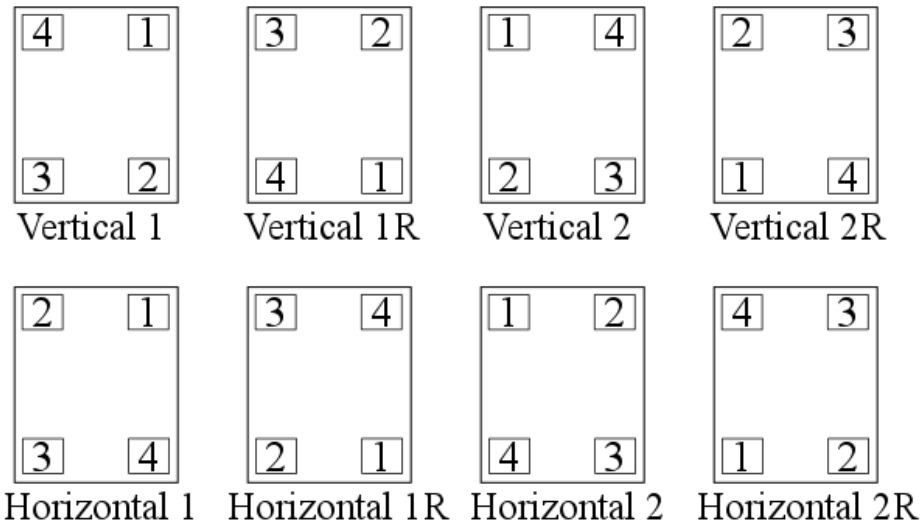

Fig. 3.1. Van der Pauw wiring configurations. The numerical values represent the number of the probe used. For ease of understanding, current was forced between probes 1→2. Voltage was measured between probes 3→4.

Due to the liquid properties of Galinstan, the resistivity of Galinstan can be measured with a modified Van der Pauw method [15]. The Van der Pauw method is a method for quantifying the resistivity and hall coefficient (if magnetic field available) of a sample with arbitrary shape [16]. The technique is typically used in the integrated circuit (IC) technology to measure impurity type

of a silicon wafer being that the commercial vendors sell silicon wafers that are either N-type or P-type.

The Van der Pauw method employs a total of eight measurement configurations in which current is sourced between two contacting probes and voltage is measured between the remaining two probes, Fig. 3.1. The Current-Voltage (I-V) measurements of each configuration are averaged, fitted, and a resistance is computed from the slope of the I-V curves. The resistance is than measured for both the vertical and horizontal configurations,

$$R_v = \frac{R_{1243} + R_{2134} + R_{4312} + R_{3421}}{4}$$

$$R_h = \frac{R_{1423} + R_{4132} + R_{2314} + R_{3241}}{4}$$

where R_v and R_h are the averaged resistances from each configuration in Fig. 3.1. With a Newtow Raphson algorithm written in MATLAB, the sheet resistance R_s is given by,

$$e^{-\pi R_v/R_s} + e^{-\pi R_h/R_s} = 1$$

The numerical result for resistivity is then computed from the simple relationship between sheet resistance and thickness of the sample (if known),

$$\rho = R_s \times t \ (\Omega \cdot \mathrm{m})$$

where ρ is the resistivity, R_s is the sheet resistance, and t is the sample thickness. For this method to be valid the followings conditions must be met: (1) the probes must be on the perimeter of the sample, (2) the probes must be infinitesimally small with respect to the sample, and (3) the probes must be made with the same materials.

Due to the liquid properties of Galinstan, a microfluidic device made of Polydimethylsiloxane (PDMS) was fabricated with soft-lithography to allow Galinstan to hold its own shape during Van der Pauw measurements, Fig. 3.2. First, a channel design was made with a computer-aided design (CAD) software and cut into a double-sided polyimide film (Kapton Double-sided Tape) using a Silhouette electronic cutting tool. The cut shape was removed from the stencil and adhered to the bottom of a container to act as a mold, Fig 3.2(a). A solution of 10:1 silicone elastomer and hardener was poured into the mold a cured in an oven at 60℃ for 45 minutes or until hard to form the elastomer cavity for liquid metal. Holes were then punched in the solidified elastomer to act as injection ports, Fig. 3.2(b), and the elastomer was overlaid on the pre-cut polyimide stencil, Fig 3.2(c). Four tungsten wires were then placed within the microfluidic device to act as Van der Pauw Probes, Fig 3.2(d). In the last step, the liquid metal was introduced into the elastomeric cavity with pressure driven actuation provided by a standard 1 ml blunt cut syringe needle and syringe pump, Fig. 3.2(e). The temperature dependent Galinstan resistivity is illustrated in Fig. 3.3. The result of the Galinstan resistivity test is in good agreement with the inverse in Galinstan conductivity measured in [13]. In addition, it was evident that there was a slight increase in resistivity as the distances between the probes were increase, therefore, mobile charge carriers have a higher probability of colliding with the vibrating atoms. The exchange of energies (electron-phonon interaction) will impede the flow of charge carriers through the material, therefore, the conductivity will drop and the resistivity

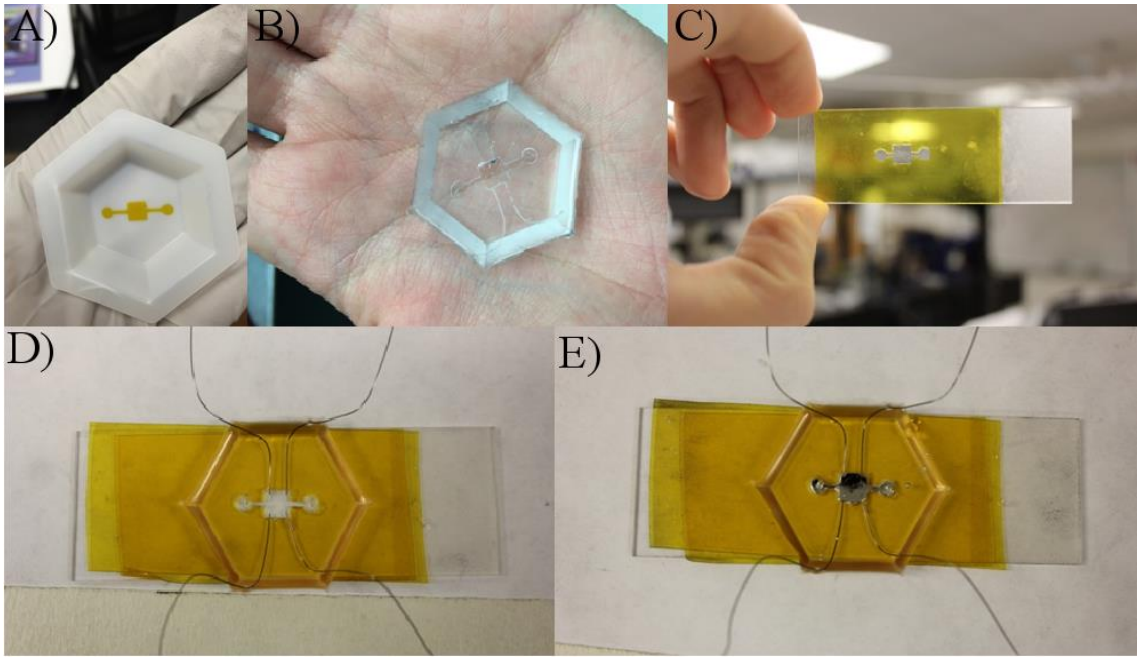

Fig. 3.2. Microfluidic device used for liquid metal four-point probe resistivity measurements: (A) Mold. (B) Solidified PDMS. (C) Bottom of microfluidic which consists of the pre-cut inverse shape of the mold used in (A), adhered to a glass slide. Microfluidic device with four tungsten probes before liquid metal injection (D) and after (E).

will increase as shown in Fig. 3.3. However, liquid metals are known to have a high thermal conductivity which is inversely related to resistivity via Wiedmann-Franz law [17]. With this idea in mind, the resistivity of liquids metals such as Galinstan will gradually increase as the environmental temperature increases and is evident in Fig. 3.3 as an approachable saturation point at elevated temperatures. This may be due to the desirable effects of high thermal conductivity and allows liquid-metals to be more suitable for a variety of devices in which heat effects performance. In a microbolometer it is desirable to measure thermal fluctuations in scene, therefore, the amount of time it will take for the photo resistive element of the microbolometer to detect thermal fluctuations in its enviroment, will ultimately determine the operational speed of the device. Currently, in un-cooled microbolometers, thermal time constants are on the order of milliseconds which is considered very slow.

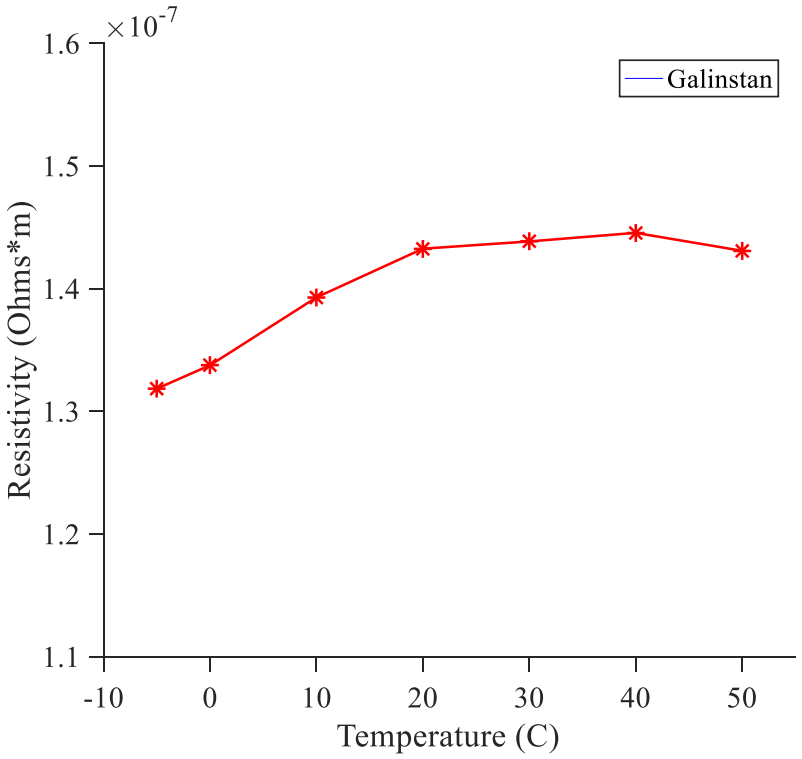

Fig. 3.3. Galinstan resistivity as a function of temperature. The device was cooled with a thermoelectric cooler. The dimensions of the Galinstan area under test are (1cm x 1cm x 300 microns).

3.1.2. Liquid-metal alloying effect

Large-scale device integration of liquid-metals such as Galinstan exhibit an alloying effect in contact with common metals: copper, tin, lead, zinc, gold, silver, and aluminum [18]. Insulating oxide barriers form at the liquid-metal/solid-metal interfaces, which can lead to electronic instability, and ultimately hinder device performance [19]. Carbon-based materials provide a unique solution for liquid-metal integration into device electronics because the inertness of carbon does not allow the formation of surface oxides to occur at the material boundaries. In one study, monolayer graphene acted as a diffusion barrier between Galinstan and aluminum, therefore, reliable electrical contact was achieved without corrosion or degradation to the aluminum material under test [20]. Additionally, the same study determined the chemical inertness of graphene via minimal changes Raman spectroscopy profiles before and after Galinstan exposure [20]. In an

alternative study, the unique catalytic properties of liquid-metals promoted residue-free and defect-free graphene synthesis with large area scalability [21]. Presently, RF applications have already benefited from the use of carbon rods that reduce oxidation and contamination while driving liquid-metal Galinstan slugs. The carbon rods allowed the authors to apply electrical stimulus needed to move liquid-metal Galinstan slugs via cavities filled with salt electrolytes in electrical devices [22].

3.1.3. Oxidation effects of encasing liquid-metals

The rapid surface oxidation of gallium alloys in air introduces challenges in that the formation of surface oxides degrade and overcome surface tension, therefore, enables liquid-metal droplets to actively wet to surrounding surfaces. The result is non-Newtonian fluidic characteristics analogous to paste that cause difficulty when moving liquid-metal structures through microfluidic systems. Multiple techniques are available to prevent the formation of surface oxides, such as strong acid/base immersion, atmospheric controlled environments, or encasement in oxygen impermeable materials [12]. In either approach, proper control over oxide growth will enable liquid-metals to move freely in a liquid state.

To explore the materials best suited to stabilize the rapid surface oxidation of Galinstan and maintain flexibility in any device, a series of timed oxidation tests were implemented with a Hioki IM3570 Impedance Analyzer. Two liquid-metal droplets were formed on a strip of graphene and encased within the materials: Krylon Crystal Clear Acrylic Coating, Norland Optical Adhesive (NOA75), Polydimethysiloxane (PDMS, Sylgard Elastomer 184), Trimethylolpropane Triacylate (TMPTA), Bisphenol A Diflycidyl Ether Epoxy Resin, and Polyimide tape. Fig. 3.4 illustrates the total change in resistance of a graphene device with liquid-metal source and drain electrodes over a two-hour period.

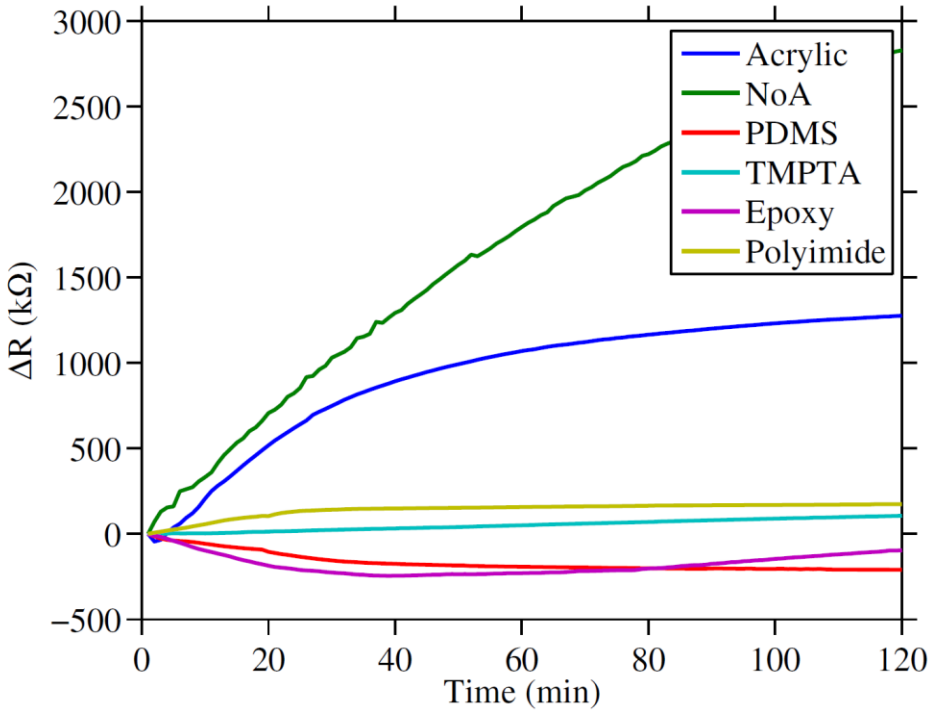

Fig. 3.4. Resistance change as a result of liquid-metal oxidation for a two-hour period in various encapsulating materials. ΔR represents the change in resistance with respect to total resistance of a test device

According to Fig. 3.4. NOA75 resulted in the quickest change in resistance for the two-hour experimental period and can be attributed to its moderate gas permeability that allowed oxygen to enter the liquid-metal cavity and promote oxidation. The quick change in resistance of the acrylic coating was attributed to the structural breaks in the acrylic film that allowed oxygen to enter the liquid-metal cavity since the film was applied in an aerosol form. PDMS and the epoxy resin exhibited a negative change in resistance and are believed to be a result of NaOH evaporation. In the event the NaOH evaporated slowly, the surface tension of the encapsulated Galinstan would degrad slightly; hence the result was an initial increase in contact area (decreased resistance) followed by additional oxide formation (increased resistance). The TMPTA showed a minimal resistance change (less than 100 ohms) over the two-hour period and is due to its much lower gas

permeability. This was an expected result for a material that exhibited solidified confinement, unfortunately, the rigidness of the solidified TMPTA did not allow for flexible operation and polyimide film was determined to be the best suited for our experiments as the change in resistance of the polyimide films was less than 170 ohms after 20 minutes and stabilized thereafter. The stabilization in the resistance change over time can be attributed to oxygen no longer having an effect oxide growth. An X-ray study of oxide layer growth on liquid-gallium surfaces demonstrated the oxide thickness saturates at ~5 °A [20]. This effect is interpreted in our results as an initial increase of resistance followed by resistance stabilization. The results from the oxidation tests are promising as polyimide films are currently used in many flexible devices and integration of such methods can be easily adopted by the current state of the art. Because of oxidation test, it is believed a combination of polyimide, electrolyte immersion, and an atmospheric controlled environment has the potential for complete elimination of oxide growth.

3.2. Graphene and liquid-metal electrodes

Liquid-metals enable mechanical strength independent of spatial position and the potential to minimize contact degradation under stress. On the other hand, Graphene provides a zero bandgap, tunable conductivity, and a high carrier mobility that is desirable in electronic devices such as the field-effect transistor (FETs). Coupling graphene and liquid-metals into fundamental electronic components like FETs can potentially overcome flexibility, weight, and size limitations of traditional platforms. The conformability of such integration may be influential in the electrical stability of future flexible electronic devices. Applications that can benefit from such integration can include Nanosat, Under-water autonomous vehicles, and Airborne platforms in which size and conformability are critical specifications that must be met by devices and sensors before deployment. The following sections explore the electronic properties of such integration.

3.2.1. Current issues with graphene contacts

Contact resistance is defined as the total resistance of a material that comes from the electrical leads and connections as opposed to the intrinsic resistance of a material under test. It is an important parameter that must always be understood when designing electronic interfaces and

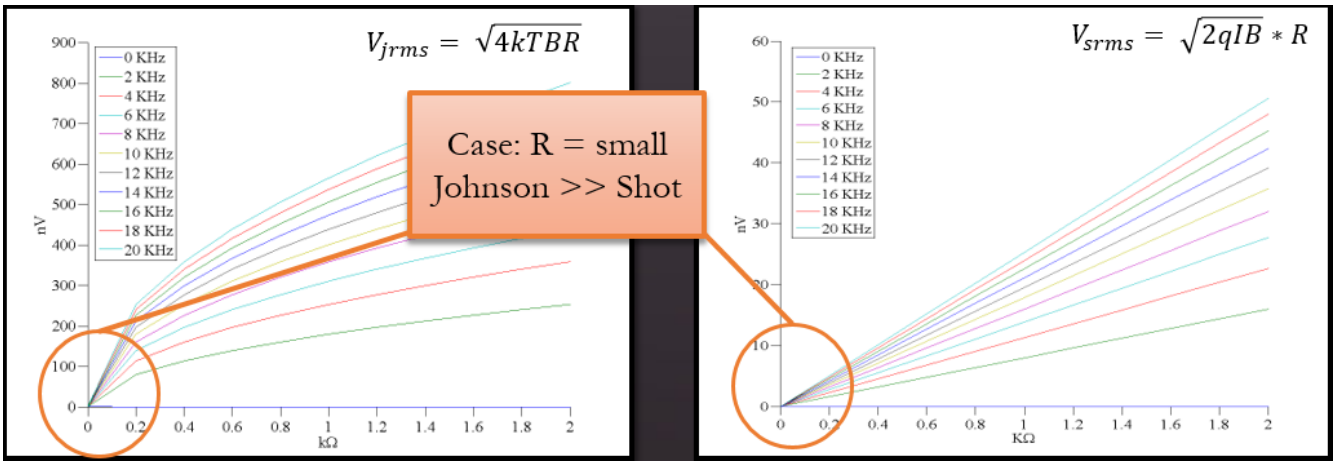

Fig. 3.5. (left) Johnson Noise as a function of noise bandwidth for a simple resistive element, T = 290K. (right) Shot Noise as a function of noise bandwidth for a simple resistive element, 100 nA input current. For small values of R, Johnson noise is the predominant noise source.

predicting noise sources. The quantification of contact resistance aids in the determination of noise sources that come about from its existence which may include *Johnson Noise* (thermal noise) and *Shot Noise* (Poisson noise). A side by side comparison of both noise sources in Fig. 3.5. illustrate that for a device with a reasonably small contact resistance, Johnson noise plays a predominant factor in device performance. In either case, the existence of even the slightest amount of contact resistance produces a significant voltage noise source. It is the responsibility of a designer to reduce contact resistance as much as possible, therefore, the designer can efficiently predict device operation.

Initial studies of graphene junction contact resistance demonstrate that contact resistance plays a crucial role in the mobility and overall device performance of a graphene electronic device [23].

For example, a graphene/metal interface that results in a high contact resistance will ultimately impede the flow of mobile charge carriers across the interface. The result is the inability of charge carriers to escape the graphene material to be electronically registered. Without proper registration of charge carriers, it may become difficult to measure the electronic and optical properties in a graphene device. A reduction in graphene contact resistance is of immense importance to the graphene scientific community as new embodiments of graphene devices may be enabled where a signal is typically weak.

There has been success with palladium and graphene interfaces to lower contact resistance [24]. However, high carrier mobility was only achieved when the proposed device was operated at a temperature of 6 Kelvin. At 6 Kelvin, mobile charges carriers can be assumed highly energetic that potential barriers at interfaces with high contact resistance will tend to look transparent to the mobile charge carrier. However, the power and heat requirements needed to operate such devices at such high temperatures make device techniques costly and unsuitable for commercial temperature ranges ($0℃ - 86℃$). In another attempt, the use of gold and titanium (Au/Ti) contacts were demonstrated with low contact resistances of ~500 Ωμm and is currently the method practiced in academic graphene devices [25], [26]. Despite many successes with Au/Ti contacts, titanium supplements initial steps in the fabrication process that can be costly and shown to be detrimental to the mobility characteristics of graphene. Such processing techniques can increase the probability of physical and or chemical damage to the graphene material. There is a need for a device material that can potentially mitigate the risk associated with processing graphene that will lower graphene contact resistance while remaining relatively easy and inexpensive to integrate.

3.2.2. A potential solution with graphene and liquid-metal electrodes

The fabrication of transistors requires a large amount of skill and preparation. In a standard integrated circuit foundry, an individual must first be trained on the large assortment of nano/microfabrication before even being allowed step foot in the facility. In addition, years of skill and experience are required in order to achieve the necessary tolerances that are currently a demand by today's electronics industry. However, despite the lengthy preparation and matured physical vapor deposition (PVD) processes, a coated surface is hardly flat after processing. At the micro-scale, surface roughness and contaminants dominate and protrude outward. At even smaller scales and in contact with two-dimensional materials small surface defects and protrusions can have detrimental effects on device performance.

As shown in Fig. 3.6(a), when two solid-metal/solid-metal surfaces come into contact, surface roughness limits surface-to-surface area contact. The result is high contact resistance due to current channels that are constricted to the minimal contact points (Illustrated by red dots in Fig. 3.6(a)). In a device, electrical contacts with high contact resistance produce noise and hinder performance.

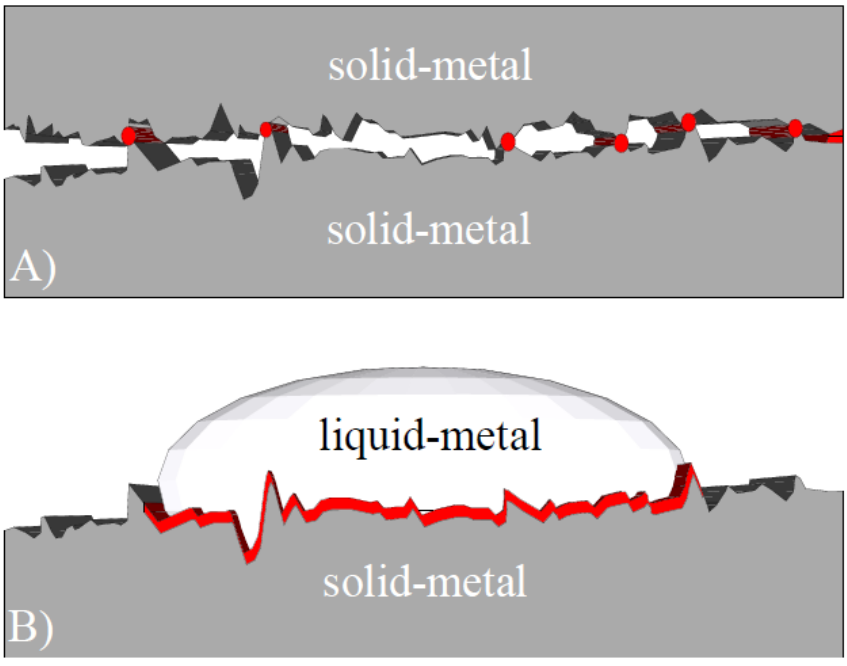

Fig. 3.6. (In Red) Difference in contact area for (a) solid-metal/solid-metal and (b) liquid-metal/solid-metal junction. In a solid-metal/solid-metal junction, the surface roughness limits the surface-surface contact area, whereas in a liquid-metal/solid-metal junction the liquid-metal conforms to the uneven surface topography and maximizes the overall contact area.

A fundamental understanding of metal junctions demonstrates that contact resistance R_c can be reduced by increasing the junction contact area A_c, where the effective resistivity of a contact material is ρ.

$$R_c = \frac{\rho}{A_c}$$

As shown in Fig. 3.6(b), liquid-metal alloys provide desirable surface adhesion properties that can accommodate surface topography and enable large-area surface coverage. The effects of contact degradation then become negligible in liquid-metal/solid-metal junctions as the deformation of a solid surface no longer compromises the contacting material when flexed. The result is a low-resistance conformal electrode that remains in constant contact with the underlying material despite flexure. In addition, the low bulk resistivity, $\rho = R_s * t$, of liquid-metals that allows for a large current carrying capacity that is required by many applications in which power loss is a critical performance factor.

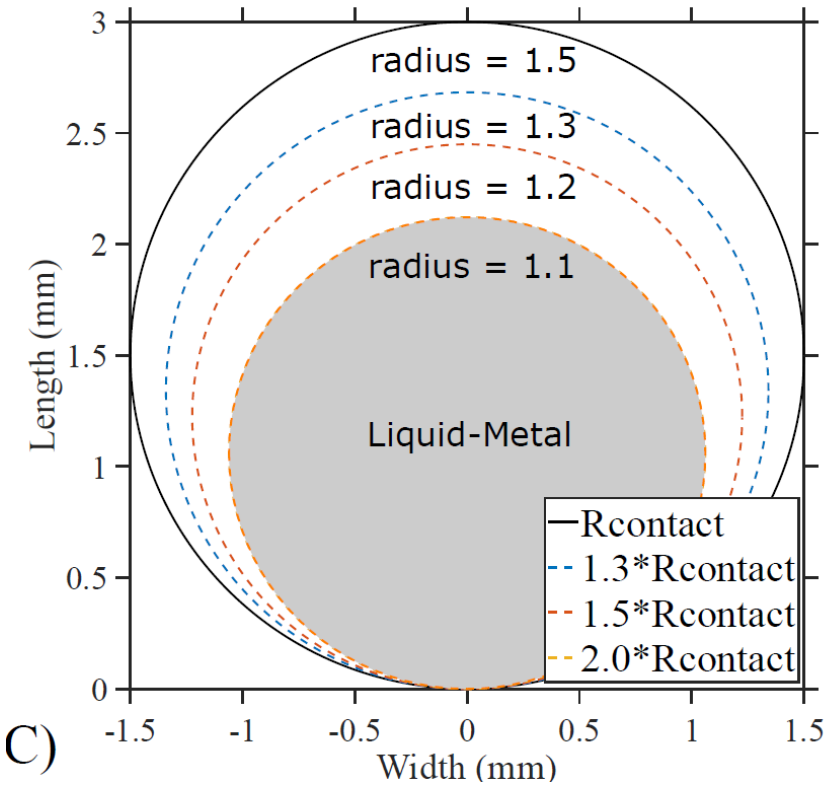

Fig. 3.7. Resistance as a function of surface area coverage for a liquid-metal electrode. Geometric changes in the liquid-metal electrode will result in variat ions in the contact resistance. Rcontact indictaed the ideal lowest contact resistance corresponding to the largest allowable radius.

Analogous to water droplets, liquid-metal alloys form spherical shapes due to high surface tension and the tendency for liquids to minimize surface area. In flexible cavities, liquid-metal electrodes try to reach spherical equilibrium, therefore, can deform or alter position during confinement as a direct response to geometrical changes within the cavity. Electrodes that are not stationary will than provide unsuitable device characteristics that are not predictable.

When designing devices with liquid-metal electrodes, it will become the responsibility of the design engineer to ensure that the area of the contacting material and the corresponding contact area of the liquid-metal/solid-metal interface remains constant under various conditions that may include pressure drive actuation or geometric changes in the encapsulating material. As a

demonstration, Fig. 3.7 illustrates variations in the geometric radius of a liquid-metal electrode within a maximum allowable contact radius of 1.5 mm. In the case that outside forces were to vary the geometry of a liquid-metal electrode, such as reduce the interfacial area, changes in geometry as small as 200 microns can have adverse negative effects on contact resistance.

3.2.3 An investigation of graphene and liquid-metal contact resistance

Liquid-metals provide a unique opportunity to investigate graphene contact resistance as liquid-metals exhibit similar electrical properties to traditional metals gold, aluminum, silver, and tungsten. However, liquid-metals have a unique capability to maintain a liquid state are room temperature. For example, liquid-metal Galinstan maintains a liquid state from$(-19℃\ to\ 1300℃)$ [13]. The following section demonstrates an initial study to measure contact resistance of liquid-metal electrodes with graphene in an effort to determine the feasibility of such integration.

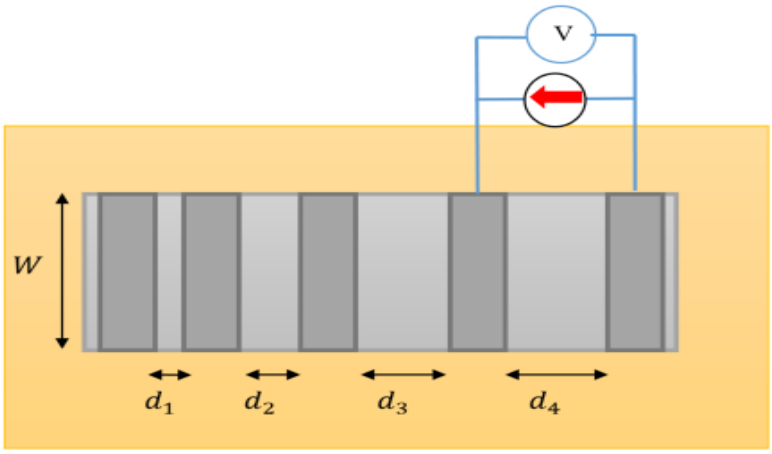

Fig. 3.8. Visualization of Transfer Length Method pattern. I-V measurements are made across adjacent electrodes with increasing distance between contacts.

Characterization of graphene with liquid-metal contacts was demonstrated with an industry standard transfer length measurement method (TLM) [27]. A typical TLM array consists of unequally (ascending) spaced source and drain electrodes with identical width and length. Fig. 3.8 illustrates a standard TLM array used for contact resistance measurements. For each pair of adjacent contacts of the TLM array, Current-Voltage (I-V) characteristics are measured using a

semiconductor parameter analyzer (Keithley 4155C), plotted, and the slope is fitted between each channel length to determine the total resistance R_T as the channel length spacing is increased. The total resistance is than defined as the summation of resistance of the bulk material plus the resistance of each graphene and liquid metal interconnect. The relationship for total resistance can then be plotted against increasing graphene channel length d as shown in Fig. 3.9 for which the linear relationship for R_T becomes

$$R_T = \frac{R_s}{w} d + 2R_c$$

where R_s is the sheet resistance of the material under contact, d is the graphene channel length between adjacent contacts, w is the width of each metal contact, and R_c is contact resistance of each graphene-metal interface. To extrapolate R_s and R_c a linear least square fitting is used and the slope and y- intercept of the linear fitting can be compared to the equation for R_T. The slope of the linear equation then provides the channel width normalized value of the sheet resistance and the y-intercept provides two times the contribution of the contact resistance.

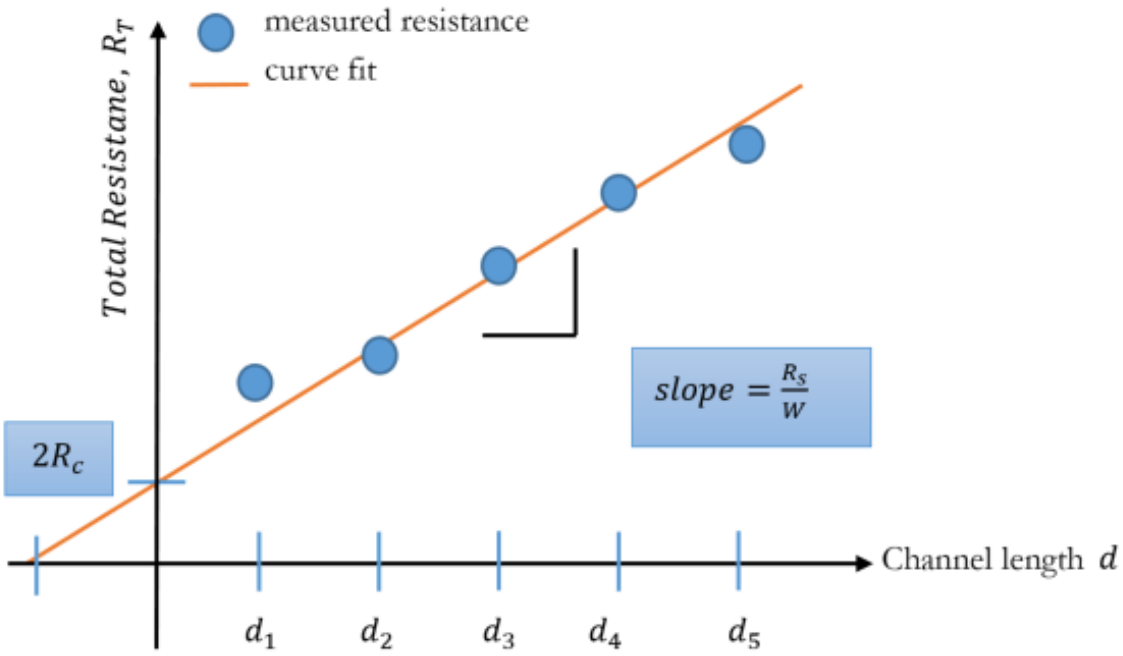

Fig. 3.9. Linear interpolation of the resistance versus graphene channel length. The y-intercept is 2x contact resistance and the slope derives the width dependent sheet resistance.

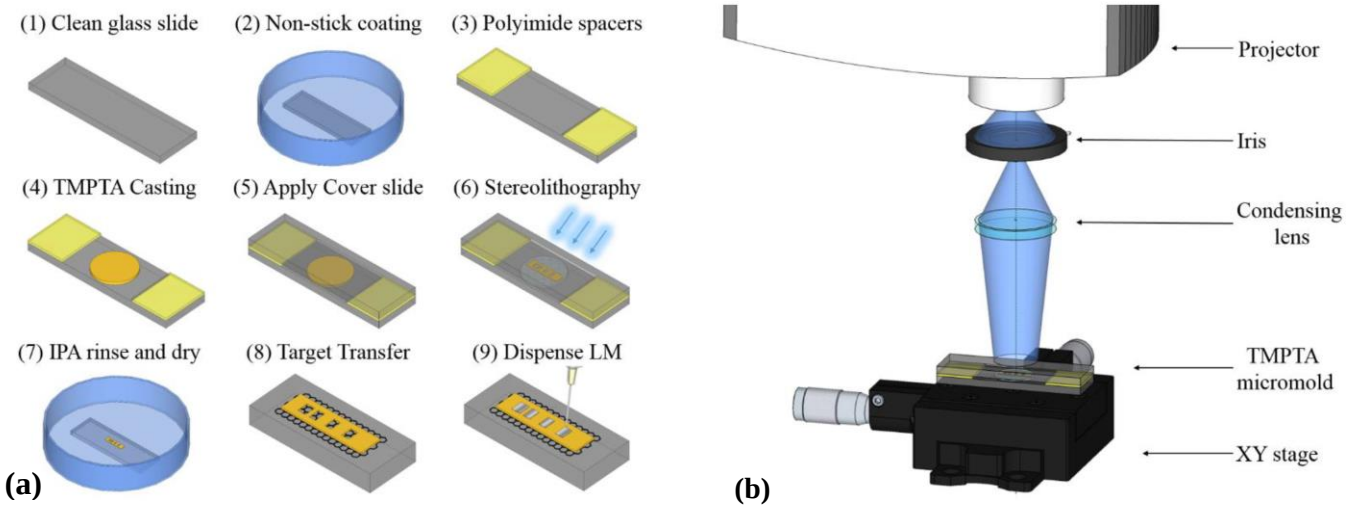

Fig. 3.10. (a) The fabrication process of TMPTA microstructures. (b) Diagraom of the photolithographic exposure system. An image is projected on TMPTA for ~50s. Illumications is controlled via a variable aperture stop (iris) and *focal length = 85mm* plano-convex lens.

3.2.3.1 Device Fabrication

Fig. 3.10 illustrates the fabrication process for the Trimethlylolpropane Triacrylate (TMPTA) microstructures necessary to isolate liquid-metal Galinstan on the surface of graphene for contact resistance measurements. A 75 x 25 mm^2 microscope slide was pre-rinsed in a solution of 5:1 DI water and surfactant, followed by a dry step, to apply a non-stick coatinguyr that would allow the easy removal of TMPTA microstructures after processing. Polyimide sticky films were then cut to size and TMPTA was carefully dispensed on the center of the microscope slide and sealed with a second microscope slide that was also dipped in surfactant. Photopolymerization of blue light (475 nm) sensitive TMPTA microstructures was achieved with a photolithographic setup illustrated in Fig 3.10. Various microstructures were designed in Adobe Illustrator CC and imported to Microsoft PowerPoint with 1920 by 1080 pixel resolution for projection. An Olympus 3 stereo microscope was used to inspect and adjust the final image focus to the desired distance away from the light source so that the edges of the projection came to a fine focus. The spatial resolution of the TMPTA microstructures was maximized by the high native resolution and intense color light output of the HD projector. This setup made it simple to optimize the amount of blue light exposure needed to accurately develop the TMPTA microstructures.

Once exposed, the remaining undeveloped TMPTA was removed with isopropyl alcohol (IPA), followed by a deionized water rinse, and drier step. The TMPTA structure was then manually removed from the glass microscope slide with fine tip tweezers and carefully aligned onto a graphene sample. Finally, the Galinstan was dispensed in each open cavity as shown in Fig. 3.11 with a 1.0 ml syringe. It was noted that a channel length of <400 micron could not be easily achieved due to various limitations such as the size of Galinstan droplets as each droplet exited the dispensing needle tip. Due to the complexity of dispensing the Galinstan by hand, structures on

the order of tens of microns will be investigated with an improved setup configuration and is discussed in Chapter 6.

Figure 3.11 Images of TMPTA microstructures fabricated for TLM experiment before (left) and after (right) Galinstan Injection.

3.2.3.2 Results

Current-Voltage (I-V) characteristics as a function of graphene channel lengths were made with an Agilent 4155C Semiconductor Parameter Analyzer and are illustrated in Fig. 3.12. To combat the fast oxidation of galinstan, tungsten micromanipulator probes were used to interface between the semiconductor parameter analyzer and test device electrodes, as tungsten is one of the few metals that do not exhibit oxidation in contact with Galinstan. The linear relationship of the I-V characteristics suggests that good contact was made with the Galinstan electrodes. However, Fig. 3.12 illustrates that the I-V characteristics for channel lengths 450, 475, and 500 vary by only a few hundred nanoamps. It is believed that the uncertainty in the graphene quality between the channel lengths could possibly result in variations in the total resistance, as the total resistance is a summation of the material resistance and contact resistance of each metal-semimetal interface.

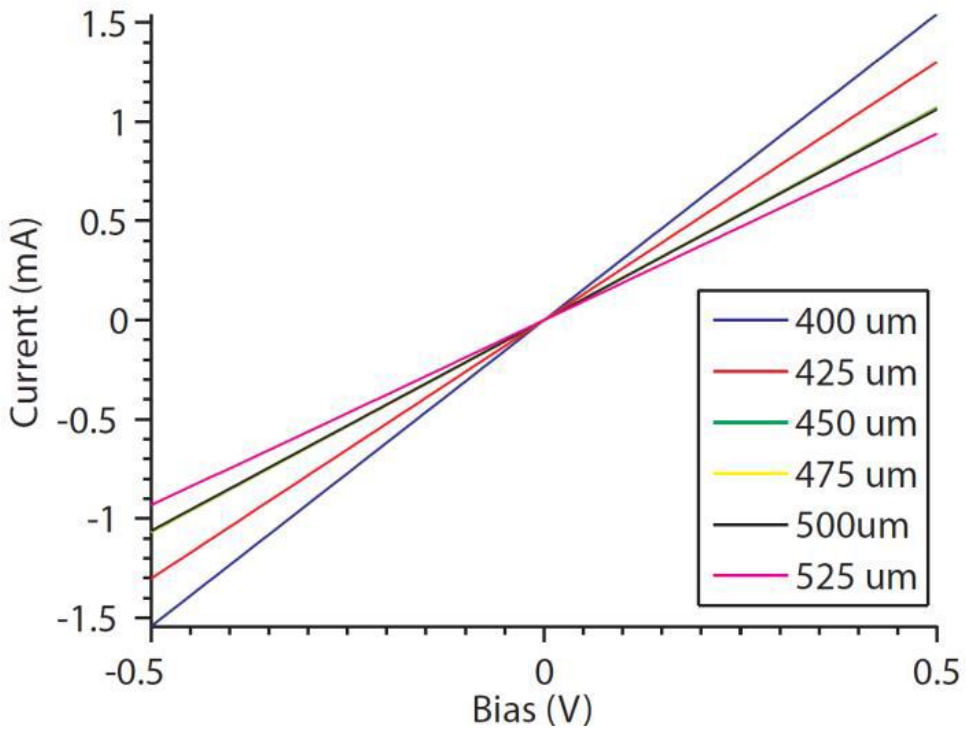

Fig. 3.12. Current-voltage (I-V) characteristics as a function of channel distance for TMPTA TLM Pattern

In the case that the graphene resistance does not change for the entire length of the TLM pattern, results would indicate transfer characteristic that are equally spaced amongst increasing channel distance. The uncertainty in graphene quality made it difficult to find samples in which the total resistance always increased with channel size. In some samples, adjacent pairs of liquid-metal electrodes exhibited very large resistance differences on the order of a ~Mega ohms and there is a reason to believe the TMPTA microstructures were placed on a graphene boundary. There needs to be further study of graphene quality after the Galinstan electrodes have been deposited. However, methods such as Raman

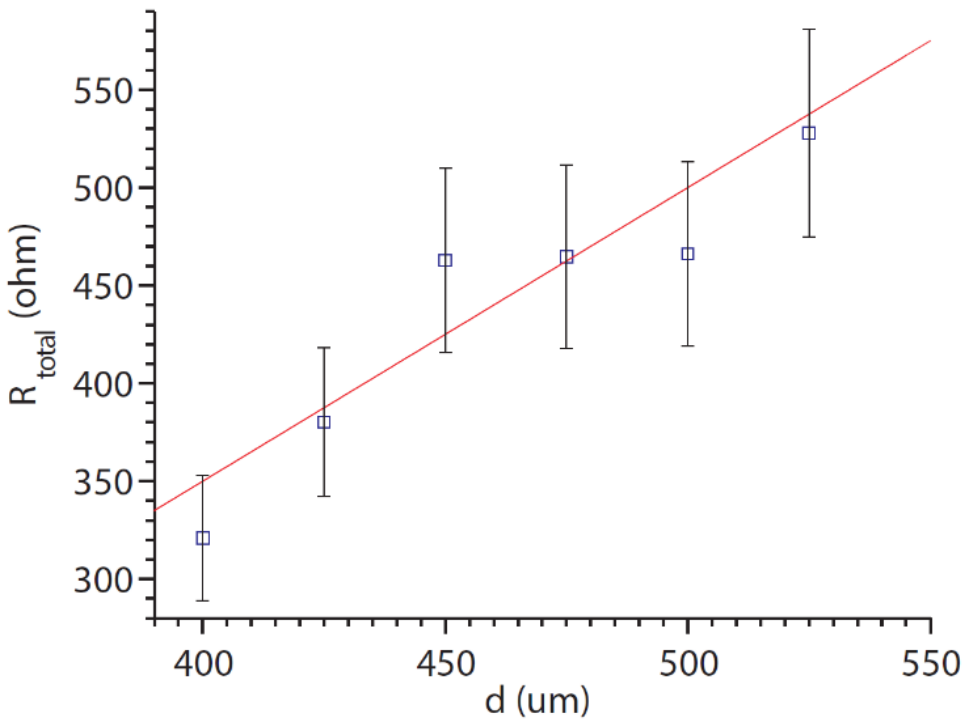

Fig. 3.13. Total Resistance as a function of channel distance. Channel width normalized sheet resistance and contact resistance was determined from a linear least squares fitting(red)

Spectroscopy may fail in this configuration as Galinstan is highly reflective and may suffer from Rayleigh scattering.

The total resistance was extracted from the I-V characteristics in Fig. 3.12 and plotted against increasing graphene channel length in Fig 3.13. A MATLAB program was then written to execute a least square fitting on the data series to extract the contact resistance and sheet resistance discussed in the transfer length method section. A measured contact resistance of -124±28 Ω and a sheet resistance of 591±28 Ω/sq was found for a contact width of 500 microns which is in line with other measurements for the sheet resistance of graphene.

3.2.3.3 Discussion

The failure of the TLM method to measure a positive contact resistance is an implication that interfacial chemical doping may occur at the graphene and liquid-metal interface as discussed in [28] for Ag-graphene contacts. However, unlike [28] our configuration does not operate via electrostatic gating and the negative contact resistance phenomena cannot be simply explained by the electric field-effect of graphene. Negative contact resistance suggests that Galinstan may promote chemisorption and shift the graphene Fermi level beyond the dirac point and influence the overall carrier concentration. Therefore, further investigation is needed to investigate useful figures of merit for resistivity, doping type, and mobility. The goal of future investigation will be to determine the carrier type and quantify the carrier concentration.

3.3 Towards flexible graphene devices with conformal electrodes

The conformability of liquid-metals combined with the conductivity and inertness of carbon nanomaterials enables electrical stability for a variety of contours. In the following section, we conducted a series of bend tests to determine the robustness of such integration. We first describe the architecture and fabrication of a two-terminal graphene device with liquid-metal electrodes followed by an incremental and bend cycle test. The remaining section provideS a discussion of the bend test.

3.3.1 Device Fabrication

A simple two-terminal device with no physical gate was fabricated to explore the feasibility of a graphene flexible device integrated with liquid-metal conformal electrodes. The complexity of the device remained simple, therefore, flexure parameters could be easily extracted from bend-test experimental results without altering the electronic state of the graphene. However, alternate embodiments of such a device can be fabricated to alter the electronic state of graphene that

includes a single top-gate, a dual-gated device, or any transistor configuration in which liquid-metal can be used to alter the electronic state of graphene. Chapter 4 will focus on a three-terminal configuration that will explore actuating the conductivity of the graphene monolayer for the purpose of a flexible 3-terminal graphene field-effect transistor (GFET).

Fig. 3.14(a) and (b) illustrate a two-terminal graphene device with liquid-metal conformal electrodes used in the bend-test experiments. First, chemical vapor deposited (CVD) graphene synthesized on a copper catalyst was commercially transferred onto Polyethylene Terephthalate (PET). PET was chosen as a bulk-substrate due to its bendability and the manageable substrate thickness which made it fairly easy to cut the samples to a desired width and length with standard cutting tools. Alternatively, solid bulk-substrates can be chosen and may include doped and un-doped silicon, silicon/SiO2, silicon/HfO2 (hafnium oxide), silicon/AlO2 (aluminum oxide), nickel, and boron nitride. However, neither of the substrates allow for flexible operation and will not be suitable for bend-test experiments described in these sections.

Graphene quality on PET was determined with a $532nm$ Confocal Raman Spectroscopy system. The measured Raman spectroscopy profile of the graphene sample allowed the quality and number of layers to be determined via the peak amplitude of the defect band

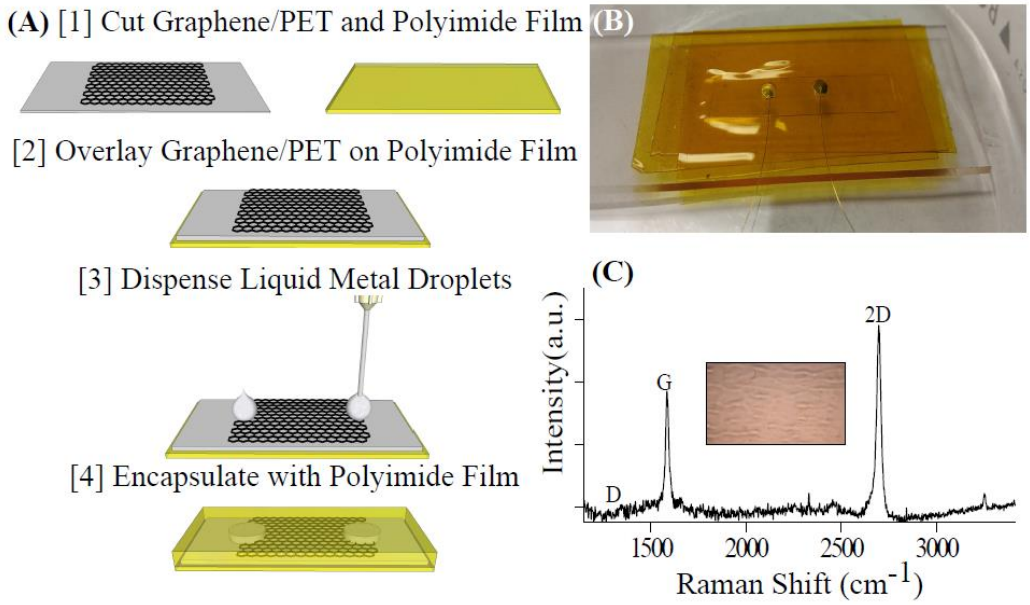

Fig. 3.14. Device Fabrication: (a) Fabrication process of (b) graphene flexible device with liquid-metal electrodes. (c) 532nm Raman spectrum of monolayer graphene transferred to polyethylene terephthalate substrate. Note that the *2D* band is greater than the *G* band and features a full-width at half maximum of ~26 cm^{-1}, which indicates that the sample is a monolayer of graphene. Also, the absence of the *D* band near 1350 cm^{-1} indicates the lack of defects in the monolayer graphene sample.

D, and an analysis of the peak intensity ratio of the $2D$ and G Bands. Fig. 3.14(c) illustrates the graphene monolayer is of high quality with minimal defects because the peak intensity of the $2D$ Band is two times greater than the peak intensity of the G Band ($I_{2D}/I_G \approx 2$)and the absence of a D Band peak states the graphene monolayer has minimal defects. Once the quality of graphene was determined, the graphene sample was overlaid on a polyimide film and prepared for Galinstan injection.

Before injection, Galinstan was stored in a solution of 1% NaOH (Sodium Hydroxide) and de-ionized water to preclude the fast oxidation of Galinstan in air. The NaOH prevented gallium oxide formation on the surface of the Galinstan electrode which if present would promote numerous disadvantages during testing. For example, it would rapidly lower the surface tension of Galinstan

material and cause problems during transport such as adhering to the barrel of a syringe that is typically needed for drop casting [12]. In addition, the oxide barrier would demonstrate undesirable insulative properties that may promote schottky or capacitive properties at the graphene and liquid-metal interface.

A Galinstan droplet of $0.6mm^3$ was quickly dispersed with a blunt-tip syringe needle onto the graphene boundaries to form the source and drain electrodes. Tungsten wires with diameters of $0.127mm$ were then embedded within the Galinstan electrodes to enable quick connectivity with external measurement devices. Tungsten wires were chosen due to its non-reactivity with Galinstan. A polyimide film was then used to encase the Galinstan electrode to further preclude the formation of gallium oxide. This technique can easily be applied to a microfluidic platform into which Galinstan can be actuated electrically or injected with an advanced pipetting system.

3.3.2 Experimental Set-up

The device was tested with a self-constructed bend test apparatus shown in Fig. 3.15(a). The bend test apparatus consisted of two Newport linear translational stages integrated with corresponding Newport linear high-precision motorized micro-positioners. Two miniature optical rails were used to hold the device-under-test at adjacent ends and a strain was applied from 0-2.5% with a Newport ESP301 Motion controller, corresponding to a minimum bend radius of 4mm, with a user-defined LabVIEW automation algorithm.

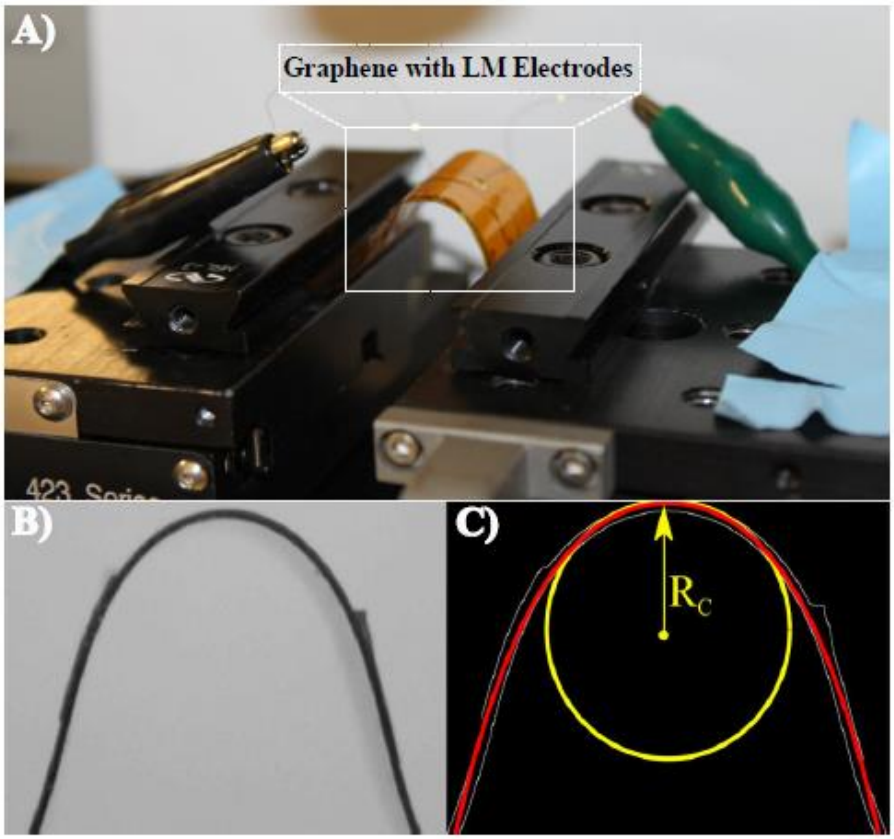

Fig. 3.15. Experimental setup: (a) Graphene flexible device with liquid-metal electrodes encapsulated in polyimide after bending, and (b) illustration of quartic polynomial regression (In red) used to find a (c) best fit osculating circle (In yellow) with the corresponding radius of curvature R_c.

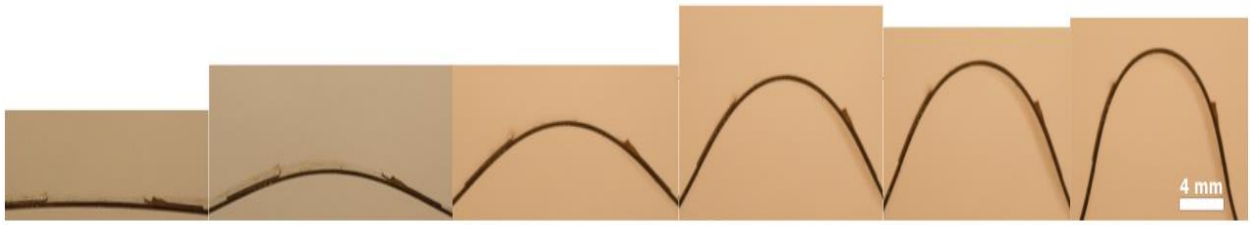

Fig. 3.16. Bend Test Images

The radius of curvature (bend radius) was extrapolated from individual bend test images similar to the images in Fig. 3.16, of each bend radii captured with a Canon Digital Single-Lens Reflex (DSLR) camera integrated with a 50mm lens. An image processing technique written in MATLAB consisted of an edge detection algorithm and quartic polynomial regression that was used to determine the best fit osculating circle and the corresponding radius of curvature. The strain was then computed and given by $\epsilon = y/R_c$ where y is the distance from the neutral axis and R_c is the radius of curvature. Fig. 3.15(b) and (c) illustrates our experimental setup along with the image processing techniques.

3.3.3 Incremental Bend Test

The device was mounted in the bend test apparatus described in the previous section and the bend radius was incremented from flat (no strain) to 4mm under standard atmospheric conditions and pressure. Current-voltage (I-V) measurements were made with an Agilent 4155C Semiconductor Parameter Analyzer for each bend radius, averaged, and then fitted in MATLAB to extrapolate the total resistance between liquid-metal electrodes. Fig. 3.17 illustrates the change in resistance as a function of applied strain and bend radius. The resistance was relatively unchanged (less than 1%) for curvatures as small as 4mm. Any slight increases in resistance were attributed to observable stresses on the polyimide cavities that caused the ceilings of the cavities to collapse and displace the bulk of the liquid-metal structure away from the graphene surface as the liquid-metal shift position in the cavity. The result was a decrease in the graphene surface area coverage and an increase in the two-terminal resistance.

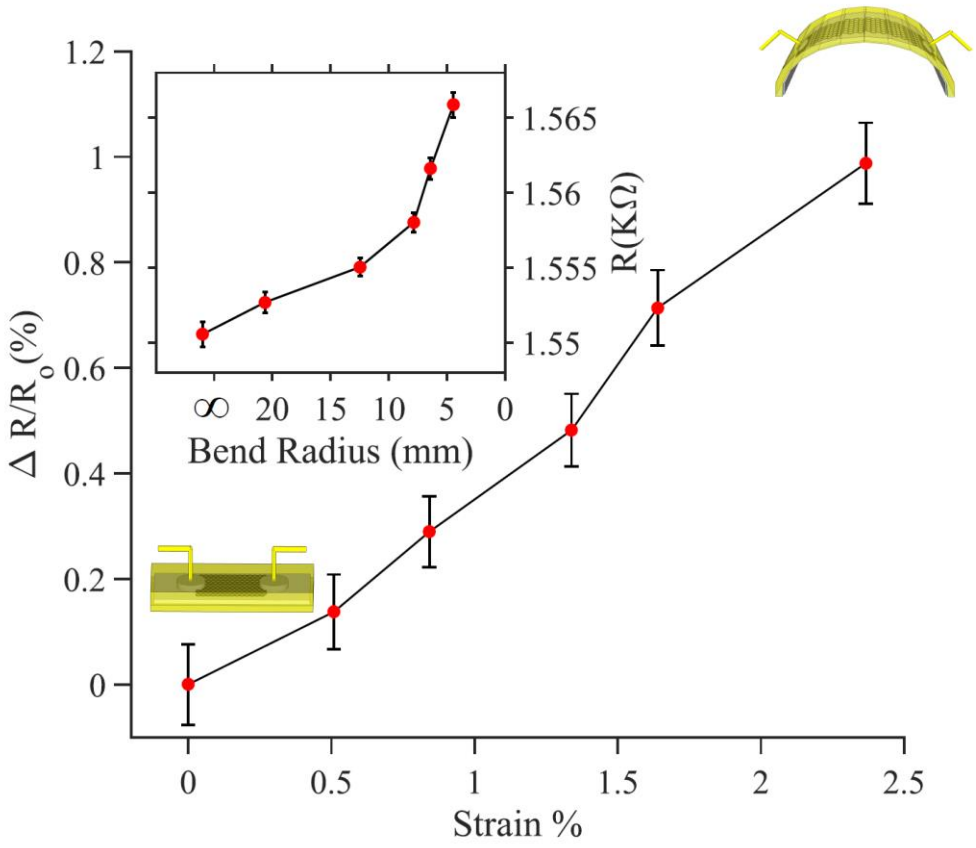

Fig. 3.17. Normalized change in resistance as a function of the applied strain. The inset illustrates the two-terminal resistance as a function of bend radius. R_0 represents the total resistance of the two-terminal device in a flat position and ΔR represents the difference in resistance of the bent position with respect to the flat position for the two-terminal device

It is important to note the best results were achieved when the surface area of the liquid-metal electrode remained constant with respect to the graphene area for the entirety of a single bend cycle and as was discussed in Section 3.2.2. In devices where the liquid-metal did not fill the cavity entirely, un-expected results persisted such as resistance measurements that did not increment with smaller bend radius. This was attributed to constant changes in the position of the liquid-metal electrode inside the polyimide cavity when deformed. Therefore, it was important to inject the correct volume of liquid-metal in each cavity. An alternative method would be to encapsulate the liquid-metal electrode in polydimethylsiloxane (PDMS) or similar elastomers that can solidify and

seal the electrode in its position above graphene. In the worst-case scenario, the polyimide film would separate from the PET substrate and a release in pressure would force the liquid-metal outside the device from any openings. This effect was attributed to poor adhesion between the PET substrate and the polyimide film. Bond strength can be improved via additional techniques such as plasma treatment and soft lithography [29].

It is important to note that unexpected operation only occurred when liquid-metal was displaced from the graphene material. If the surface area of the interconnect remained constant, the change in resistance was negligible. An added benefit of such intergration is that the liquid-metal displacement is reversible, and a low resistance interconnect is restored once the liquid-metal electrode returned to its original contact position. In standard devices that integrate rigid interconnects, such as in thin film transistors, typical PVD based interconnects can peel or tear graphene from a bottom substrate, therefore, irreversibly destroying the device.

3.3.4 Bend Cycle Test

Graphene and Liquid-metal interconnects enable conformal devices for a variety of contours that can include wearable electronics for defense applications and biomedical devices. However, such applications require a bendable operation for repeated uses. To demonstrate the robustness of the graphene and liquid-metal interconnects under repeated strain, the device was subjected to multiple bend cycle tests under standard atmospheric conditions and pressure. Similar to the incremental bend test, current-voltage (I-V) measurements were captured with SPA, averaged, and a MATLAB algorithm was implemented to extrapolate the two-terminal resistance. Fig. 3.18 illustrates the change in resistance as a function of bend

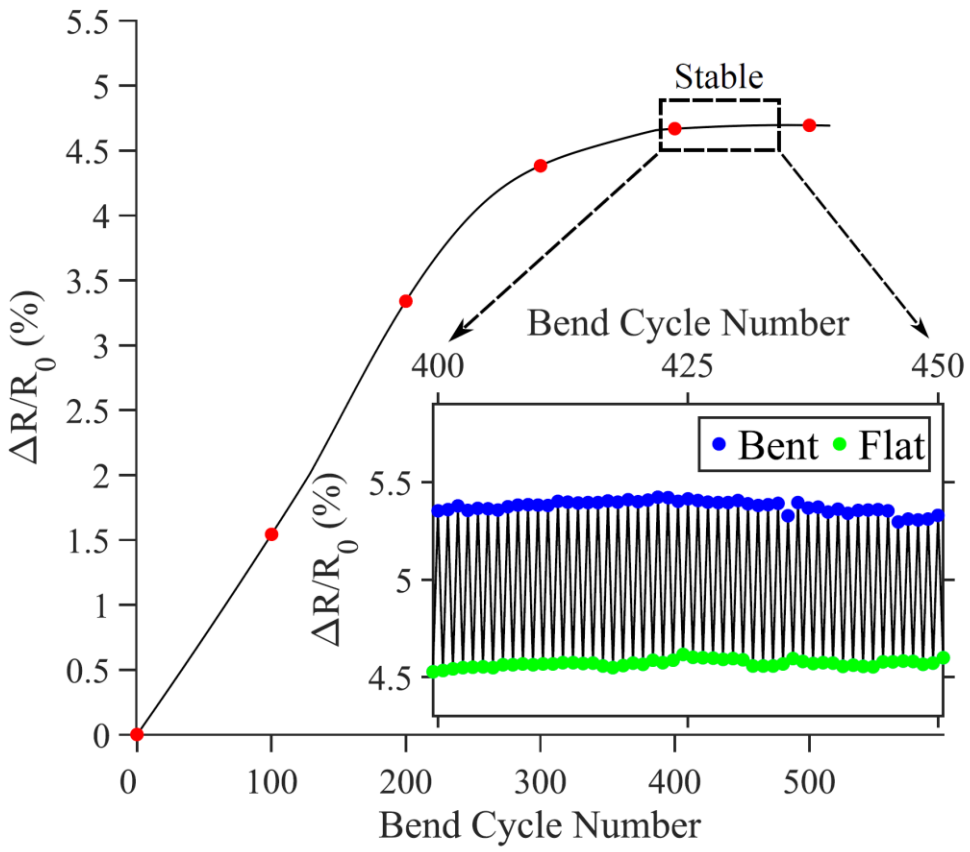

Fig. 3.18. Normalized change in resistance as a function of bend cycle number. The inset illustrates the change in resistance as a function of 50 bend cycles when Galinstan oxidation has stabilized.

cycle number for a total of 500 bend cycles.

A nonlinear regression was fitted about the mean to illustrate any trends in the total change in resistance over continual bending. Subsequent bend cycles exhibited a total change in resistance of less than 5.5% and are believed to be mainly and effect of Galinstan oxidation and are illustrated in Fig. 3.18 as an initial rising trend. In future devices, the effects of oxidation can be reduced by a combination of techniques discussed that can include the following: electrolyte immersion or hermetically sealing the device in an atmospherically controlled environment.

As Galinstan oxidation stabilized, a less than 1% change in resistance was exhibited due to continual bending and is illustrated by the inset of Fig. 3.18. These results were repeatable for

multiple devices. The ability of graphene and liquid metal interconnects to sustain contactover repeated bend cycles is an ideal result as such integration can be implemented in flexible devices.

3.3.5 Discussion

In this section, we addressed the fundamentals of graphene and liquid-metal electrodes for electronic devices. Furthermore, the advantages and disadvantages of such integrations. Flexible devices fabricated with PVD based electrodes typically suffer from irreversible damage due to surface delamination and wrinkling at high flexures. An additional unsolved problem is the alteration of the intrinsic properties of graphene as a result of the gases and sacrificial layers used in PVD.

Liquid-metals, such as Galinstan, offer the conformal properties of a liquid and the conductive properties of a metal without processing. With these properties, a two-terminal graphene flexible device with Galinstan electrodes achieved strain resilience up to 5.5% that was mainly due to Galinstan oxidation. As Galinstan oxidation stabilized a less than 1% change in resistance was exhibited thereafter with a smallest bend radius of 4mm. The limitations imposed by the oxidation of Galinstan were evident by a resistance increase over time as the exposed surfaces reacted with environmental oxygen. However, these limitations can be circumvented if additional techniques to hermetically seal the environment are adapted in future embodiments of our techniques.

The ability of liquid-metals to be reconfigurable under high strain enables numerous opportunities for inexpensive microfluidics and self-healing, wearable electronics that maintain desirable power handling provided by liquid-metals and graphene. As liquid-metal electrodes are scaled to the system level for graphene electronics, designers can form nontoxic, microfluidic integrated circuit systems at the nanoscale. This will enable numerous applications in bioelectronics, flexible displays, microelectromechanical systems, durable actuators, and power ICs. A refinement of the

liquid-metal encasement technique is needed, as this section demonstrates the simplest embodiment (two-terminal device) of graphene with liquid-metal electrodes. The following section will explore a three-terminal configuration of graphene field-effect transistor with liquid-metal electrodes. The goal is to demonstrate an inexpensive embodiment of a graphene field-effect transistor with robust and bendable operation comparable to the state-of-the-art graphene transistors.

REFERENCES

[1] J. Che, T. Cagin and W. A. Goddard III, "Thermal conductivity of carbon nanotubes," *Nanotechology,* vol. 11, no. 2, p. 65, 2000.

[2] A. K. Geim and K. Novoselov, "The rise of graphene," *Nature Nanomaterials,* vol. 6, no. 3, pp. 183-191, 2007.

[3] J. Ryu and et al., "Fast synthesis of high-performance graphene films by hydrogen-free rapid thermal chemical vapor deposition," *ACS Nano,* vol. 8, no. 1, pp. 950-956, 2014.

[4] X. Wang and et al., "A spectrally tunable all-graphene-based flexible feild-effect light emitting device," *Nature Communications,* vol. 6, 2015.

[5] H. Y. Jeong and et al., "Graphene Oxide thin films for flexible nonvolatile memory applications," *Nano letters,* vol. 10, no. 11, pp. 4381-4386, 2010.

[6] G. A. Salvatore and et al., "Wafer-scale design of lightweight and transparent electronics that wraps around hairs," *Nature Communications,* vol. 5, 2014.

[7] A. Pospischil and et al., "CMOS-compatible graphene photodetector covering all optical communication bands," *Nature Photonics,* vol. 7, no. 11, pp. 892-896, 2013.

[8] J. Fan, "Investigations of the influence on graphene photodetector by using electron-beam and photo-lithography," *Solid State Communications,* vol. 151, no. 21, pp. 1574-1578, 2011.

[9] R. Wong and et al., "Flexible microfluidic normal force sensor skin for tactile feedback," *Sensors and Actuators A: Physical,* vol. 179, pp. 62-69, 2012.

[10] G. Maltezos and et al., "Tunable organic transistors that use microfluidic source and drain electrodes," *Applied Physics Letters,* vol. 83, no. 10, pp. 2067-2069, 2003.

[11] "Mercury Hazards," *National Council for Occupational Safety and Health,* 30 April 2016.

[12] T. L. Liu and et al., "Characterization of liquid-metal Galinstan for droplet applications," in *Micro Electro Mechanical System (MEMS), 2010 IEEE 23rd International Conference on IEEE,* 2010.

[13] X. Liu and et al., "Non-toxic liquid metal microstrip resonators," in *Microwave Conference, 2009. APMC 2009,* Asia Pacific. IEEE, 2009.

[14] A. f. T. S. a. D. Registry, "Managing Hazardous Materials Incidents Mercury (Hg) CAS 7439-97-6 UN 2024 (liquid compunds)," U.S. Department of Health and Human Services, Public Health Service, Atlanta, GA, 2001.

[15] L. Van der Pauw, "A method of measuring the resistivity and Hall coefficient on lamellae of arbritrary shape," *Phillips Technical Review,* vol. 20, pp. 220-224, 1958.

[16] "Four-Probe Resistivity and Hall Voltage Measurements with Model 4200-SCS," *Keithley Appl. Note 2475,* pp. 1-8, 2011.

[17] P. L. Rossiter, "The electrical resistivity of metals and alloys," *Cambridge Universisty Press,* 1991.

[18] "Geratherm medical ag, safety datasheet acc, to guideline 93/112/ec.".

[19] K. Kandidatprograpmmet, "Reactivity of Galinstan with Specific Transition Metal Carbides," 2014.

[20] P. Ahlberg and et al., "Graphene as a Diffusion Barrier in Galinstan-Solid Metal Contacts," *IEEE Transactions on Electron Devices,* vol. 61, no. 8, pp. 2996-3000, 2014.

[21] T. Lifang and et al., "Design of catalytic substrates for uniform graphene solid-metal to liquid metal," *Nanoscale,* vol. 7, no. 20, pp. 9105-9121, 2015.

[22] R. Gough, "Continious electrowetting of non-toxic liquid metal for RF applications," *Access, IEEE,* vol. 7, no. 20, pp. 9105-9121, 2015.

[23] K. Nagashio and et al., "Metal/graphene contact as a performance killer of ultra-high mobility graphene analysis of intrinsic mobility and contact resistance," in *Electron Device Meeting (IEDM), 2009 IEEE International. IEEE*, 2009.

[24] H. Zhong and et al., "Realization of low contact resistance close to theoretical limit in graphene transistors," *Nano Research,* vol. 8, no. 5, pp. 1669-1679, 2015.

[25] K. Nagashio and et al., "Contact Resistivity and current flow path at metal/graphene contact," *Applied physics Letters,* vol. 97, no. 14, p. 143514, 2010.

[26] L. Ju and et al., "Graphene plasmonics for tunable terahertz metamaterials," *Nature Nanotechnology,* vol. 6, no. 10, pp. 630-634, 2010.

[27] A. Venugopal and et al. , "Contact resistance in few and multilayer graphene devices," *Applied Physics Letters,* vol. 96, no. 1, p. 013512, 2010.

[28] R. Nouchi, "Observation of negative contact resistance in graphene graphene field-effect transistors," *Journal of Applied Physics,* vol. 111, no. 8, p. 084314, 2012.

[29] M. A. Eddings and et al., "Determining the optimal pdms-pdms bonding technique for microfludic devices," *Journal of Micromechanics and Microengineering,* vol. 18, no. 6, p. 067001, 2008.

4. Technical Execution of Dissertation

Per the 2015 International Technology Roadmap for Semiconductors [1] (ITRS, a report put together by a collaboration of the world's major semiconductor associations), the year 2021 is the predicted year for the end of "Moore's Law." Moore's Law is defined as the fundamental idea that the number of transistors per silicon integrated circuit will double every two years. The ending of this fundamental idea will define a turning point in history because it will no longer be economically viable to shrink transistors beyond their current physical limit. There is a critical need to identify new materials and new transistor architectures that will revitalize the semiconductor industry.

In the following sections, the author demonstrates a novel graphene transistor architecture as an alternative to silicon-channel metal-oxide-semiconductor field-effect transistors (MOSFETs). The device is called a liquid-metal graphene field-effect transistor *(LM-GFET).* As noted in Chapter 1, the ultrahigh carrier mobility and atomic thickness of graphene can lead to numerous advantages over silicon-based transistors such as tunable conductivity and planar architecture. In addition, the conformability of liquid-metal electrodes enables reproducible low-resistance interconnects to graphene, without damage to the graphene layer. Applications of an LM-GFET will be provided in Chapter 5 by integration of the architecture with semi-conducting quantum dots and a PN junction embodiment.

4.1. Review of MOSFETs

Before we get into the study of a flexible graphene field-effect transistor (GFETs) architecture, it is important to note the fundamental operation of a traditional field-effect transistor known as a MOSFET. Fig. 4.1 illustrates the standard architecture of silicon-based MOSFET and is comprised of a source, drain, and gate electrodes that are separated from a bulk substrate (In Fig. 1 a p-type

silicon substrate) by a dielectric material. An applied voltage across the gate and bulk substrate of the MOSFET can generate an electric field-effect that will stimulate an inversion layer through the depletion region of the bulk material in which carriers can flow from the source to drain electrode. For example, in a n-type MOSFET (nMOS), a fabrication engineer may dope the bulk substrate with hole carriers (p-type) and then dope the source and drain electrodes with an excess of electrons (n++) via ion implantation. The application of a gate bias will than stimulate an inversion layer between the source and drain electrode that allows electron current to flow. Furthermore, careful control of the amplitude of the gate-bias can modulate the overall conductivity through the channel. The opposite is true for a p-type MOSFET (pMOS).

There are three main operational modes of standard MOSFETs:

1. Subthreshold. Operational mode in which the gate-source voltage V_{gs}) is below the threshold voltage V_{th}, also known as the minimal value of (V_{gs}) in which enough charge carriers will accumulate in the depletion region to form a conducting channel. In this mode, carrier flow is negligible and only those carriers that are thermally excited are transferred through the channel.
2. Linear. Operational mode in which the (V_{gs}) is above V_{th}. In this mode, an inversion layer is formed and current begins to flow between source and drain. The amount of drain current I_D that flows is governed by the following relationship:

$$I_D = u_n C_{ox} \frac{W}{L}(V_{gs} - V_{th})V_D$$

Where u_n is the mobility, C_{ox} is the gate capacitance, $\frac{W}{L}$ is the width to length ratio, and V_D is the drain voltage. Manipulating V_D in this mode will increase the drain current.

3. Saturation. Operational mode in which $V_D \gg V_{gs}$. In this mode, current saturates because the channel is pinched off at the drain electrode and V_D no longer affect the channel conduction. Current in saturation mode is given by [2]:

$$I_{D,sat} = u_n C_{ox} \frac{W}{2L} \left(V_{gs} - V_{th}\right)^2$$

In either mode, V_{gs} plays a significant role on the channel conduction properties. Therefore, to characterize the performance of a MOSFET, the expression for transconductance is used. Transconductance g_m is defined as the ratio of change in the output current I_D to the change in the gate voltage. Units are typically in siemens or amperage per volts.

$$g_m = \left.\frac{\delta I_D}{\delta V_{gs}}\right|_{V_D = constant}$$

The value of g_m corresponds to the gain of the MOSFET. A device that exhibits a large g_m can deliver a large gain assuming all other parameters are held constant [2, 3].

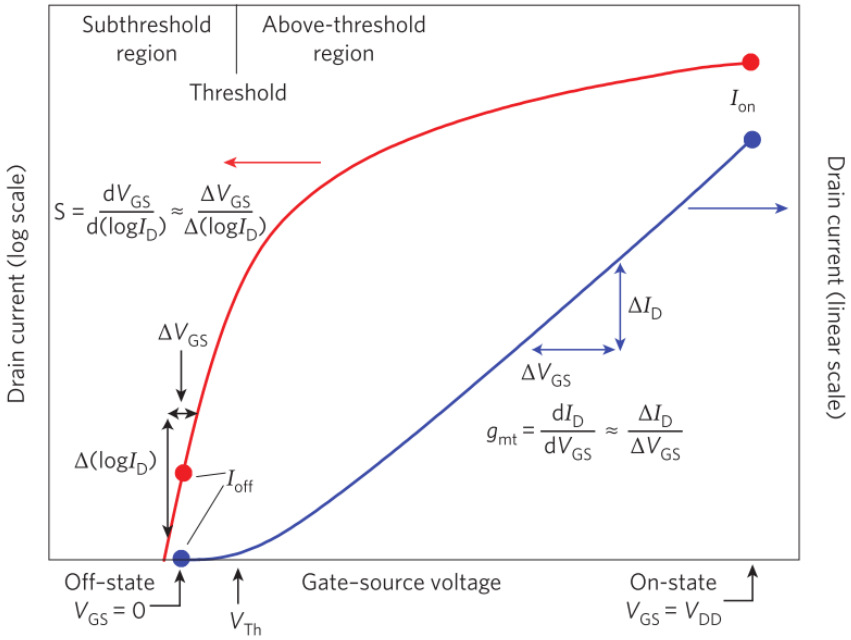

Fig. 4.1. Field-effect transitor transfer characteristics:
Drain Current as a function of gate-source voltage V_{gs} [3].

4.2. Liquid-metal and Graphene field-effect transistors *(LM-GFETs)*

Since graphene does not exhibit a bandgap, it does not operate by the means of stimulating an inversion layer in the bulk material. Rather, in a graphene field-effect transistor (GFET), the graphene material becomes the conductive channel and small changes by either electrostatic or chemical doping alter the material conductivity. For this reason, a GFET will not have an off-state and will suffer from low static power consumption. Therefore, recent graphene research has shifted towards radio-frequency devices that are unique in that they can operate in an on-state and radio frequency signals that are to be amplified are superimposed on a DC gate-to-source voltage [3]. In a embodiment of a graphene RF detector, graphene was separated from Complementary metal-oxide-semiconductor field-effect transistor (CMOS) architecture via a dielectric material. Exposure of a RF signal on the graphene surface allowed surface charge to generate, therefore, the opposite polarity could be measured capacitively with an on-chip CMOS differential amplifier [4]. It was determined the act of stimulating graphene with a RF signal manipulated the surface conductivity of graphene, therefore, alter the measured differential voltage measured by a CMOS amplifier Fig. 4.2.

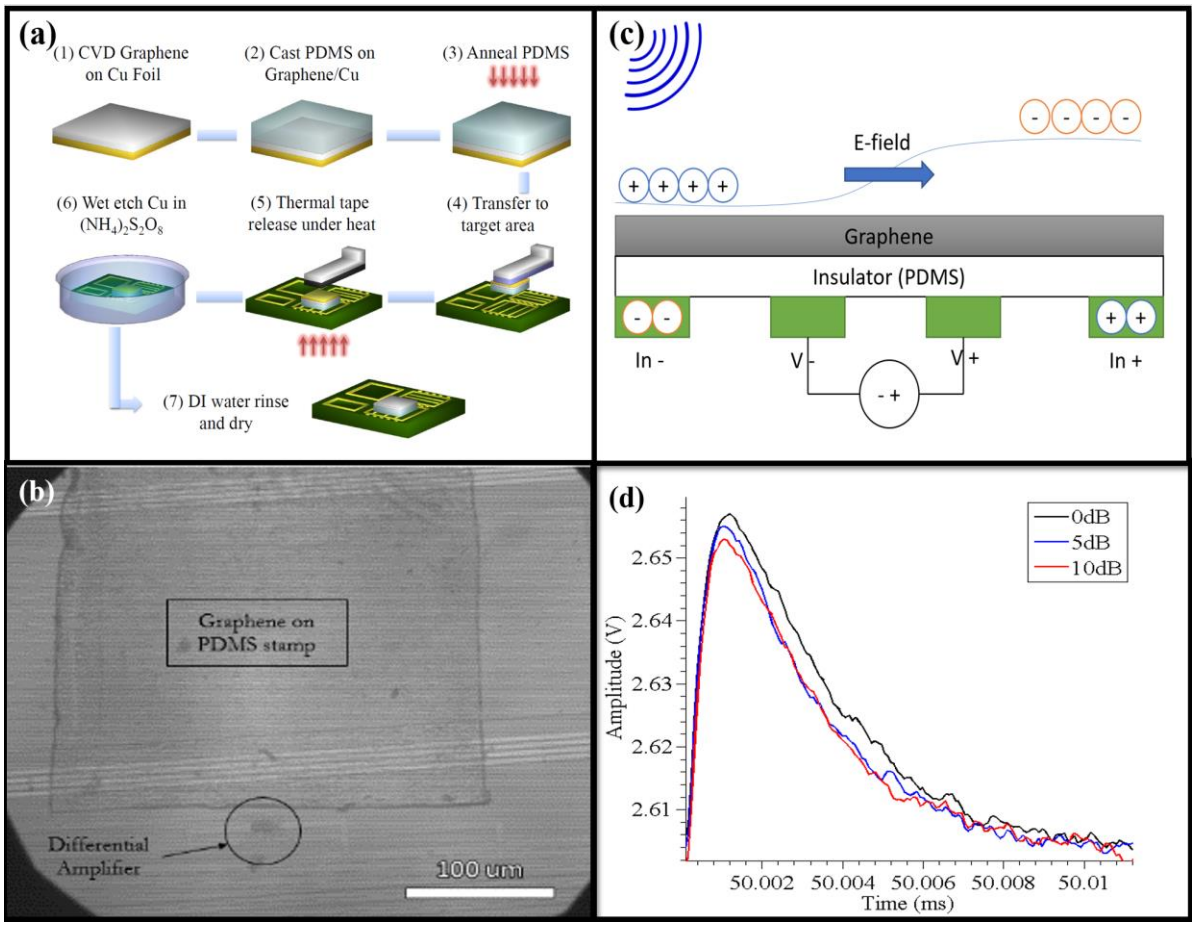

Fig. 4.2. (a) A novel graphene transfer process for complementary metal-oxide-semiconductor (CMOS) technology and (b) illustration of graphene after transfer. (c) Methodoology of graphene RF detector. Graphene was overlaid on CMOS architecture with the help of a dielectric separator. RF stimulus will effectively alter the graphene surface conductivity. With the utilization of an underlying electric-field, graphene charge will separate across the graphene surface and can be measured capacitively utilizing rails connected to a CMOS differential amplifier.

Despite the redirection of graphene research to implement RF detectors, the unique electrical and mechanical properties of graphene can still provide numerous advantages that benefit FETs. The most applicable quality is the controllable conductivity of graphene that is tunable based on a strong electric field-effect [5]. The ability to tune the conductivity within the same device leads to ambipolar transfer characteristics that enable a single GFET element to operate with both n-channel and p-channel characteristics. This feature has the potential to solve the current

geometrical limitations of CMOS architecture as both nMOS and pMOS devices cannot occupy the same physical area. Additionally**,** in a sensor application the high carrier mobility of graphene can boost electronic response time. Recently, IBM researchers have demonstrated an epitaxial GFET with A 240nm channel length that exhibited a cutoff frequency of 100 GHZ which greatly outperforms any silicon-based MOSFET architecture of similar geometry. The functionalization of graphene to a RF, biological, or photonic source will also enable graphene to act as a high-speed detection device.

4.2.1 A novel flexible graphene transistor architecture

The following section demonstrates the proposed architecture and feasibility of a three-terminal graphene transistor architecture utilizing liquid-metal electrodes and is given the name liquid-metal graphene field-effect transistor, *LM-GFET*. In a typical GFET fabrication process, graphene is typically synthesized via chemical vapor deposition and transferred to a target surface via delamination. Lift-off processes are then used to construct contact electrodes, gate-dielectrics, and gate-contacts [6] [7] [8]. Unfortunately, numerous articles have reported degradation in graphene transistor performance due to mechanical and electrical strain put on graphene that is a direct result of photolithography and physical vapor deposition based techniques used [9] [10] [11] [12]. In addition, graphene has been shown to exhibit high contact resistance with standard electrode materials relative to its size that create non-ideal performance across the board [12]. This performance limitation will potentially force a researcher back into the cleanroom to identify drawbacks in his or her fabrication process.

As described in Chapter 3, the integration of conformal liquid-metal electrodes allows low-resistance repeatable electrical contact to be made with graphene, without the typical damage and chemical doping graphene would encounter with standard PVD processes.

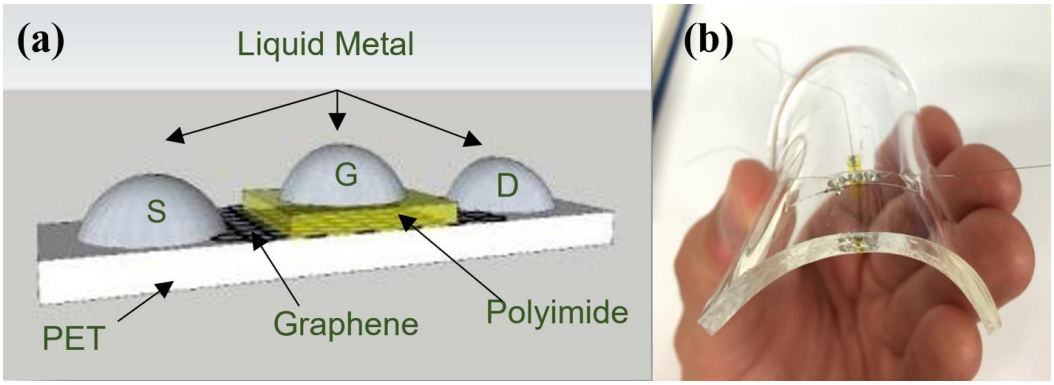

Fig. 4.3. (a) Visualization of flexible three-terminal device with graphene and liquid-metal electrodes, *LM-GFET*. The location of the gate dielectric separator is in yellow (b) Device encapsulated in an elastomer

To fabricate the proposed flexible *LM-GFET*, chemically vapor deposited graphene (CVD graphene) was first commercially transferred to a Polyethylene terephthalate (PET) substrate to serve as support substrate for graphene. PET was chosen due to its moderate bendability and manageable thickness that made it easy to cut the samples to a desirable size with standard cutting tools. Graphene quality on PET was determined with a Renishaw 514nm Confocal Raman Spectroscopy system as discussed in Chapter 1. When a region of high quality graphene was identified, A Kapton film (polyimide film) with a thickness of 12.5 micron and dielectric constant of four was then cut to a desirable size and overlaid onto the graphene/PET sample to act as a dielectric separator. A back-gate configuration can also be used, however, suffers from large parasitic capacitances and cannot be integrated with other components easily [3].

Utilization of a blunt-tip syringe needle (1 ml BD Syringe), allowed three liquid metals droplets to be dispensed on the monolayer graphene surface, two of which made direct contact with graphene to act as a source and drain electrode, and a third electrode was dispensed on the Kapton film to act as a top-gate electrode. In a final step the device was encapsulated in

Polydimethysiloxane (PDMS, Sylgard Elastomer 184) to counteract the rapid surface oxidation of liquid-metal with oxygen as discussed in Chapter 3. A visualization of the transistor architecture is illustrated Fig. 4.3 alongside an image of the device encapsulated in PDMS.

4.2.2 Transfer Characteristics of LM-GFET with polyimide dielectric separator

To determine the operational performance of LM-GFET devices with a polyimide dielectric separator, the following graphene transfer characteristics were obtained and a model was used to extract the relevant parameters for n_0 and μ for both the hole and electron branches.:

- drain current as a function of the gate-source voltage ($I_D - V_{gs}$)
- channel resistance as a function of gate-source voltage ($R_D - V_{gs}$)
- drain current as a function of the drain voltage ($I_D - V_D$)

All measurements were conducted with a Keysight B1500A Semiconductor Probe Analyzer and electrical contact was made with a Micromanipulator probe station integrated with tungsten probe tips. Tungsten was used due to its chemical inertness and stability in contact with Galinstan. To reduce noise, all measurements were made in vibration-isolated faraday environment. Fig. 4.4, illustrates the experimental setup and test electrical connections.

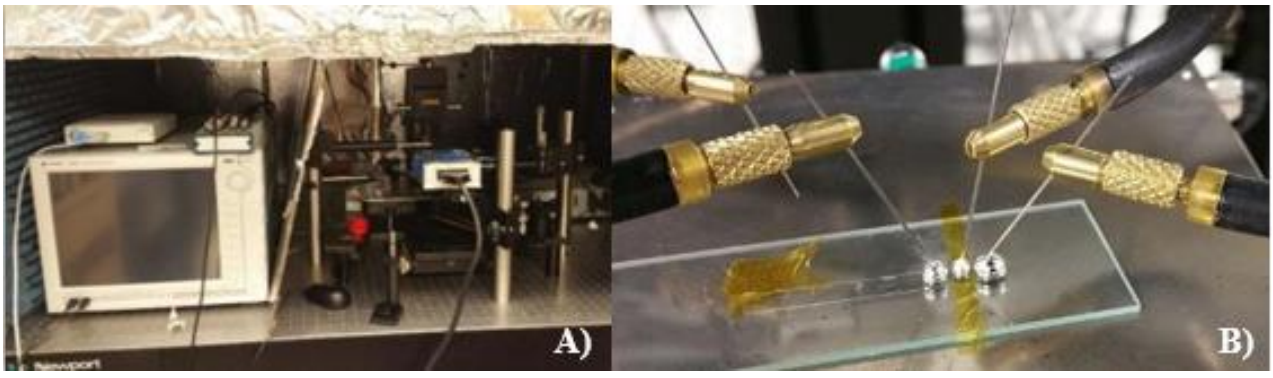

Fig. 4.4. (a) Experimental Set-up for device characterization and (b) flexible GFET with liquid metal electrodes probed by tungsten probe tips. To ensure ohmic contact with the measurements probes, the tungsten probes were penetrated through the Galinstan droplet surface.

The drain current (top) and channel resistance (bottom) as a function of top-gate voltage V_{TG} are both shown in Fig. 4.5. The point at which both the hole and electron conduction branches meet is known as the charge neutrality point (Dirac point) [13]. Fig. 4.5 illustrates the charge neutrality point occurs at the V_{TG} = 0 and represents the gate-voltage for which the maximum resistivity occurs in the graphene channel.

Careful analysis of the conduction branches featured in the current-voltage characteristics illustrate the ambipolar characteristics of graphene as discussed in Chapter 2 and will aid in the determination of the carrier density and type of carrier (either electrons or holes) that exist in the graphene channel. It was noted that for negative values of V_{TG}, the graphene channel promotes hole conduction (left branch) and for positive values of V_{TG}, the graphene channel promotes electron conduction (right branch). This characteristic is unique to graphene and is described in [5] as a direct relationship between the fermi energy and variable carrier concentration $E_F = \hbar v_F \sqrt{\pi n}$, hence, altering the density of states that depends linearly on electrostatic potential. The ability to tune the conductivity of graphene with a gate-source voltage is of great value to the semiconductor industry as the same device can operate with both n-channel and p-channel characteristics.

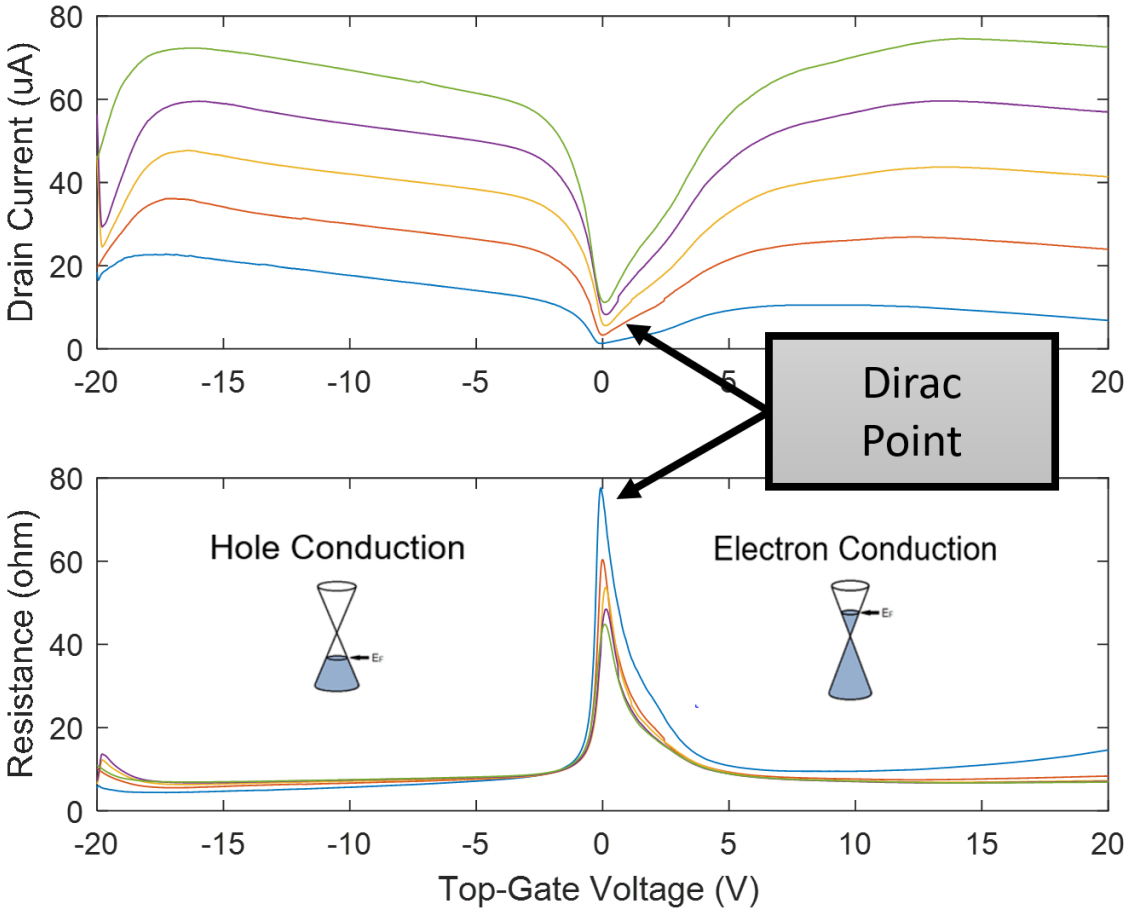

Fig. 4.5. Drain Current I_d and channel resistance R_d as a function of the gate to source voltage. It is important to note the charge neutrality point occurs at the dirac voltage (minimum conductivity). A shift from V_{TG} = 0 represents chemisorption due to chemical doping within the transistor architecture.

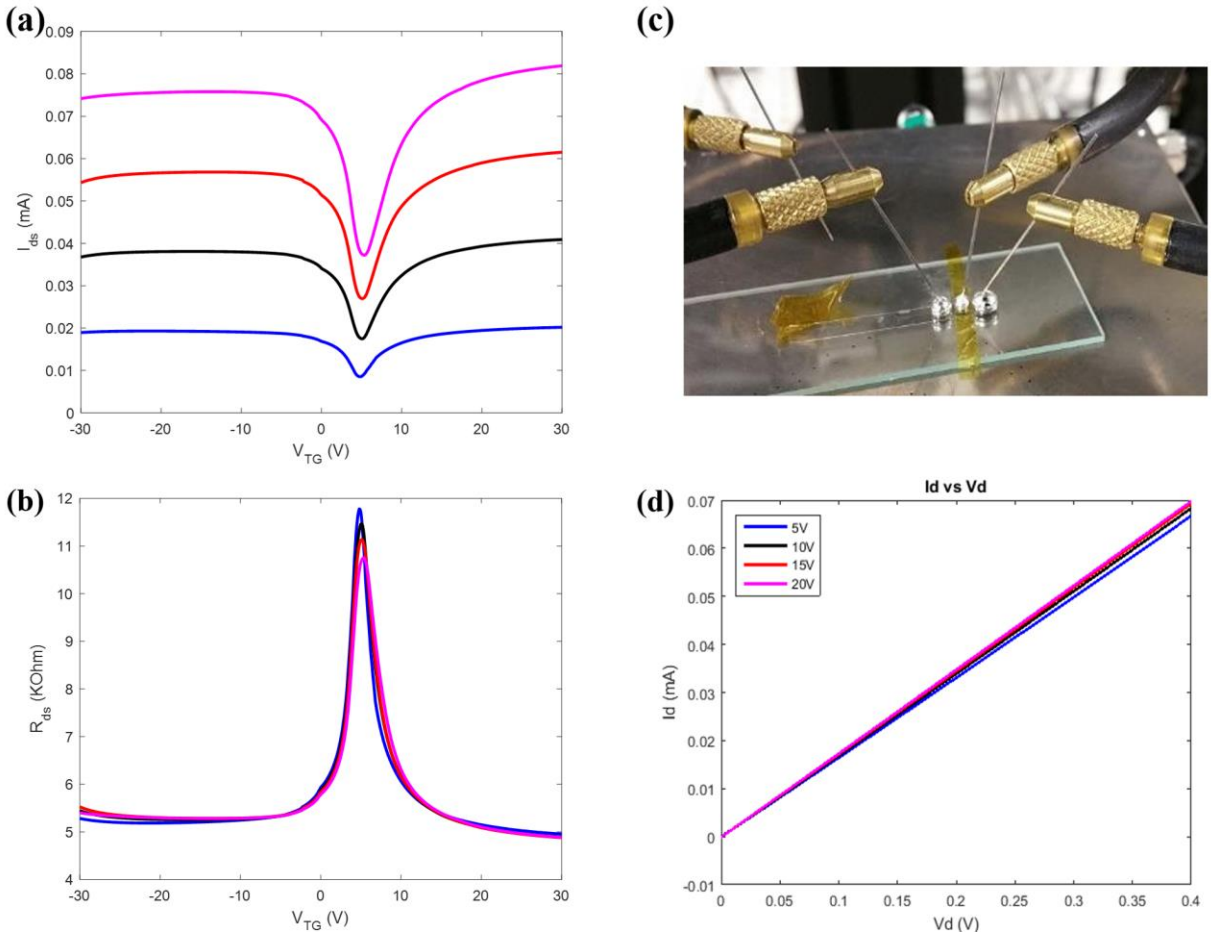

Fig 4.6. (a) Drain Current I_d as a function of top-gate voltage V_{TG} for LM-GFET with polyimide top-gate and (b) Drain Resistance R_d as a function of top-gate voltage V_{TG}. (c) Image of device-under-test. (d) Drain Current I_d as a function of drain voltage V_{TG}.

Due to the chemical nature of graphene, the charge neutrality point can be shifted from V_{TG} = 0 by chemically induced doping that may be a result of the fabrication processes or work function mismatch amongst the materials that comprise the transistor architecture. The ambipolar transfer characteristics for an LM-GFET with a shifted dirac point is shown Fig. 4.6. The location of the dirac point was determined to be at $V_{TG} = 4.5V$, therefore, states there is moderate chemical p-doping and may be due to the materials involved in fabrication [14]. It was determined that moderate chemical doping occurred due to the sodium hydroxide solution used to deter chemical oxidation of the Galinstan droplets. As the Galinstan electrodes were dropped on the dielectric

surface sodium hydroxide would either etch the polyimide film slightly or overflow onto the graphene surface. However, the doping remained small <5V and was considered reasonable compared to the literature [3]. The dirac point can be corrected if a back-gate voltage is applied via a back-gate transistor architecture. However, a back-gate GFET embodiment suffers from parasitic capacitance, therefore, the intrinsic dirac point is located at higher gate-voltages and higher gate-voltages are needed to swing dirac-voltage back to zero. Lastly, Fig 4.6 illustrates the drain current as a function of drain voltage and demonstrates correct transistor operation in that the as the drain voltage is increased the graphene channel conductivity is increased. However, it was also determined the device did not reach saturation within the measured drain voltage range.

4.2.3 Modeling Transistor Behavior

To validate the *LM-GFET* transfer characteristics curve fitting was made with the model described in *Kim et al.* [13] and compared with a measure of the total resistance R_{tot} . The model consists of an approximated graphene channel carrier concentration (electron or holes):

$$n_{tot} = \sqrt{n_0^2 + n[V_{TG}^*]^2}$$

where n_0 represents the carrier density at the charge neutrality point. $n[V_{TG}^*] = V_{TG} - V_{dirac}$, is the gate dependent carrier concentration away for the charge neutrality point and is obtained from the quantum capacitance of graphene and the gate-source voltage:

$$V_{TG} - V_{dirac} = \frac{q}{C_{ox}} n + \frac{\hbar\, v_F \sqrt{\pi n}}{q}$$

The total resistance is than approximated as:

$$R_{tot} = R_{contact} + R_{channel} = R_{contact} + \frac{N_{sq}}{n_{tot} q\mu} = R_{contact} + \frac{N_{sq}}{\sqrt{n_0^2 + n[V_{TG}^*]^2} q\mu}$$

where N_{sq} is the W/L (width/length) ratio of the graphene channel. With a non-linear regression written in MATLAB, the model data for R_{tot} was fitted to the real data as shown in Fig. 4.7. The relevant parameters were than extracted for n_0 and μ for both the hole and electron branches.

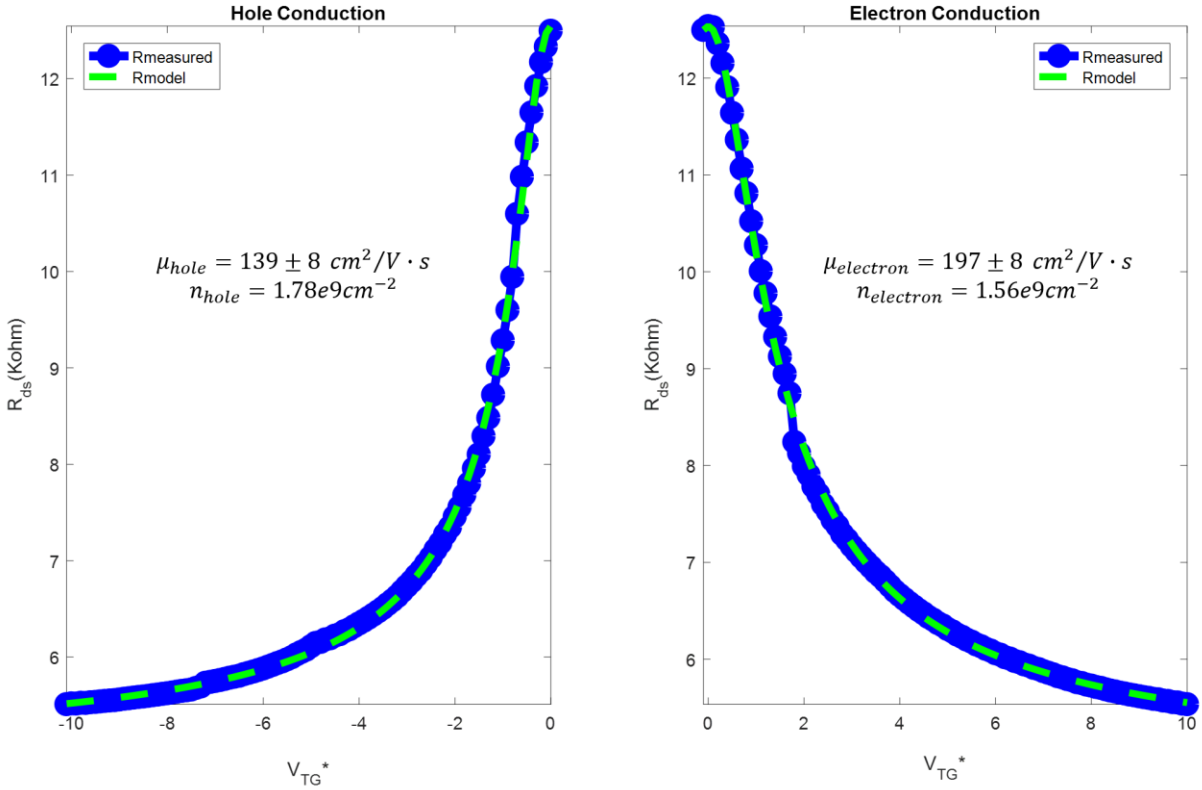

Fig 4.7. Drain-to-source resistance as a function of V_{TG}^* for a LM-GFET device with polyimide gate dielectric for the data illustrated in Fig 4.6 in which $V_d = 200\ mV$. Measured data (blue) along with modeling results (green). The inset illustrates the hole and electron mobilities and carrier concentrations.

By fitting the model to the measured data from Fig 4.6, the relevant parameters were extracted and summarized in Fig.7. The modeled data is in good agreement with the measured data. The results are promising as they are comparable with traditional GFET operation [15, 16, 17, 18]. Despite obtaining reasonable results, $\mu_{hole} = 139 \pm 8\, cm^2/V \cdot s$ and $\mu_{electron} = 197 \pm 9\, cm^2/V \cdot s$ is quite low compared to [19] and is believed to be due to a fairly large physical channel length that will result in a large number of defects over the length of the graphene channel, therefore, the

mobility will go down. The channel length used in the measured devices was on the order of hundreds of microns.

4.2.4 The use of electrolytic gate dielectrics in graphene transistors

It is important to note the use of polyimide dielectric separator produced undesirable results due to the inability for the gate-capacitance to remain constant over time and over multiple devices. It was determined that the sodium hydroxide used to deter the rapid surface oxidation of liquid-metal during transport would also etch the polyimide dielectric separator providing unreliable results in the current-voltage measurements. This can be seen by a measure of capacitance over time for sodium hydroxide on a polyimide film, Fig. 4.8.

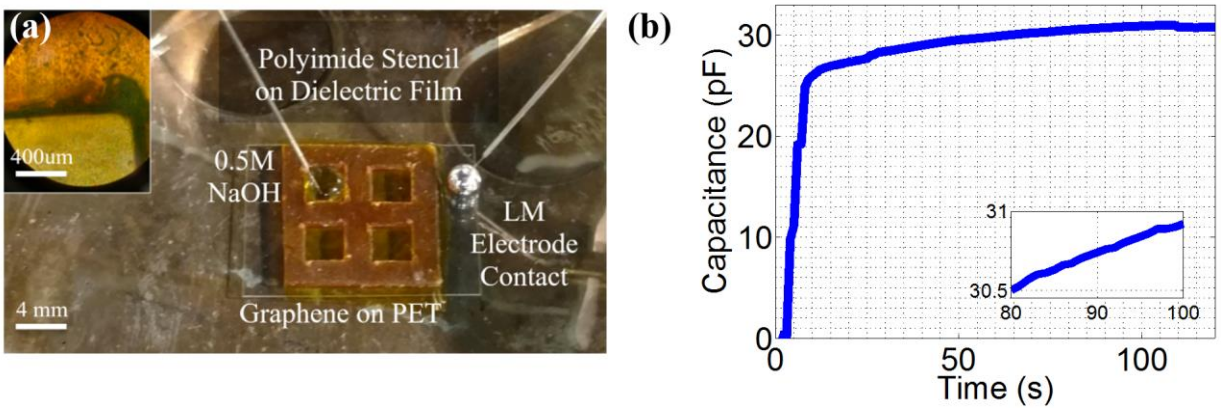

Fig. 4.8. (a) Flexible graphene capacitor with graphene on PET covered with a polyimide film and a polyimide stencil used to hold the sodium hydroxide in place. (b) Change in capacitance as a function of time. It was seen that the capacitance exponentially increases until a saturation point.

To mitigate this effect, use of an electrolytic gate dielectric (EGD) was explored rather than a solid dielectric material as was done with the polyimide film. Recently, ion gels have demonstrated ideal performance as EGDs for flexible GFET devices due to an ability to produce extremely high gate-capacitance and high dielectric constants required for high on-current and low-voltage operation

[15]. In addition, the biasing voltages required for EGD based transistors are much smaller on the order of <1V.

An EGD is fundamentally different than a solid gate dielectric material in that the EGDs are liquids with various viscosity and ionic concentrations. Due to the presence of ions and high polarizability of EGDs, a diffusion of charge is formed at the thin layer between the EGD and conducting materials like graphene. This layer forms an electric double layer and is typical when ionic liquids contact metallic surfaces [20]. Due to the nanoscale separation distance of the electric double layer, usually from 1-10nm, a large charge gradient is formed on the conductive surface. For example, in the case a gate electrode is positively charged and submerged in an EGD on graphene, anions will accumulate at the gate/EGD interface and cations will accumulate at the EGD/graphene interface. The resultant electrical double layer at the EGD/graphene interface will then alter the conductivity of the conducting material, Fig 4.9. The opposite is true for the case in which the gate electrode is negatively charged.

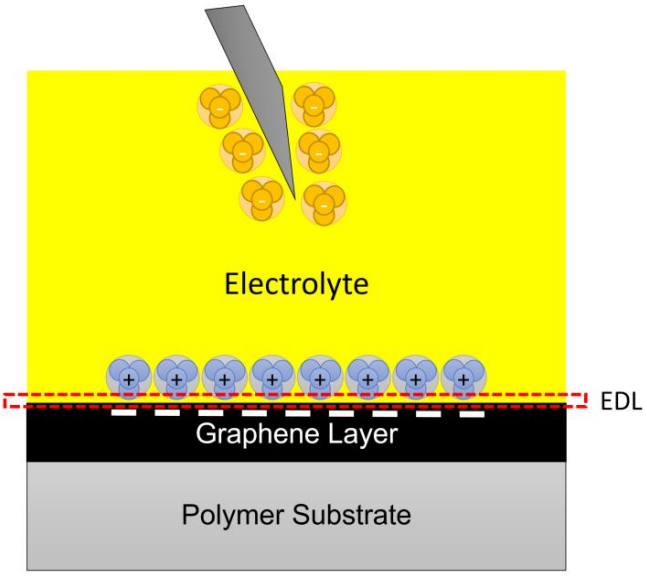

Fig. 4.9. Representation of charge distribution between electrolyte and graphene surface. The activation of a gate electrode constructs a charge gradient in an electrolyte that generates an electric double layer above a graphene surface that alters the graphene conductivity.

The fabrication of gel-like EGD materials, known as ionic gels, is quite challenging. Typically, a triblock copolymer is mixed in a toxic ionic liquid and dissolved in a solvent [15, 16] for many days. Unfortunately, ionic gels require special preparation in an atmospherically controlled environment to mitigate outgassing and combustion, which only adds to its complexity. There is a need to find alternate EGD materials that are non-toxic, have easy preparation, and are readily available.

4.2.5 Transfer characteristics of LM-GFET with gate dielectric made of honey

Honey is typically produced via sugary secretions from bees, harvested, and packaged under various brand names for commercial food consumption. Honey contains various concentrations of water, vitamins, minerals, amino acids, and sugars: fructose, glucose, sucrose that can be controlled via bee production and honey extraction techniques [21]. To our benefit, the water and acidic content of honey formulate an ionic gel-like solution analogous to ion gels. The introduction of honey as an electrolytic gate dielectric is advantageous for the rapid fabrication of GFET devices due to honey's commercial availability, non-toxicity, control of ionic content that can be used to alter dielectric properties, and minimal preparation time. The transistor architecture of the *LM-GFET* device with an electrolytic gate dielectric comprised of Honey is shown in Fig. 4.10a and an image of the device are shown in Fig 4.10(c). Graphene was commercially purchased and a measure of the graphene quality was conducted with a Renishaw InVia 514.5nm (Green) Micro-Raman Spectroscopy System for three different graphene sites. The absence of a defect band *D* and analysis of the peak intensity ratio of the *2D* and *G* Bands $(I_{2D}/I_G \approx 2)$ indicated high-quality graphene in all three sites, Fig 10(b). A strip of graphene on Polyethylene Terephthalate (PET) was then cut with standard cutting tools and adhered onto a glass microscope slide with the graphene facing up. Liquid-metal Galinstan droplets with a volume $0.6mm^3$ were dispensed with

a blunt-tip syringe to act as electrodes. Care was taken to withdraw liquid-metal Galinstan from its original container as to minimize exposure to atmospheric oxygen. Therefore, the rapid surface oxidation of Galinstan can be minimized. In the event liquid-metal Galinstan was to oxidize, the surface tension of the liquid-metal droplet will lower and actively wet to surrounding surfaces, analogous to a paste. A researcher may utilize a solution of 0.1M NaOH (Sodium Hydroxide) and deionized water to preclude the rapid surface oxidation. Raw Honey was commercially acquired via Amazon.com and dispensed from a plastic dropper at a volume of $1.0mm^3$ between the two liquid-metal droplets to act as the electrolytic gate dielectric. Contact was made with the source, drain, and gate electrodes using standard s a semiconductor probe station.

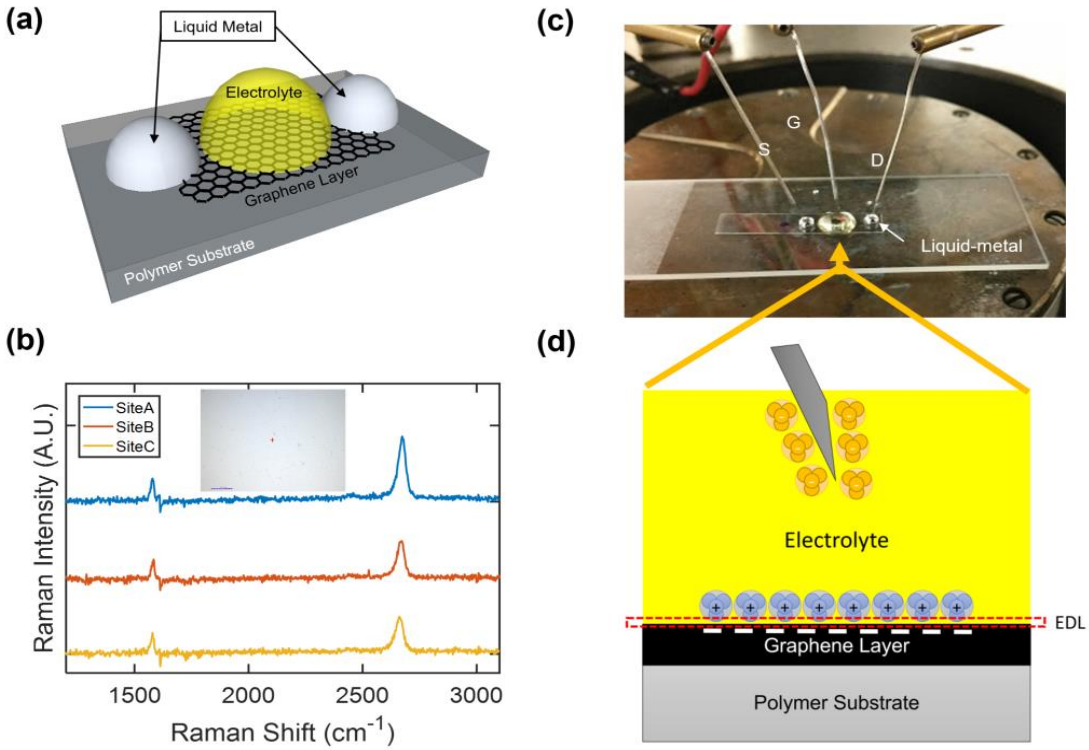

Figure 4.10. (a) Illustrations of graphene field-effect transistor with liquid-metal source and drain electrodes (LM-GFET); and electrolytic gate dielectric comprised of honey. (b) Raman spectroscopy profile of graphene sample transferred to Polyethylene Terephthalate. (c) Image of the LM-GFET and (d) representation of charge distribution in the honey-gate dielectric.

Electrical measurements were performed with an Agilent 4155C Semiconductor Parameter Analyzer in air and in a standard laboratory environment. To determine the operational performance of the device with the Honey gate dielectric, the following graphene transfer characteristics were obtained:

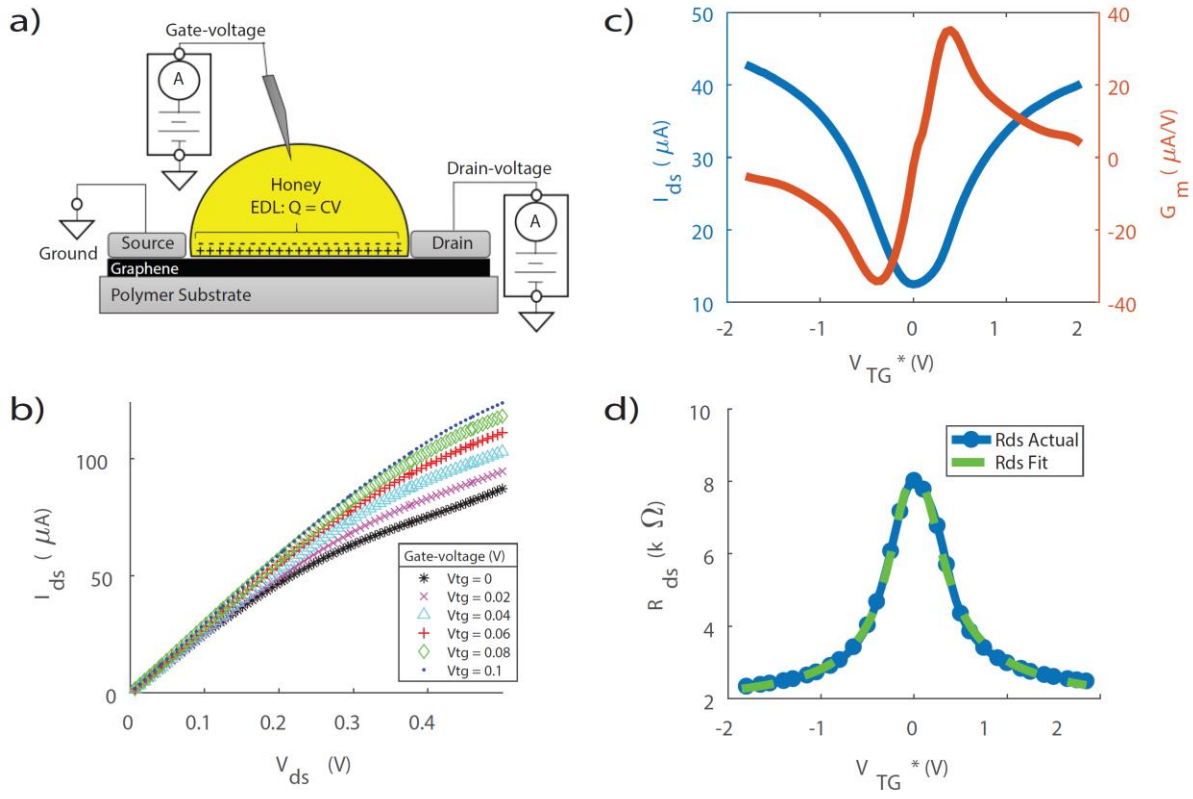

Fig. 4.10. (a) Schematic representation of single-gate *LM-GFET* electrolytic gate dielectric made of honey and location of the electric double layer. (b) *Left:* Relationship of drain-to-source current as a function of top-gate voltage ($I_{ds} - V_{TG}^{*}$) and *Right:* Transconductance, G_m, as a function of top-gate voltage ($G_m - V_{TG}^{*}$). (c) Measured data and fitting model for the drain-to-source resistance as a function of top-gate voltage ($R_{ds} - V_{TG}^{*}$) (d) Drain-to-source current as a function of drain-to-source voltage for varied top-gate voltage ($I_{ds} - V_{ds}$).

- drain current as a function of the gate-source voltage ($I_D - V_{gs}$)
- channel resistance as a function of gate-source voltage ($R_D - V_{gs}$)
- drain current as a function of the drain voltage ($I_D - V_D$)

- the transconductacnce (g_m)

A schematic representation of the electrical measurements is shown in Fig. 4.11(a). Fig. 4.11(b-d) illustrate graphene transport characteristics for a single-gated *LM-GFET* device with an electrolytic gate dielectric made of honey.

The V-shaped curve of the relationship between top-gate voltage V_{TG}^{*} and drain-to-source current I_{ds} in Fig. 4.11(c) highlights the ambipolar operation that is characteristic of any graphene field-effect transistor and provides designers the flexibility to bias the device in either hole or electron conduction mode. A well-documented model extraction technique was utilized to extract graphene parameters from the device's transfer curve [13]. The model fits determined hole and electron mobilities of 213 ± 15 and $166 \pm 5\ cm^2/V \cdot s$ respectively, at a drain bias of 100 mV. Despite the rapid and inexpensive fabrication process, the devices exhibited performance comparable to that of much more elaborately fabricated GFET devices with ionic gels [15, 18]. In addition, Fig. 4.11(c) also illustrates the device's transconductance that reaches a considerable value of $38uA/V$ with a large degree of symmetry and linearity within the operational range of *-0.5V* to *0.5V*. This linear, ambipolar transconductance has significant utility in ambipolar electronic circuits such as radio frequency mixers, digital modulators, and phase detectors [22]. Fig. 4.11(b) illustrates the $I_{ds} - V_{ds}$ response to the various transconductances associated with different V_{TG}^{*} values. Fortunately, due to the monotonic transconductance of the *LM-GFET* devices, the drain-to-source voltage V_{ds} sweep does not demonstrate an inflection point. Particularly, the varying V_{TG}^{*} curves do not intersect one another, which cannot be presumed to occur in all standard GFET devices [3]. Instead, the $I_{ds} - V_{ds}$ trend is encouraging because the drain currents diverge at higher V_{ds} biases. As a sensor based on GFET architecture, a designer can first bias his/her device at the desired V_{ds} and I_{ds}. Then, external stimuli will trigger a change in the device's gate voltage, which will create

a notable change in I_{ds}. Note, the dielectric constant of honey was measured to be 21 and the gate capacitance was measured to be $4.7 uF/cm^2$ using an LCR meter which is very comparable to what is described in the literature [23] [24].

4.3. Discussion

The *LM-GFET* devices described in Chapter 4 have demonstrated a way to rapidly characterize graphene materials with the use of non-toxic eutectic liquid-metal Galinstan interconnects and flexible gate dielectrics. Due to the inconsistency of a three-terminal graphene field-effect transistor embodiment with use of a polyimide dielectric material, an electrolytic gate dielectric made of honey was explored. It is important to note that the *LM-GFET* with Honey produced repeatable results and the devices characterized in this section were fabricated within less than 30 minutes and in a general laboratory setting. Despite not being fabricated in a

Reference	Description	Electron Mobility	Hole Mobility	Flexibility
[17]	FET with pentacence and Au electrodes	$0.02\ cm^2/V \cdot s$		yes
[25]	Single-walled Carbon Nanotube with Graphene electrodes	$0.5\ cm^2/V \cdot s$	$2\ cm^2/V \cdot s$	yes
[26]	Ion gel GFET on PET	$91 \pm 50\ cm^2/V \cdot s$	$203 \pm 57\ cm^2/V \cdot s$	yes
	LM-GFET with Polyimide	$\mathbf{197 \pm 9\ cm^2/V \cdot s}$	$\mathbf{139 \pm 8\ cm^2/V \cdot s}$	**yes**
[27]	GFET with Ion Gel and Conductive Polymer Top-gate	$214\ cm^2/V \cdot s$	$106\ cm^2/V \cdot s$	yes
	LM-GFET with Honey	$\mathbf{166 \pm 5\ cm^2/V \cdot s}$	$\mathbf{213 \pm 15\ cm^2/V \cdot s}$	**yes**
[28]	Multi-FinFet	$300\ cm^2/V \cdot s$		no
[29]	UV cured Ion gel GFET	$452 \pm 98\ cm^2/V \cdot s$	$852 \pm 124\ cm^2/V \cdot s$	yes
[30]	IBM 100Ghz GFET on SiC	$1500\ cm^2/V \cdot s$	$1000\ cm^2/V \cdot s$	no

Table 4.1 Flexible Transistor Comparison

conventional cleanroom, the device embodiments provided comparable performance to the current state-of-the-art with an added flexibility component. A table comparing the electron and hole mobilities of the current state-of-art to the *LM-GFET* devices is shown in Table 4.1.

The manipulation of the physical characteristics of Galinstan is also a precursor to flexible devices. Liquid-metal Galinstan can be embedded in microfluidic enclosures and exhibit shape deformability. There are many devices that can result from reconfigurability such as wearable diagnostics and conformal RF devices. Moreover, the liquid state of honey provides the potential for uniform gate dielectrics that are currently an issue for PVD-based gate dielectrics. The author encourages the reader to explore alternate embodiments utilizing the liquid materials described and further explore the potential for flexible applications. The author admits the use of liquid-metal Galinstan and honey for graphene devices was discovered by accident. However, the author predicts such transistors will open the box on the exploration of alternative materials that are slightly unconventional in the hopes these innovative discoveries provide a new class of materials that are non-toxic, biodegradable, and require minimal preparation time.

REFERENCES

[1] G. Paolo and et al., "International Technology Roadmap for Semiconductors 2.0: Executive Report (ITRS)," Semiconductor Industry Association, 2015.

[2] J. H. Warner and et al., Graphene: Fundamentals and emergent applications, Newnes, 2012.

[3] F. Schwierz, "Graphene Transistors," *Nature nanotechnology*, vol. 5, no. 7, pp. 487-496, 2010.

[4] R. C. Ordonez and et al., "Radio Frequency Detection with On-chip Graphene," *Naval Engineers Journal*, vol. 126, no. 4, pp. 155-158, 2014.

[5] K. Novoselov, "Electric field effect in atomically thin cabon films," *Science*, vol. 306, no. 5696, pp. 666-669, 2004.

[6] L. Liao and et al., "High-speed graphene transistors with self-aligned nanowire gate," *Nature*, vol. 467, no. 7313, pp. 302-308, 2010.

[7] Y. Lin and et al., "100-GHz transistors from wafer-scale epitaxial graphene," *Science*, vol. 327, no. 5966, p. 662, 2010.

[8] C. M. Torres and et al., "High-Current Gain Two-Dimensional MoS2-Base Hot-Electron Transistors," *Nano Letters*, vol. 15, no. 12, pp. 7905-7912, 2015.

[9] L. Liao and et al., "Graphene dielectric integration for graphene transistors," *Material Science and Engineering: R: Reports*, vol. 70, no. 3, pp. 354-370, 2010.

[10] F. a. e. a. Michalik, "Investigation of the indluence on graphene by using electron-beam and photolithography.," *Solid State Communications*, vol. 151, no. 21, pp. 1574-1578, 2011.

[11] P. Toth and et al., "Electrochemistry in a drop: a study of the electrochemical behavior of mechanically exfoliated graphene on photoresist coated silicon substrate," *Chemical Science*, vol. 5, no. 2, pp. 582-589, 2014.

[12] W. Liu and et al., "A study on graphene—metal contact," *Crystals*, vol. 3, no. 1, pp. 257-274, 2013.

[13] S. kim and et al., "Realization of a high mobility dual-gated graphene feild-effect transistor with Al203 dielectric," *Applied Physics Letters*, vol. 94, p. 062107, 2009.

[14] D. Farmer, "Chemical doping and electron-hole conduction asymmetry in graphene devices," *Nano Letters*, vol. 9, no. 1, pp. 388-392, 2008.

[15] S. Kim and et al., "High-performance flexible graphene field effect transistors with ion gel dielectrics," *Nano Letters*, vol. 10, no. 9, pp. 3464-3466, 2010.

[16] K. Lee and et al., "Stretchable graphene transistors with printed dielectrics and gate electrodes," *Nano Letters*, vol. 11, no. 11, pp. 4642-4646, 2017.

[17] W. H. Lee and et al., "Transparent flexible organic transistors based on monolayer graphene electrodes on plastic," *Advanced Materials*, vol. 23, no. 15, pp. 1752-1756, 2011.

[18] C. Yan and et al, "Graphene-based flexible and stretchable thin film transistors," *Nanoscale*, vol. 4, no. 16, pp. 4870-4882, 2012.

[19] Venugopal, "Effective mobility of single-layer graphene transistors as a function of channel dimensions," *Journal of Applied Physics*, vol. 109, no. 10, p. 104511, 2011.

[20] D. Wang and et al., "Electrolytic gated organic field-effect transistors for application in biosensors—A Review," *Electronics*, vol. 5, no. 1, 2016.

[21] O. Anjos and et al., "Aplication of FTIR-ATR spectroscopy to the quantification of sugar in honey," *Food Chemistry*, vol. 169, pp. 218-223, 2015.

[22] Z. Wang, "Graphene-based ambipolar electronics for radio frequency applications," *Chinese Science Bulletin*, vol. 57, no. 23, pp. 2956-2970, 2012.

[23] W. Guo and et al., "Sugar and water contents of honey with dielectric property sensing," *Journal of Food Engineering*, vol. 97, no. 2, pp. 275-281, 2010.

[24] J. Cho and et al., "Printable ion-gel gate dielectrics for low-voltage polymer thin-film transistors on plastic," *Nature Materials*, vol. 7, no. 11, pp. 900-906, 2008.

[25] S. Jang and et al., "Flexible, transparent single-walled carbon nanotube transistors with graphene electrodes," *Nanotechnology*, vol. 21, no. 42, p. 425201, 2010.

[26] B. Kim and et al., "High-Performance Flexible Graphene Field Effect Trasistors with Ion Gel Gate Dielectrics," *Nano Letters*, vol. 10, pp. 3464-3466, 2015.

[27] T. Kim and et al., "Large-scale graphene micropatterns via self-assembly-mediated process for flexible device application," *Nano letters*, vol. 12, no. 2, pp. 743-748, 2012.

[28] Y. Liu an et al., "Electron mobility in multi-FinFET with a (111) channel surface fabricated by orientation-dependent wet etching," *Microelectronic Engineering*, vol. 80, pp. 390-393, 2005.

[29] S.-K. Lee and et al., "Photo-patternable ion gel-gated graphene transistors and inverters on plastic," *Nanotechnology*, vol. 25, no. 1, p. 014002, 2013.

[30] Y. Lin and et al., "100 GHz transistors from wafer-scale epitaxial graphene," *Science*, vol. 327, no. 5966, p. 662, 2010.

[31] F. Koppens and et al., "Photodetectors based on graphene, other two dimensional materials and hybrid systems," *Nature nanotechnology*, vol. 9, no. 10, pp. 780-793, 2014.

[32] A. Grigorenko and et al., "Graphene Plasmonics," *Nature photonics*, vol. 6, no. 11, pp. 749-758, 2012.

[33] Z. Li and et al., "High-sensitive hybrid photodetectors based on CdSe quantum dots and graphene for detecting ATP bioluminescence on lab-on-chip devices," in *Biomedical Circuits and Systems Conference (BioCAS), IEEE*, 2015.

[34] C. Lu and et al., "High mobility flexible graphene field effect-transistors with self-healing gate dielectrics," *ACS Nano*, vol. 6, no. 5, pp. 4469-4474, 2012.

5. Towards LM-GFET Optical Sensors

As discussed in Section 2.5, the ability to dope graphene electrostatically has the potential to tune the spectral responsitivity of graphene by the Pauli blocking of interband transitions with energies less than twice the fermi energy. A typical doping concentration for graphene transistors is on the order of $10^{11} cm^{-2}$ and can be easily achieved with electrostatic gating and will maximize the optical response of graphene into the infrared range. In addition, if the doping concentration were to reach $> 10^{14} cm^{-2}$, which can only be achieved via chemical doping, graphene absorption can be screened down the visible range [1]. Despite this unique quality to tune the spectral responsitivity of graphene, there have been few attempts to present graphene photodetectors with optical performance that can outperform photodetectors that are fabricated with engineered band gaps while reducing the cost of fabrication. Table 5.1 illustrates the performance reached by current graphene photodetectors [2].

Table 1 | Performance parameters.

Reference	Description	Responsivity	Detector type	Bandwidth	Wavelength	IQE (%)	EQE (%)
18,19	Graphene–metal junction	6.1 mA W^{-1}	Photocurrent (PV/PTE)	>40 GHz	Visible, NIR	10	0.5
30,37,52	Graphene p–n junction	10 mA W^{-1}	Photocurrent (PTE)		Visible	35	2.5
20–22	Graphene coupled to waveguide	0.13 A W^{-1}	Photocurrent (PV/PTE)	>20 GHz	1.3–2.75 μm	10	10
90	Graphene–silicon heterojunction	0.435 A W^{-1}	Schottky photodiode	1 kHz	0.2–1 μm		65
31	Biased graphene at room temperature	0.2 mA W^{-1}	Bolometric		Visible, infrared		
94	Dual-gated bilayer-graphene at low temperature	10^5 V W^{-1}	Bolometric	>1 GHz	10 μm		
105	Hybrid graphene–QD	10^8 A W^{-1}	Phototransistor	100 Hz	0.3–2 μm	50	25
63	Graphene with THz antenna	1.2 V W^{-1}	Overdamped plasma waves		1,000 μm		
120	Graphene interdigitated THz antenna	5 nA W^{-1}	Photovoltaic and photoinduced bolometric	20 GHz	2.5 THz		
147,148	Graphene–TMD–graphene heterostructure	0.1 A W^{-1}	Vertical photodiode		<650 nm		30
130	Biased MoS_2	880 A W^{-1}	Photoconductor	0.1 Hz	<700 nm		
143	Graphene double-layer heterostructure	>1 A W^{-1}	Phototransistor	1 Hz	0.5–3.2 μm		
7,8,134	WSe_2 p–n junction	16 mA W^{-1}	p–n photodiode		<750 nm	60	3
136	GaS nanosheet	19.1 A W^{-1}	Photoconductor	>10 Hz	0.25–0.5 μm		

Table 5.1 illustrates the performance reached by current graphene photodetectors [2]

As shown, there have been various successes with manipulation of graphene plasmonic and phononic effects to improve graphene optical response. For example, there has been success with a graphene p-n junction device ($10\ mA\ W^{-1}$), a hybrid graphene device ($10^8\ A\ W^{-1}$), and a bi-layer graphene photodetector ($10^5\ A\ W^{-1}$) [2]. However, the complexity to fabricate the devices overviewed in Table 5.1 have slowed adoption into the photodetector industry.

In the following sections, the author demonstrates the integration of the *LM-GFET* device into different photodetection mechanisms. The author begins by a demonstration of the broadband optical absorption of graphene in a two-terminal graphene device followed by the weak bolometric effect of graphene with 3-terminal transistor architecture on bulk silicon and silicon dioxide. The author then demonstrates the two-terminal embodiment with semiconductor quantum dots followed by a demonstration of a PN junction embodiment to increase detector gain. The author then wraps up Chapter 5 with a combination of semiconductor quantum dots and the PN junction embodiment that demonstrates responsivity of $1\ mA/W$.

5.1 Measurements of Graphene broadband absorption

As described in Chapter 2, graphene has a broad spectral bandwidth that spans the visible to infrared ranges with a 2.3% optical absorption coefficient. When a laser source irradiates graphene, a photocurrent can be generated that changes the overall conductivity. Connected to a measurement device, the photocurrent change can be measured. A demonstration of graphene photocurrent generation in a two-terminal configuration to a modulated red (785nm), green (532nm), and blue (405nm) laser source illustrated in Fig. 5.1. It was determined that the responsivity for each laser source was approximately $22.5\ uA/W$, $20\ uA/W$, and $28\ uA/W$ respectively when the laser was cycled on and then off. It is important to note the responsivity in Fig 5.1 is for unbiased graphene. Therefore, the density of states is at its minimum and there is

little charge to interact with the incident laser source. In this embodiment, the photocurrent response is weak. To increase sensitivity the graphene material can be biased in which the fermi energy level is altered under and applied gate bias as discussed in Chapter 2. The optical response of graphene can then become controllable with the electric field-effect and can be implemented with a graphene field-effect transistor architecture that can screen interband transitions with energy less than twice the fermi energy due to Pauli blocking.

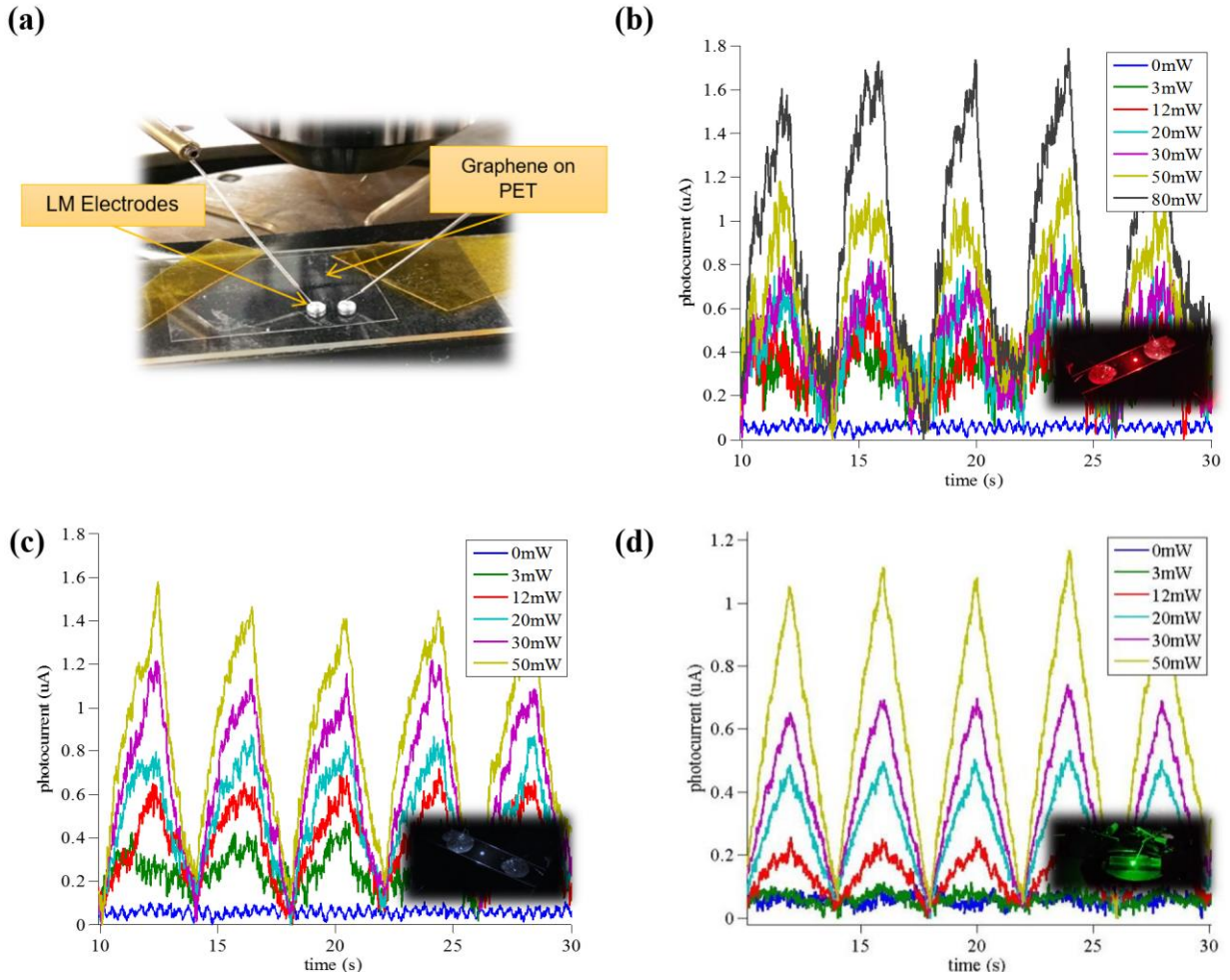

Fig. 5.1. (a) Illustration of graphene two-terminal device with liquid-metal electrodes. Room-temperature Graphene visible response to (a) 785 nm, (b) 405 nm, and (c) 532 nm laser light.

5.2 Bolometric effect in graphene optical response

In a graphene transistor embodiment, graphene has a channel resistance on the order of 1-2Kohm with an excess resistance that is dependent on the contact resistance. When electromagnetic energy such as in the form of a laser spot irradiates a graphene material, the laser has the potential to increase the temperature around the incident area [2, 3]. The temperature change, also known as the bolometric effect, alters the graphene resistance and has the potential to produce a change in DC current. This can be seen by the application of a 785nm laser spot on graphene transistor embodiment on a single crystal silicon wafer doped with n/phosphoric (resistivity $< 50\ ohm - cm$) and $100\ nm$ oxide thickness as shown in Fig. 5.2.

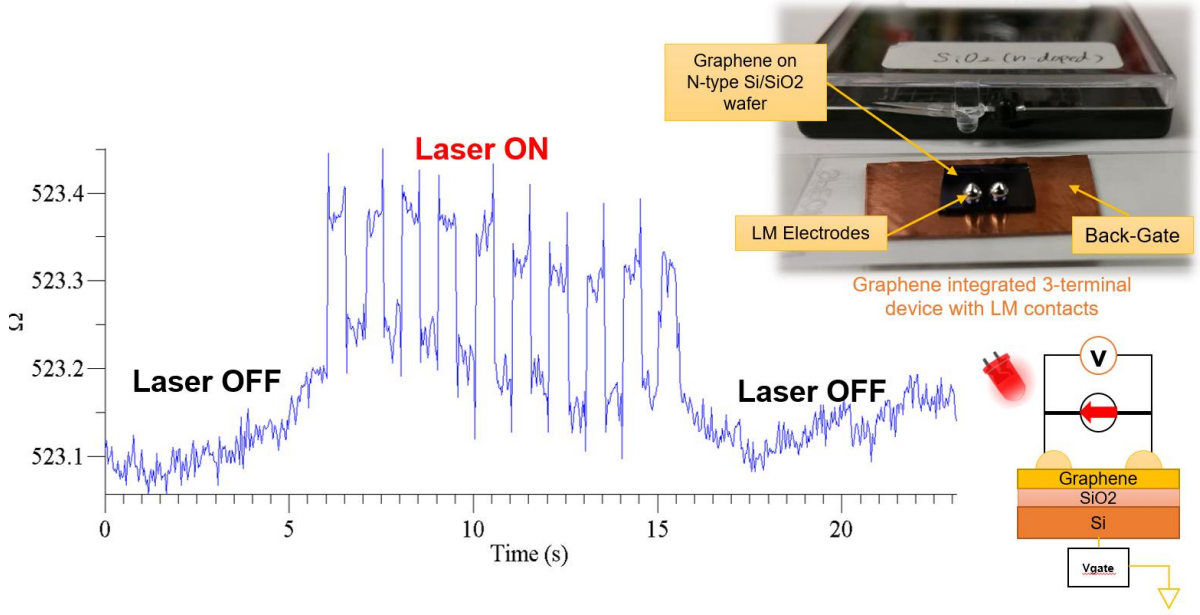

Fig. 5.2 Minute changes in graphene resistance due to IR laser excitation, $785\ nm$, $16\ mW$, $V_{back-gate} = 4V$

The resistance change can be described as the weak coupling between incident photons and graphene phonons (lattice vibrations). Typical embodiments of the bolometric effect are known as microbolometers and serve a variety of biological and military applications that span the mid-

infrared and terahertz wavelengths. However, there is weak temperature dependence on the electrical resistance in graphene that has only demonstrated small responsivity of $0.2\,mA/W$ [2]. Furthermore, bolometers suffer from long decay times on the order of many milliseconds, therefore, limits the use in high-speed optoelectronic applications.

5.3 Graphene with semiconductor quantum dots

To augment the difficulties in photodetector gain, semiconductor-based quantum dots, also known QDs, have been implemented into a graphene photodetectors [4, 5]. Like the new QLED televisions manufactured by Samsung, QDs can be arrayed to emit/absorb high resolution optical information while maintaining a high-energy star rating required by commercial markets. QDs are best defined as semiconductor Nano spheres where size (~1-10nm) and shape of a QD can be carefully manufactured to determine their photo emission/absorption properties. For example, QDs with a size of $\sim 2-3nm$ have visible light emission/absorption and QDs with a size $> 6\ nm$ has infrared light emission/absorption. Recently, quantum dot synthesis has become very cheap and architectures have been explored using materials such as graphene. Lastly, the QD stark effect can be exploited to electronically tune the QD photoemission over a narrow bandwidth and at much higher speeds. This enables access to wavelengths that are previously not accessible by state-of-art laser technology [6].

To demonstrate the potential for QDs into *LM-GFET* architectures, a quantum dot integrated device was explored and is illustrated in Fig. 5.4. The device consists of a graphene conductive channel on a flexible substrate. QDs were drop casted on graphene with a standard syringe needle, dried, and act as photon absorbers in the presence of a collimated laser source. Liquid-metal contacts form the source and drain electrodes and tungsten wires penetrated the liquid-metal

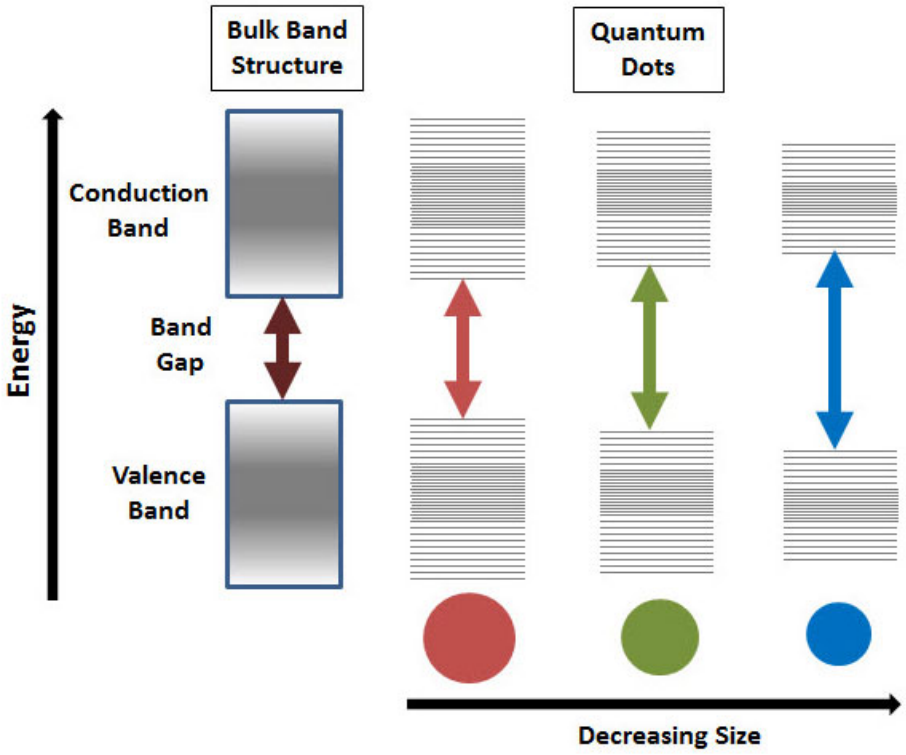

Fig. 5.3 Visualization of quantum dots as a function of band gap. The size and radius of the quantum determines the spectral emission and absorption properties [7].

electrodes to make electrical connections to test instruments. In a final step, the entire device was sealed with a silicon elastomer to hold the liquid-metal droplets in place.

The integration of quantum dots on a two-terminal liquid-metal device was measured and recorded to have a resistance change of $\sim 1K\Omega$ in the presence of a $5mW$ UV ($365\ nm$) light source. The change in resistance can be attributed to a photo gating effect in the presence of excited QDs. As the quantum dots are irradiated with collimated UV light source, photon absorption has the potential to generate an excess of electron hole pairs in the quantum dot layer. This charge separation generates an internal electric field that has the potential to aloter graphene conductivity due to the work function mismatch between graphene and the quantum dot layer [5].

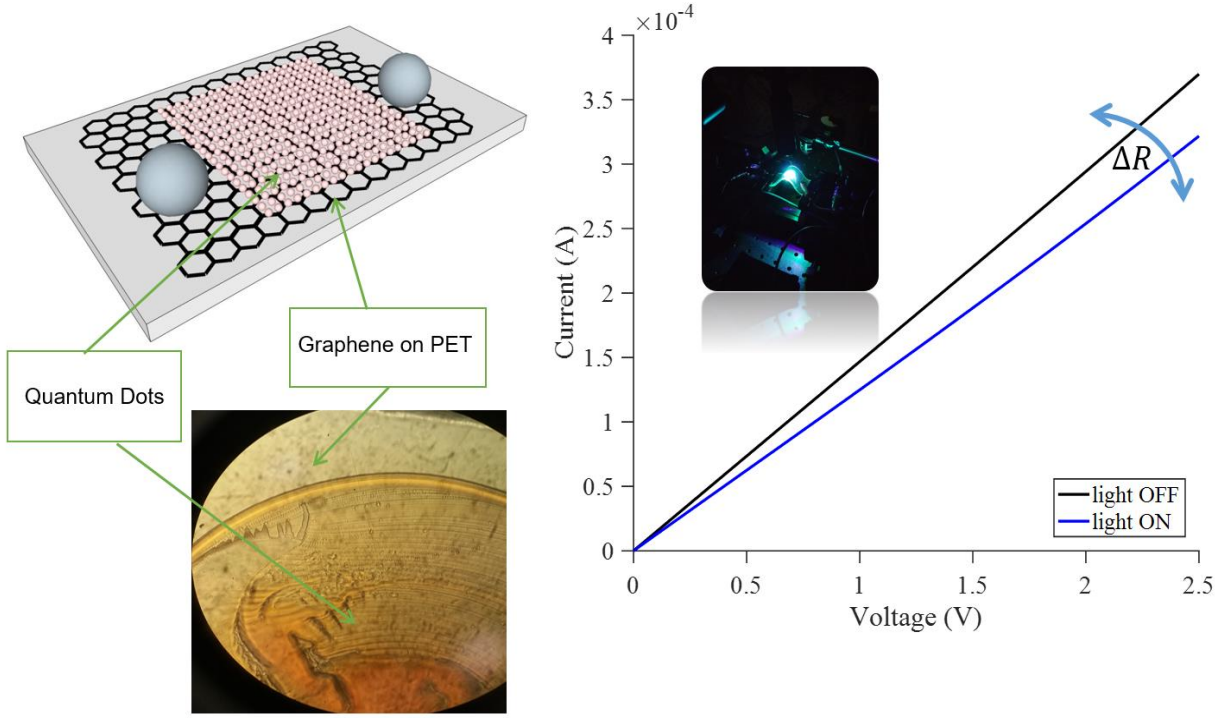

Fig. 5.4. Current-Voltage characteristics of a two-terminal graphene device with galinstan electrodes. The activation of quantum dots with a photoemission of 487nm using a UV (365nm) laser source alters the graphene resistivity.

Depending on the intrinsic carrier concentration of graphene at the time of illumination, the resistance will either increase or decrease. In the measured case, Fig 5.4, the resistance increased and may be contributed to current quenching caused by recombination taking place between the photo generated holes within the QDs to graphene electrons [5, 7]. Meaning, the graphene had excess of electrons upon illumination and received holes from the QDs. The n-type chemical doping may have been a result of the sodium hydroxide used to deter the rapid surface oxidation which was determined by a shift the dirac voltage as seen in Chapter 4. Alternatively, the n-type chemical doping may have been caused by the silicon elastomer used to seal the liquid-metal and graphene area in a flexible substrate.

5.4 **Adaptive control of graphene PN junction characteristics**

A fundamental transistor architecture used in modern phototransistors is the PN Junction photodiode. A photodiode operates similarly to a circuit diode, however, generates a photocurrent when light is absorbed in the depletion region between two materials with different carrier concentrations. A photodiode has two modes operation known as the photoconductive and photovoltaic mode. In a photoconductive mode, the PN junction is reverse biased and under illumination, a strong electric field is formed in the depletion region and aids the photocurrent [8, 9]. The main benefits of a photoconductive mode are a low junction capacitance and high linear response. The main disadvantages of a photoconductive mode are large dark current. In a photovoltaic mode, the PN junction is zero biased and the flow of current is restricted to the junction and a voltage builds in the presences of light as electron and holes are generated. The benefits of a photovoltaic mode are a low dark current and is typically used in solar cells. The disadvantages of a photovoltaic mode are the energy efficiencies are rather low and a large amount of light is required to generate significant voltage drops required by commercial solar cell application.

One can create a PN junction in monolayer graphene with two gates on or above graphene and a solid dielectric material [10, 11]. However, fabrication can be simplified by the suspension of collinear wires above graphene as part of a *LM-GFET* architecture with an electrolytic gate dielectric such as honey. A representation of this idea is shown in Fig. 5.5a. The device consists of a source and drain electrode comprised of liquid-metal, a graphene channel on PET, and two wires suspended above graphene and in honey with a 100 micron separation from the graphene

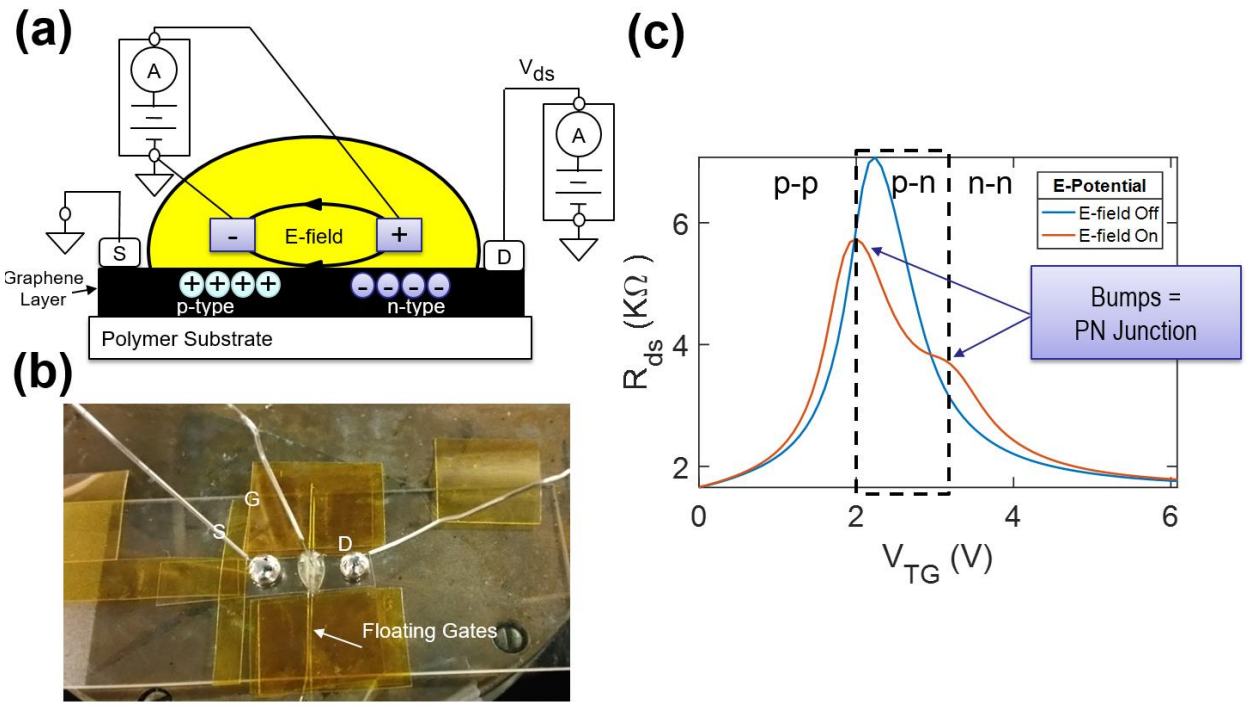

Fig. 5.5. (a) Illustration of PN junction embodiment with LM-GFET transistor architecture that utilizes honey as an electrolytic gate dielectric and (b) Image of the LM-GFET device with location of the floating gates used to generate PN junction characteristics. (c) Drain-to-source resistance R_{ds} as a function of top-gate voltage V_{TG}. The bump feature in R_{ds} illustrate the changes in carrier concentration throughout the graphene channel.

surface. For example, as the suspended electrodes are forward biased, holes are attracted to the negative terminal and electrons are attracted to the positive terminal. A measure of the drain-to-source resistance R_{ds} as a function of top-gate voltage V_{TG} reveal the PN junction phenomena, Fig. 5.5b. In the event, the lateral electric field is kept OFF, the relationship for R_{ds} demonstrates typical graphene transistor characteristics with a single charge neutrality point (dirac point). However, when the lateral electric field is turned ON, two dirac points appear and demonstrate PN junction characteristics in which an excess of hole carriers exist for $V_{TG} < 2.0\,V$, a PN junction froms between $2.0V < V_{TG} < 3.2\,V$, and an excess of electron carriers exists for $V_{TG} > 3.2\,V$. To further explore the PN junction phenomena a bi-directional sweep was performed with and Agilent 4155C Semiconductor Probe Analyzer in which the left and right floating gates were

varied from $-4\,V < V_{lg}, V_{rg} < 4.0V$ as the drain-to-source voltage was kept $V_{ds} = 1V$. The surface plots for the drain-to-source current I_{ds} and drain-to-source resistance R_{ds} are utilized to identify the pn, nn, np, and pp regions for a *LM-GFET* devices with an electrolytic gate dielectric made of honey, Fig. 5.6. A top view of the drain-to-source current I_{ds} clearly identifies the different biasing schemes and is illustrated in Fig. 5.7 alongside an illustration of the energy band diagrams that correspond to each region [12]. In the nn and pp regions, a strong lateral electric field favors homogeneous electrostatic doping as the electric double layer in the electrolytic gate dielectric is charged. However, the np and pn regions give rise to a asymmetric charge distribution that is evident by small bumps in the I_{ds} and R_{ds} profiles of Fig. 5.7a-b. Such techniques are applicable in photodetector applications as one could carefully control optical transitions by biasing in the correct scheme as illustrated in Fig. 5.7.

It is important to note, as the electric field strength is altered in Fig. 5.6, the distance between the two charge neutrality points changes. Moreover, the distance between the Dirac points than indicate the work function required to generate photocurrent which is governed by the fermi energy level $E_F = \hbar\, v_F \sqrt{\pi n}$, as described in Chapter 2. Whether optical interband transitions are allowed ($E_{ph} \geq 2E_F$) then becomes a design choice and is solely dependent on the designer's target frequency range.

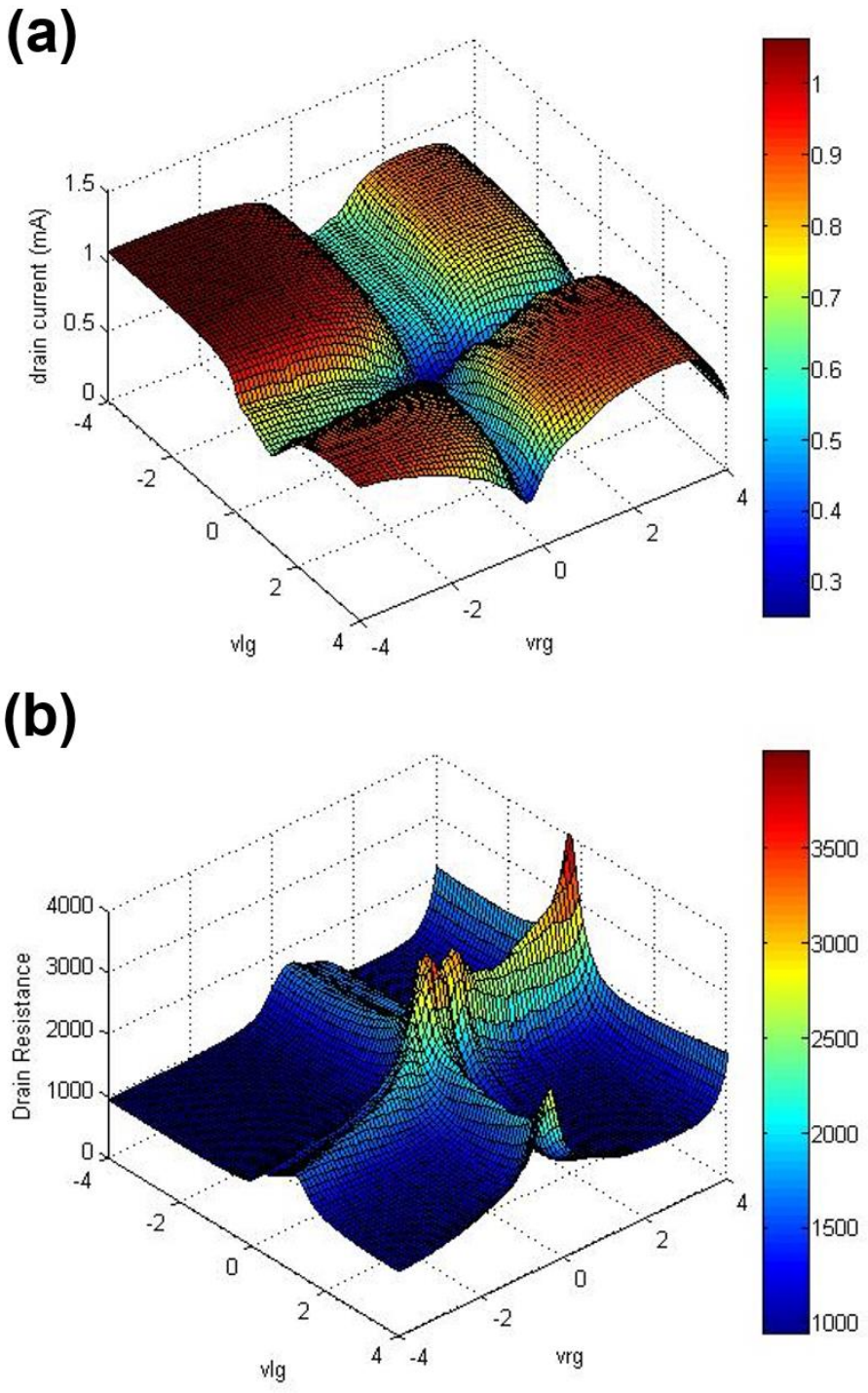

Fig. 5.6. Bi-directional sweep illustrating the (a) drain-to-source current I_{ds} and (b) drain-to-source resistance R_{ds} as a function of two floating top-gate voltages V_{lg}, V_{rg}. A colormap illustrates the I_{ds} and R_{ds} respectively. The drain-to-source voltage is 1V

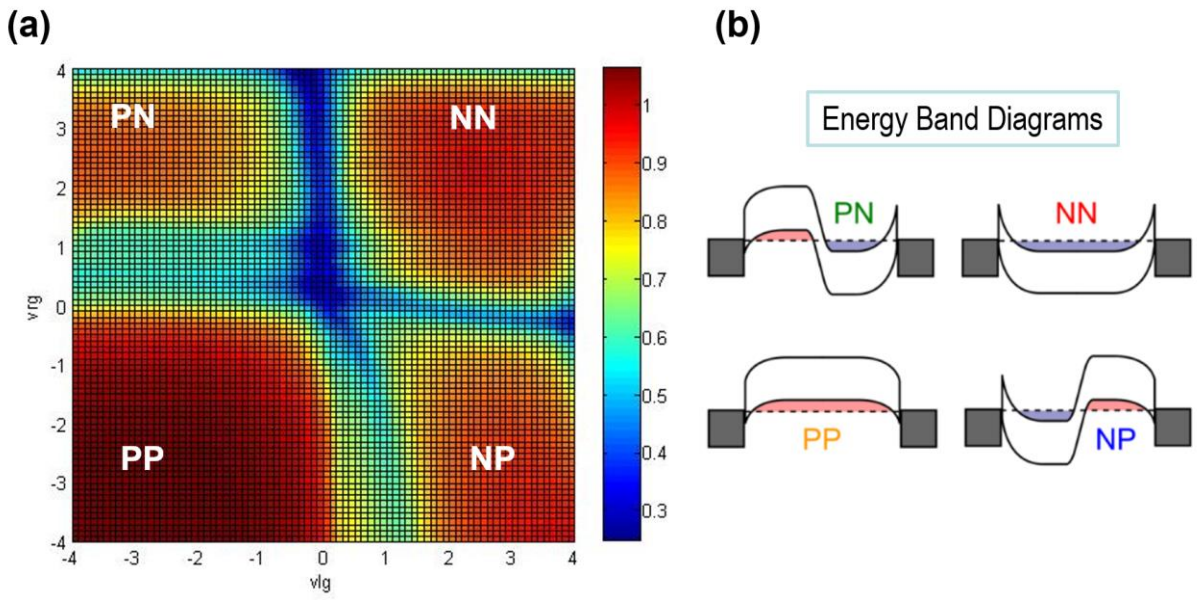

Fig. 5.7. (a) Top View of Bi-directional sweep for drain-to-source current I_{ds} as a function of two floating top-gate voltages V_{lg}, V_{rg}. (b) Representation of energy band diagrams for the pn, nn, pp, and np biasing schemes [12].

5.5 Hybrid LM-Graphene phototransistor with Quantum Dots and PN Junction

To explore the PN junction phenomena previously described in section 5.4 and to increase detector responsivity beyond that of the two-terminal graphene configuration (~28 uA/W) described in section 5.1, a hybrid graphene *LM-GFET* phototransistor with quantum dots and PN junction capability was fabricated. The hybrid *LM-GFET* transistor consisted of the *LM-GFET* architecture described in Chapter 4 with a electrolytic gate dielectric made of honey, combined with semiconductor quantum dots that act as optical absorbers as described in section 5.3, and the PN junction embodiment to control photocurrent as described in section 5.4. An image of the hybrid LM-Graphene phototransistor is shown in Fig. 5.8 along with a schematic theory of operation. The operation of the device was as follows:

- A biased PN junction controls graphene conductivity

- Under incident illumination, the quantum dots generate electron-hole carriers

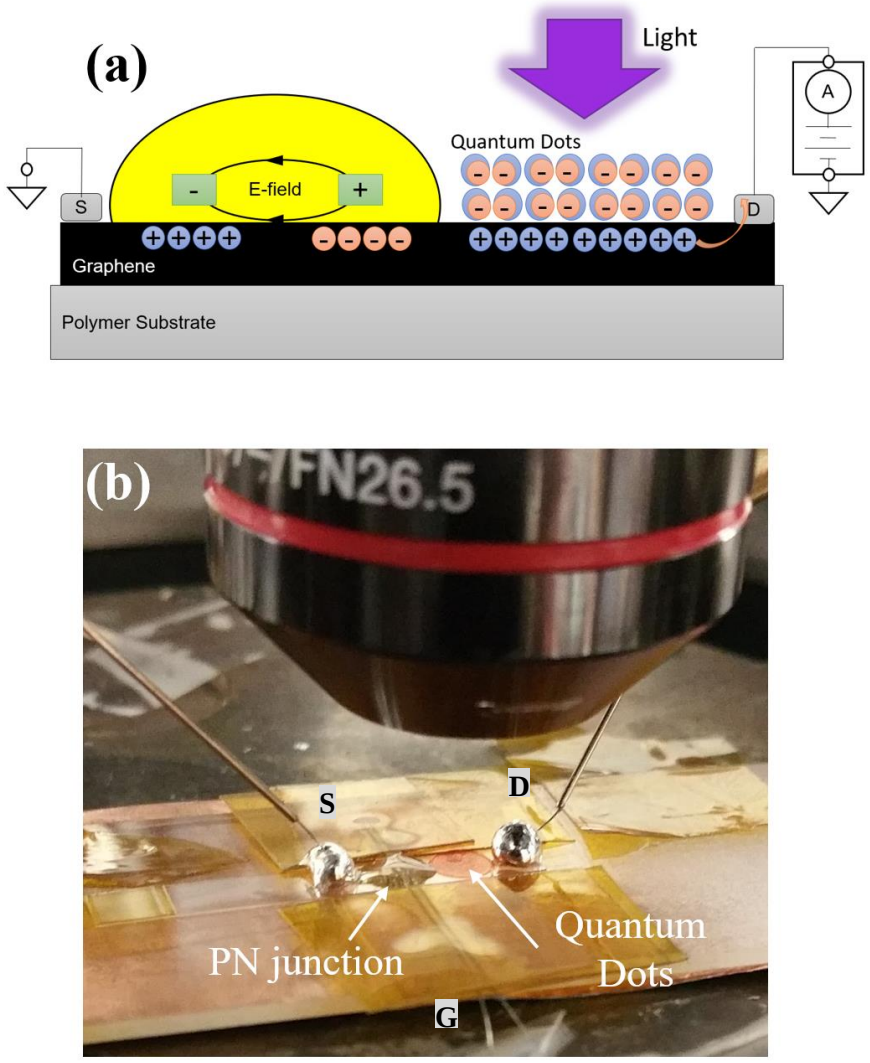

Fig. 5.8. (a) Schematic of hybrid LM-graphene phototransistor with quantum dots and PN junction capability and (b) image of the hybrid phototransistor architecture with the location of the quantum dots and PN junction area on the graphene surface.

- The holes transfer to the graphene surface and electrons remain trapped in the quantum dots lattice.
- Through capacitive coupling, a photogating effect occurs between the trapped quantum dot electrons and holes that previously transferred to the graphene material [5].

- The photogating effect alters the graphene conductivity that was originally set by the PN Junction
- In the event the PN junction was forward-biased, too much current is generated and filters out the quantum dot photoresponse
- In the event the PN junction is reverse biased, the photocurrent is directly proportional to the illumination

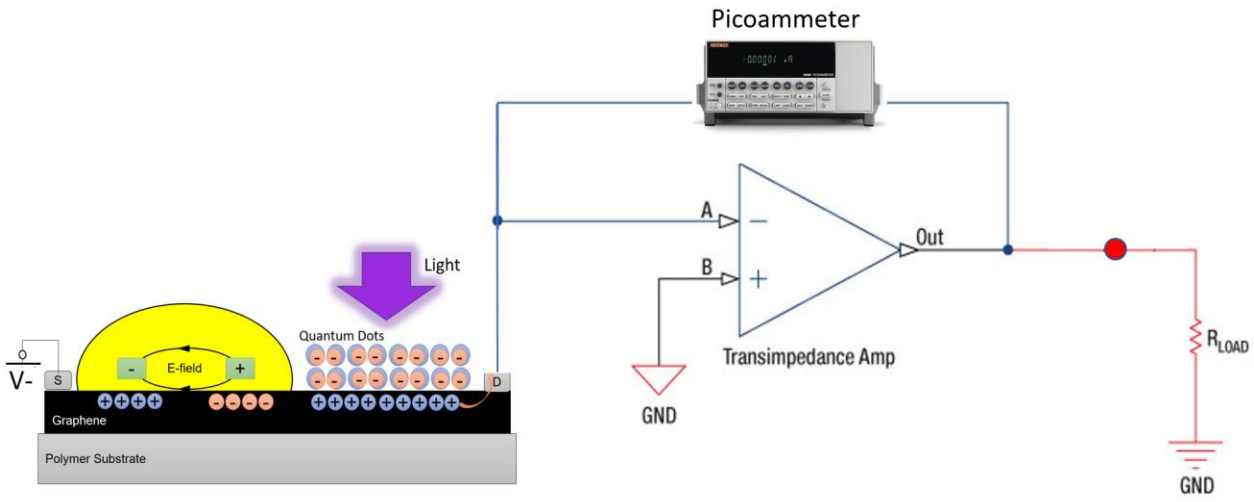

Fig. 5.9. Hybrid *LM-GFET* phototransistor circuit

To optimize photoresponse measurements a transimpedance amplifier was required to convert the photocurrent into an output voltage, Fig. 5.9. The photoresponse circuit consisted of a standard inverting operational amplifier configuration in which the non-inverting input is referenced to ground. Moreover, forces the phototransistor into a photoconductive mode when the phototransistor source is biased negatively. A load resistor can be connected from the output terminal of the operational amplifier and to ground to measure a voltage response. To measure photocurrent, one can replace the feedback resistor with a picoammeter that exhibits a negligible

internal resistance. Therefore, the measured photocurrent will have a 1:1 ratio with respect to phototransistor optical response.

To test the photoresponsivity, the hybrid *LM-GFET* phototransistor was illuminated with a collimated UV ($365nm$ Hamamatsu Lightning Cure Lc8) light source, power of $3mW$ and a diameter of 0.5cm. A Thorlabs Optical Chopper with a spin frequency of 1Hz was used to modulate the light source. The optical measurements were conducted in standard laboratory conditions with the room lights off.

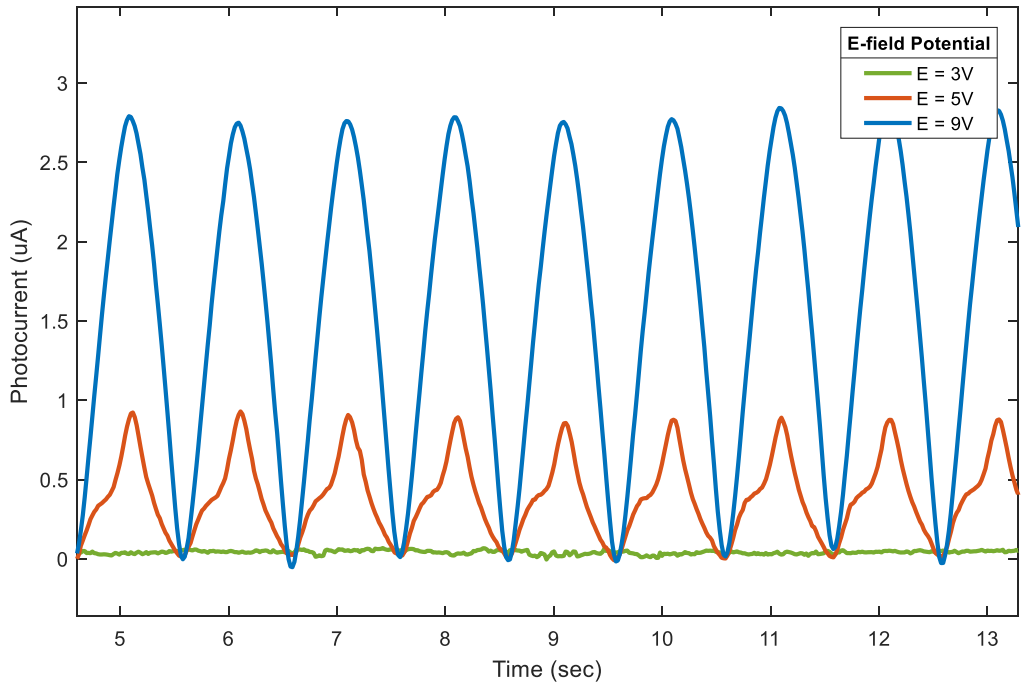

Fig. 5.10. Photocurrent response for a hybrid *LM-GFET* phototransistor with quantum dots and a PN junction as a function of time. The electric field potential was varied from $3V - 9V$ between the two top-gates suspended in the electrolytic gate dielectric comprised of honey.

It was determined from the optical measurements that the electric field potential used to bias the PN junction element would also control the amplitude of the generated photocurrent. A relationship between photocurrent and time, Fig. 5.10, demonstrated there was no observable photocurrent generation as the device was lightly reverse biased (V_{source} = -2V) with an electric field potential of $E = 3V$. As the electric field potential was increased there was appreciable photocurrent amplification. From $E = 5V$ to $E = 9V$, the photocurrent increased from 1uA to 3uA, corresponding to a photoresponsivity of $0.33mA/W$ and $1mA/W$.

It is noted that the graphene photoexcited carriers typically decay within picosecond times scales [2, 13, 14], therefore, do not contribute to the photocurrent. The increase in photocurrent of Fig. 5.10 as the PN junction induced electric field in graphene is increased can be contributed to an interaction with the quantum dot photoinduced field within the graphene channel under UV excitation. The quantum dot photoinduced field can couple with the field generated by the PN junction elements and allow the photoinduced charge carriers to escape the excitation region and induce current to the contacts [2, 14]. Under a strong electric field, the effect is maximized and results in larger photocurrent. The ability to turn on and off the photocurrent generation electronically enables a variety of controllable applications such as optical switches and optical resonators.

5.6 Discussion

In this Chapter, multiple optical sensor embodiments were demonstrated to explore the feasibility of the flexible transistor architecture as a photodetector element. With minimal fabrication steps a bolometric, integrated semiconductor quantum dots, PN junction, and a hybrid quantum dot and PN junction architectures was demonstrated. A gain of $35\ A/A$ was achieved with a hybrid architecture over a single graphene two terminal element. In addition, adaptive

control of the output photocurrent in the hybrid architecture with a simple change in electric field potential was achieved. A variety of applications can be explored with adaptive control such as optical switches, resonators, and free space optical communications.

It is important to note the $1mA/W$ measured photoresponsivity is still rather average with respect to the photodetector elements summarized in Table 5.1. Although, the fabrication steps of the summarized photodetector embodiments is rather complex and the dimensions of the devices is on the order of <100 microns. There is reason to believe the photoresponsivity of the *LM-GFET* architectures will improve as the dimensions are reduced. In that the two-terminal resistance will be reduced between source and drain and the PN junction induced electric field will couple better with respect to the photoinduced quantum dot electric field. Further work is needs to be done to determine the spectral photoresponsivity of the hybrid *LM-GFET* architecture to explore optical screening with photon energies less than two times the fermi energy level. Broadband frequency tunable operation can be achieved within a single photodetection element. In a spectrometer application size and weight can be reduced because the photodetection element will not need a diffraction grating. In addition, the use of liquid electrodes and dielectric materials enable a flexibility capability that has not been achieved by any of the summarized embodiments in Table 5.1. In either case, inexpensive materials liquid-metal and honey have been combined for the very first time in an optical phototransistor embodiment that demonstrated comparable results to the state-of-the-art.

REFERENCES

[1] A. Grigorenko and et al., "Graphene Plasmonics," *Nature photonics,* vol. 6, no. 11, pp. 749-758, 2012.

[2] F. Koppens and et al., "Photodetectors based on graphene, other two dimensional materials and hybrid systems," *Nature nanotechnology,* vol. 9, no. 10, pp. 780-793, 2014.

[3] M. Freitag and et al., "Photoconductivity of biased graphene," *Nature Photonics,* vol. 7, no. 1, pp. 53-59, 2013.

[4] Z. Li and et al., "High-sensitive hybrid photodetectors based on CdSe quantum dots and graphene for detecting ATP bioluminescence on lab-on-chip devices," in *Biomedical Circuits and Systems Conference (BioCAS), IEEE*, 2015.

[5] G. Konstantatos and et al., "Hybrid graphene-quantum dot phototransistors with ultrahigh gain," *Nature Nanotechnology,* vol. 7, no. 6, pp. 363-368, 2012.

[6] S. Reimann, "Electronic Structure of quantum dots," *Review of Modern Physics,* vol. 74, no. 4, p. 1283, 2002.

6. Summary & Dissertation Contributions

The adoption of graphene into modern electronics has had little success due to the challenges in fabrication. Researchers are often plagued by graphene degradation as a direct result of the complex microfabrication techniques used in fabrication. A researcher must be trained to utilize the microfabrication instruments and must prepare their devices in clean rooms. The complexity of such fabrication steps forces researchers to optimize their fabrication techniques continuously. These steps can become costly and time-consuming depending on the funds available and allotted time allowed to execute project task.

For the very first time, inexpensive materials liquid-metal and commercial electrolytic gate dielectrics have been utilized for flexible graphene field-effect transistor fabrication. With the fabrication steps disclosed in this dissertation, researchers can rapidly fabricate graphene transistors and aim their focus to exploration of the important graphene phenomena needed to advance graphene research without the need for complex fabrication techniques or equipment. Each device demonstrated in this dissertation took less than one hour to fabricate compared to much more sophisticated processing techniques that can take up to a few months depending on the skillset of the fabrication engineers. It is important to note the simplification of the graphene transistor fabrication described in this dissertation has allowed the author to explore graphene phenomena and analyze data daily more easily and efficiently. Furthermore, the *LM-GFET* devices fabricated have allowed undergraduate and graduate learners to work with graphene technology at the University of Hawai′i at Mānoa, Dept. of Electrical Engineering for the first time.

The *LM-GFET* devices provided a novel flexible transistor architecture that utilized inexpensive materials and can be applied to many sensor applications. The broadband optical absorption of graphene can enable a variety of nanophotonic applications as illustrated in Fig. 6.1. For example,

future efforts can explore contraband detection and surveillance for commercial applications. Moreover, an investigation can be led to explore night vision, aerial, and underwater communications for military applications in which size and shape are critical device parameters that must be optimized to increase mission range and duration.

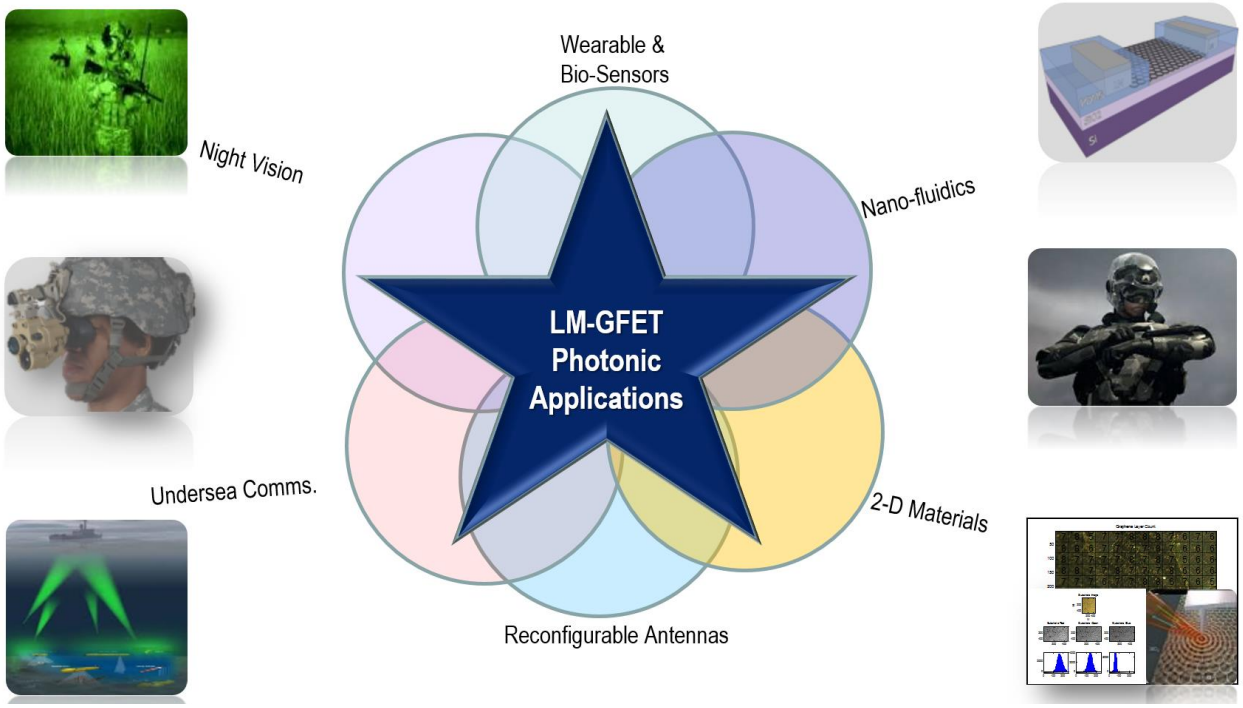

Fig. 5.1. Summary of Potential LM-GFET Photonic Applications

In either case, the conformability of the *LM-GFET* architectures provide numerous advantages for graphene devices beyond optical performance improvements. The *LM-GFET* enables a unique flexible capability for graphene electromagnetic sensors by the means of a microfluidic technology, a relatively widespread practice to manipulate liquids and droplets in the biomedical industry but uncommon method to fabricate transistors. Liquid-metal fluid flow can be controlled by series of carefully fabricated microfluidic cavities, Fig. 5.2. Fully flexible microfluidic structures have the potential to enable wearable electromagnetic sensors that can be integrated into clothing for

assisted optoelectronic applications or can be used as body temperature measurement devices that are disposable. As microfluidics reach nanometer resolution via advanced UV lithography techniques, it is viable to replace rigid semiconductor based transistors with microfluidics such as in the proposed *LM-GFET* devices. Microfluidic transistor level graphene electromagnetic sensors provide an interesting area for future study.

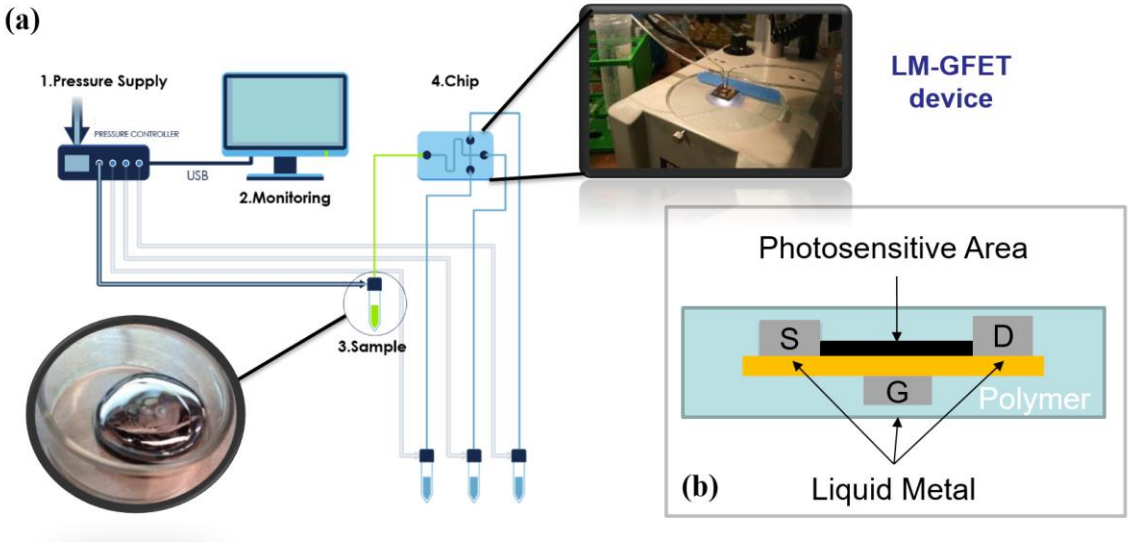

Fig. 5.2. Microfluidic Integration for LM-GFET (a) Utilization of micro-pipetting system to inject liquid-metal to LM-GFET microfluidic cavities.
(b) Illustration of potential device architecture.

In Summary, the *LM-GFET* architecture focused only on the integration of two-dimensional graphene. Since the author began this work, a variety of additional two-dimensional materials have been discovered. The use of conformal liquid-metal electrodes and electrolytic gate dielectrics as used in the *LM-GFET* devices provides possible expansion to alternate two-dimensional materials that include hexagonal boron nitride, molybdenum disulfide, and black phosphorus. With this in mind, additional nanophotonic applications can be investigated that may include display, solid state lighting, and ultraviolet imaging as described in Fig. 5.3.

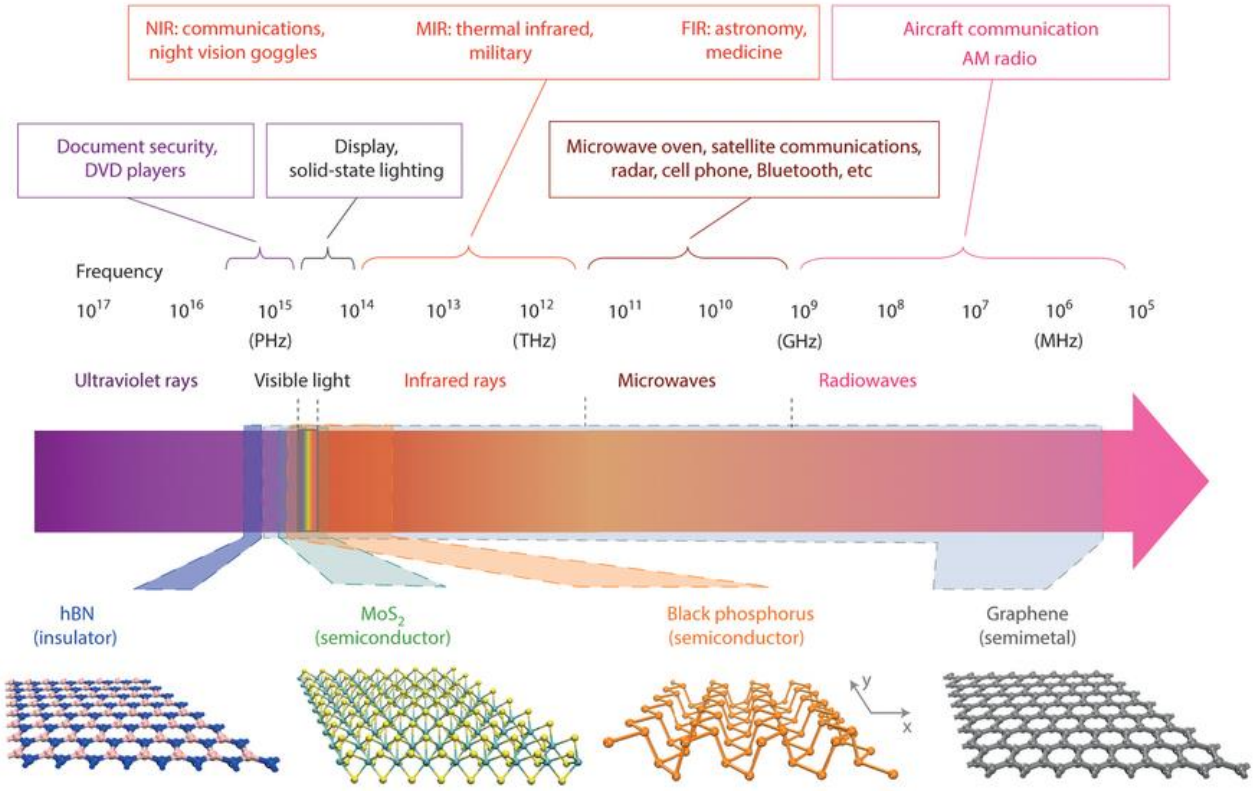

Fig. 5.3. Two dimensional materials covering a broad spectral range of applications [1]

REFERENCES

[1] F. Xia and et al., "Two-dimensional material nanophotonics," *Nature Photonics*, vol. 8, no. 12, pp. 899-907, 2014.

The End